Tuning Water Adhesion on Biomimicking Superhydrophobic MnO_2 Films

XIAODAN ZHAO

(B. Sc, Hua Zhong University of Science & Technology)

A THESIS SUBMITTED

FOR THE DEGREE OF DOCTOR OF PHILOSOPHY

DEPARTMENT OF PHYSICS

NATIONAL UNIVERSITY OF SINGAPORE

(2012)

Acknowledgements

I would like to express the deepest appreciation to my supervisor, Professor Liu Xiang-Yang, for his valuable guidance and advice, without his persistent help this dissertation would not have been possible. He has been continually and convincingly conveying a spirit of adventure in regards to research and scholarship, patiently mentoring the academic writing. Moreover, he has been enthusiastically encouraging us to learn from nature, and I have been really motivated by the project “biomimicing of lotus effect” and enjoying both the happiness and sadness of the research. I thank for his insightful suggestions and kind encouragement throughout my research.

I would like to thank to Prof. Fan Haiming for his advices and discussions in the study of the wettability on MnO_2 nanotube membrane. In addition, thank Professor Pan Haihua, who inspired me that physics is all around the world. I would also like to express my appreciation to Prof. Feng Yuanping, Prof. Yan Jie, Prof. Liu Ru Chuan, Prof. Luo Jun, Prof. Ding Jun, Prof. Zou Binsuo, Prof. Zhang Keqin for their guidance and help on my project research.

Meanwhile, I would like to thank my seniors and colleagues, Mr. Teo Hoon Hwee, Sin Yin, Du Ning, Tianhui, Liu Yu, Rongguo, Guobin, Shaokun, Wang Lei, Zhou Hu, Li Yang, Wang Hui, Linda, Zhiqiang, Wu Xiang, Yang Zhen,

Qinqiu, Yingying, William, Joel, Ye Dan, Tuan, Viet, Gong Li, Luo Yuan, Desuo, Naibo, Jiafeng, Boyou, Wengong, Liyong, as well as my friends Chen Yu, Yuli, Tang Pan, Tang Zhe, Xinjun , Song Qin, Lanfei, Guang Xin, Issac, Siew Kit, Zhicheng, Xinhe, for their help during my research life.

I am indebted to my parents for their deepest love and greatest faith in me. I regret that I didn't spend much time with them during these years, but they were always there to massage my stress whenever I was in blue. Since I can remember, they have been always encouraging me to pursue my dream, to be confident and to be independent.

I want to give a special thank you to my beloved wife Gangqin for her passionate and pristine love. She has pulled me out of the cave of my own lonely world to share happiness with friends.

Last but not least, I would like to express my acknowledgement to National University of Singapore for offering the scholarship to support my study.

Table of Content

Figures

Tables

Abbreviation

BCS	Ball cactus-like structure
CA	Contact angle
EW	Electro-wetting
FT-IR	Fourier transform infrared spectroscopy
HRTEM	High-resolution transmission electron microscopy
L-MLS	Large MLS
MLS	Meshlike structure
MTA	MnO_2 nanotube array
NPA	Nanopropeller array
NWS	Nanowire structure
PFOTES	1H,1H,2H,2H-perfluorooctyltriethoxysilane
SA	Sliding angles
SAED	Selected area electron diffraction
SEM	Scanning electron microscope
S-MLS	Small MLS
TA	Tilting angle
TCL	Three-interface contact line
TEM	Transmission electron microscopy
TNS	Tilted nanorod structure
XRD	X-ray diffraction
WCA	Water contact angle

Summary

Wettability of solid is important for both fundamental researches and technical applications, ranging from industrial coating to microfluidic engineering. Specifically, non-wettable surfaces with high contact angles and small sliding angles, called superhydrophobic or ultrahydrophobic, have received a large amount of attention in recent years. Water drops that come into contact with superhydrophobic surfaces remaining a nearly spherical shape, with contact angle close to 180° have been reported. These surfaces are of practical interest due to it water-repellent, antisticking, and self-cleaning properties.

Recently, special attention has been focused on the strong adhesive superhydrophobic or more properly superhydrophobic-like surfaces that enable a nearly spherical water droplet to be firmly pinned on the surfaces. Such novel superhydrophobic surfaces are expected to have particular applications in open microdroplet devices with respect to increasing the need for controlled transport of small volumes of liquids in localized chemical reactions, bio/chem analysis assay, single-molecule spectroscopy, and tissue engineering.

Currently, one of the challenges in this area is to design and fabricate smart surface systems that are able to adjust the wetting properties on demand. Therefore, the aim of my doctoral dissertation is to reveal a general route to prepare superhydrophobic surfaces with tunable adhesion and to explore new techniques to modulate adhesion on superhydrophobic surfaces in a fast and *in-situ* manner.

MnO_2 has increasingly attracted the attention because of its low cost, environmentally benign nature. In this doctoral dissertation, different nanostructures, ranging from nanorods, nanotubes, nano-sheets to hierarchical nanopropellers and ball cactus-like structured films have been obtained experimentally. According to the principles of roughness-enhanced superhydrophobicity and three-interface contact line (TCL) continuity related adhesive behavior, there is the possibility to tune the adhesion over a broad range in terms of various nanostructures and morphologies of MnO_2 nanocrystallites.

The stability is crucial for the functional superhydrophobic surfaces and lab-on-chip devices in real applications, and therefore it is necessary to design and fabricate robust superhydrophobic surfaces in the first step. Inspired by the structure of lotus leaves, the hierarchical MnO_2 nanopropeller array (NPA) was designed and fabricated by a two-step hydrothermal method. The robustness of superhydrophobicity was confirmed by the water droplet squeezing test. The

results showed that the NPA film maintained its superhydrophobicity under the pressure of 500 Pa, which was sufficient to address bouncing droplets and/or vibrating droplets in superhydrophobic state. Varied wetting properties were also investigated on MnO_2 nanostructured films with other morphologies and they are found to be good candidates for designing smart surfaces in a wide range of applications.

In order to uncover a general route to prepare superhydrophobic surfaces with controllable adhesion, we investigated the intrinsic correlation with structural features and the adhesive force. It was found that the tunable adhesion on a superhydrophobic MnO_2 nanostructured film can be achieved by fabricating different patterns including meshlike, ball cactus-like and tilted nanorod structures. The marvelous modulation range of the adhesive forces from 132.4 to nearly 0 μN endows these superhydrophobic surfaces with extraordinarily different dynamic properties of water droplet. This pattern-dependent adhesive property is attributed to the kinetic barrier difference, resulting in the different continuity of the three-interface contact line. This finding will help to provide the general strategies for the adhesion adjustment on superhydrophobic surfaces.

In-situ manipulating water adhesion on superhydrophobic surfaces was realized by application of a small Direct Current (DC) bias, maintaining large contact angles of water droplets. Upon this technique, the measured adhesive force of a 3

μL water droplet increased monotonically with increasing negative voltage, reaching a maximum of 130 μN at 22 V, 25 times higher than the original value. It follows that the nearly spherical water droplet can be controllably pinned on the substrate, even if the substrate is turned upside down. This remarkable electrically controlled adhesive property is ascribed to the change of contact geometries between the water droplet and MnO_2 nanotube arrays, on which water droplets exhibit different continuities of TCL. As the modulation in this manner is *in situ*, fast, efficient and environment-friendly, this kind of smart material with electrically adjustable adhesive property is expected to find various applications in biotechnology and in lab-on-chip devices.

Publications

1. Zhao X-D, Fan HM, Luo J, Ding J, Liu X-Y, Zou B-S, Feng Y-P (2011) *Electrically Adjustable, Super Adhesive Force of a Superhydrophobic Aligned MnO2 Nanotube Membrane*. **Adv Funct Mater**, 21 (1):184-190. doi:10.1002/adfm.201000603

2. Zhao XD, Fan HM, Liu XY, Pan H, Xu HY (2011) *Pattern-Dependent Tunable Adhesion of Superhydrophobic MnO2 Nanostructured Film*. **Langmuir**, doi:10.1021/la104709d

3. Zhao XD, Xu GQ, Liu XY, *Bioinspiration in Science and Technology, Part II: Water Channels, Structural Colors, Lotus Effect*, **Springer**, *prepared for submission*.

4. Zhao XD, Xu GQ, Fan HM, Liu XY, *Synthesis of hierarchical MnO2 nanostructure and their wetting properties*, *prepared for submission*.

Chapter 1

Introduction

Wettability of solid is important for both fundamental researches and technical applications, ranging from industrial coating to microfluidic engineering. Specifically, non-wettable surfaces with high contact angles and small sliding angles (SA), called superhydrophobic or ultrahydrophobic, have received a large amount of attention in recent years. Water drops that come into contact with superhydrophobic surfaces remaining a nearly spherical shape, with water contact angle (WCA) close to 180° have been reported.[1] These surfaces are of practical interest due to its water-repellent, antisticking, and self-cleaning properties. These properties are desirable for many applications, including raindrop self-cleaning,[2] oil spill cleanup,[3] water-capture devices,[4] laboratory-on-a-chip devices,[5] bioinspired geckos/mussels feet[6] and functional interface for cell and tissue engineering.[7]

1.1. Superhydrophobicity in Nature

In nature, various species exhibit impressive water-repellent property. One prominent example is the lotus leaf, which is well-known for its self-clean feature removing dust and mud by water droplets rolling off surfaces and is regarded as a traditional symbol of purity in Buddhist societies. In 1997, Barthlott *et al*.[8] revealed for the first time the interdependence between the surface roughness and the water-repellent property as well as dust particles adhesion. By comparing and summarizing the surface structures and their wetting properties of different plant leaves, the author found those with microsized papillae all exhibit WCAs larger than 150°. Figure 1.1(a) shows the Scanning Electron Microscope (SEM) image of lotus leaf (***Nelumbo nucifera***), from which fine-branched nanostructures on top of microsized papillae can be observed. Following researchers have found that such dual-scale structure combined with low surface energy is crucial to design superhydrophobic surfaces with large WCA and small SA.[9, 10] Barthlott *et al*. also coined the term "lotus effect" for the demonstrable superhydrophobic property and later researches on superhydrophobic surfaces have been activated to mimic the nature.

Since functionally optimized surface structures are one of the key innovations in the more than 400 million years of evolution of species, much more superhydrophobic surfaces with particular functions in wildlife have been explored. The water strider's legs are structured with numerous superhydrophobic

nanohairs, which provide impressive supporting force on water surface. The micrographs (Figure 1.1(b)) revealed numerous oriented setae on the legs. These needle-shaped setae endow a single leg with maximal supporting force about 15 times the total body weight of the insect. [11] The secret of the Stenocara beetle surviving in extremely arid habitat is due to its structured superhydrophobic back, which is able to collect water from the fog-laden wind in the morning.[4] The wings of many butterflies are endowed with superhydrophobic feature to prevent capillary forces sticking them together.[12] The fine structure of butterfly (*Papilio Ulysses*) wings is shown in Figure 1.1(c). Inspired by these observations in nature, increasing endeavors from chemistry, material science, physics and biology have been made to mimic those structures for varied functional concerns.

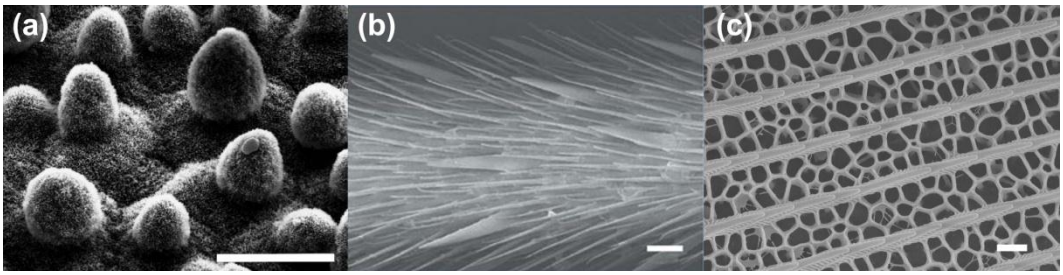

Figure 1.1 SEM image of (a) *Nelumbo nucifera* surface which is characterized by microsized papillae; *Reprinted with permission from ref. [8]. Copyright 1997, Springer.* (b) a water strider leg showing numerous oriented spindly microsetae; *Reprinted with permission from ref. [11]. Copyright 2004, Nature Publishing Group.* (c) hollow and bridges structures of *Papilio Ulysses* wings. Scale bars: (a) and (b) 20μm, (c) 1μm.

1.2. Bioinspiration and Biomimetics

In the biomimetics of functional superhydrophobic surfaces, it is found that suitable roughness combined with low surface energy are essential to obtain superhydrophobic surfaces, no matter what material is used (organic or inorganic) and what kind of structure formed on the surface (particles, rod arrays, or pores). As a result, roughening the surface followed by hydrophobization or transforming low-surface-energy materials into rough surfaces are common procedures to produce superhydrophobic surfaces. Since Kao *et al*.[13] have demonstrated the artificial superhydrophobic fractal surface made of alkylketene dimer and reemphasized the importance of geometrical structure in surface wettability, an increasing number of ways to fabricate superhydrophobic surfaces have been reported, either by introducing roughness into a low surface energy material and modifying a rough surface with low surface energy materials.

The mostly used substrates for fundamental research on superhydrophobic surfaces involve rigid solid substrates such as silicon wafers, glass slides and metal surfaces, which might limit the practical applications and the large-scale production of superhydrophobic surfaces.[14] Flexible substrates such as polymer films and fibrous substrates outperform the rigid substrates for superhydrophobic surfaces in industrial applications. The rough surfaces could be cast, spray coated

or post treated on polymer films with intrinsic low surface energy or imparted by hydrophobization. Fibrous substrates include woven or nonwoven textiles with natural or synthetic microfibers.

Practically, the methods for superhydrophobic surface preparation can be generally ascribed into three categories: top-down, bottom-up, and combination of bottom-up with top-down approaches. Top-down approaches involve lithographic and template-based techniques,[15] as well as surface plasma treatment.[16-23] Bottom-up approaches encompass mostly self-assembly and self-organization,[16-23] such as chemical deposition,[24-28] layer-by-layer (LBL) deposition,[28-32] hydrogen bonding,[24, 28, 29] and colloidal assemblies.[33] Methods combining bottom-up with top-down approaches contain casting of polymer solution, phase separation,[15, 27, 34-36] and electrospinning.[37] In the subsequent section, different approaches are illustrated in detail.

1.2.1. Top-down approaches

Top-down approach is a general term when referring to the manufacture of materials and devices by carving, molding, or machining bulk materials with tools and lasers in microelectronics, including technologies such as templation[30, 38, 39] and lithographic approaches,[40, 41] micromachining,[9, 42-46] and plasma treatments have been applied. The technologies are frequently combined in order

to produce surfaces with desired features. For example, the surfaces produced by lithographic approaches and micromachining can be used as a replicating template.

Template methods involve molding and replication steps with the template removed by lifting off,[47]dissolution[40, 41] or even sublimation as the following steps[48] in order to replicate the desired features. In the lithographic approaches, irradiation of light through a mask with designed features onto the substrates with a photoresist is followed by the etching steps, generating the desired patterned surfaces which correspond to the feature of mask. Silanization is subsequently used to make these surfaces hydrophobic.[49, 50] In micromachining, surfaces are diced into the anticipated texture.[9, 42-46] In the plasma treatments, surfaces are etched anisotropically hence yielding rough surfaces. For instance, plasma treatment of poly(ethylene terephthalate) (PET)[21, 22], poly(tetrafluoroethylene) (PTFE)[51], and polyethylene (PE).[19] Pulse-laser treatments of poly(dimethylsiloxane) (PDMS) for the fabrication of superhydrophobic surfaces have also been developed.[52, 53]

1.2.2. Bottom up approaches

Opposite from the top-down approach, bottom-up methods refer to the building of larger, more complex objects by integrating smaller building units or components. The bottom-up approaches in nano fabrication normally involve

self-assembly and self-organization. Self-assembly and self-organization are normally used interchangeably. To be specific, self-organization is a nonequilibrium process while self-assembly is an integration process leading to equilibrium in which components assemble spontaneously in solution or the gas phase until they reach a stable structure with minimum energy. Bottom-up approaches utilized in the preparation of superhydrophobic surfaces cover chemical deposition methods such as Chemical Bath Deposition (CBD),[23, 30-32] Chemical Vapor Deposition (CVD),[30, 31] and electrochemical deposition,[28, 29, 54] Layer-By-Layer (LBL) deposition *via* electrostatic assembly,[24] colloidal assembly,[27, 36] sol-gel methods,[34, 36, 55-63] hydrogen bonding,[33] and chemical synthesis.[64] Some important examples will be introduced and discussed in detail in the following paragraphs.

1.2.3. Combination of bottom-up and top-down approaches

The combination of bottom-up and top-down approaches is especially useful for creating substrates with a two-scale roughness, similar to the structure of the lotus leaf. The combination methods typically consist of two stages: the top-down approach creating a rough surface and the subsequent bottom-up process producing fine roughness. However, combination methods do not necessarily require a distinct two-stage process. Take phase separation for example, it

involves casting of thin film and succeeding phase separation by adjusting the environmental conditions.

Sun *et al.*[65] have utilized chemical vapor deposition (CVD) to fabricate superhydrophobic film with anisotropicly aligned carbon nanotubes (ACNT) with uniform tube length on quadrate micropillar arrays silicon substrates produced by photolithography. Due to the anisotropic nature of the carbon nanotube arrays, both hydrophobic and hydrophilic surfaces coexist depending on the spacing between the pillar arrays. However, after further coating with a fluorinated SAM of (2-(perfluorooctyl)ethyl)trimethoxysilane, all surfaces turned to be superhydrophobic without the spacing effects.

Most porous polymer membranes are produced by casting polymer solution through an appropriate template, with microscopic structures formed by phase separation, which occurs when the polymer solution approaching the cloud point is immersed in nonsolvents or experiences heat treatments. The nucleation of polymer results in rich poor phases of polymer due to the interaction of solvent and nonsolvents with macromolecules. The macromolecules nucleate and the networks form in the polymer rich phase whereas pores form after the solvent removal in the polymer poor phase.[66]

Micelles are termed as the aggregates of colloidal dimensions formed by the association colloids which are in equilibrium with molecules or ions. Micelles are formed by the microscale phase separation. Block copolymers form micelles due to the different solubility of the blocks in the particular solvent.[67, 68] The cast micelles formed by block polymer will generate films with different morphologies when exposed to environments with varied relative humidity.

Electrospinning is normally a process for extruding polymer nanofibers from the extrusion nozzle to a grounded collection plate where an electrical bias is applied.[69] A continuous, nonwoven web of electrospun fibers forms films, along the trajectory of the extruded polymer fiber, where most of the solvents evaporate. The film properties can also be modified by introducing chemical modification such as fluorine.[39]

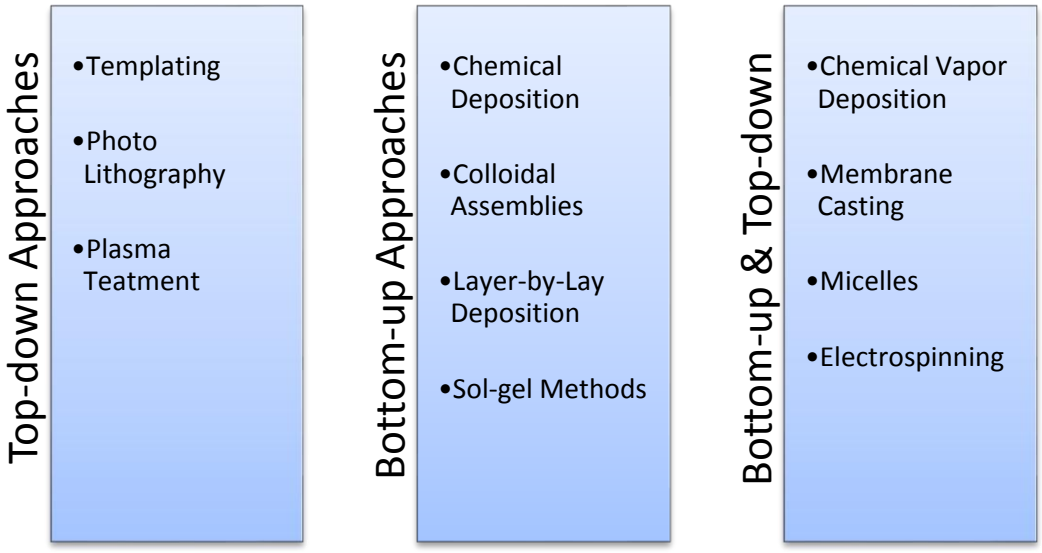

1.3. Theoretical Modeling of Superhydrophobicity

To understand the relationship between surface roughness and its wetting property of structured superhydrophobic surfaces in nature and other mimicking materials, Wenzel's[70] and Cassie's[71] theories are the most applied. Essentially, these two theories describe different superhydrophobic states: the former is complete wetting and the latter is when water droplets sit on composite surfaces with air pockets trapped underneath. Besides, some other researchers[72-75] have argued that it is the TCL rather than the interfacial area within the perimeter that determines the contact angle behaviors including advancing, receding, and contact angle hysteresis (the difference between advancing and receding angle). Even though conceptual problems may exist within Wenzel's and Cassie's theories, they still have merits to be applied at certain situations as advocated by their critics.[73-75] It is fairly straightforward to use them to characterize two distinguishable superhydrophobic states: the "slippy" Cassie state and the "sticky" Wenzel state. In general, water droplets adhere more strongly to the textured surface in the Wenzel state than in the Cassie state, causing stronger contact angle hysteresis. In many cases, water droplets on structured surfaces are in the metastable Cassie state and the transition from Cassie to Wenzel state can be induced by external stimuli, such as pressure, electric voltage, or vibration, *etc*.

1.3.1. Ideal Surface

The wetting angle of a water droplet on an ideal surface is determined by the Young law[76] with the assumption of the balance among the cohesive forces acting in the three-interface contact line (TCL) shown in Figure 1.2(a) (see Eq. $F_{SV} = F_{LV}\cos\theta_Y + F_{SL}$ (1.1)).

$$F_{SV} = F_{LV}\cos\theta_Y + F_{SL} \tag{1.1}$$

Where $F_{ij,}$ refers to the cohesive forces assumed acting in TCL, θ_Y represents static equilibrium contact angle. For many years, this equation has been reinterpreted in a way of thermodynamic equilibrium by substituting forces by surface tension.

$$\cos\theta_Y = \frac{\gamma_{SV} - \gamma_{SL}}{\gamma_{LV}} \tag{1.2}$$

where γ_{SL}, γ_{SV}, and γ_{LV} refer to the interfacial energy in the solid−liquid, solid-vapor, and liquid-vapor interface, respectively. Young's theory provides a very simple description of the different wetting scenarios on flat surfaces with varied surface energy. When the solid-vapor interface exhibits a high surface energy, theoretically the addition of γ_{SV} and γ_{SL} equals γ_{LV}, and then the drop wets completely the surface, reaching a superhydrophilic state, with WCA less than 5°. In the case of surfaces with low surface tension, the WCA increases. WCAs on surfaces higher than 90° are commonly defined as hydrophobic state, while WCAs higher than 150° are referred as superhydrophobic state.

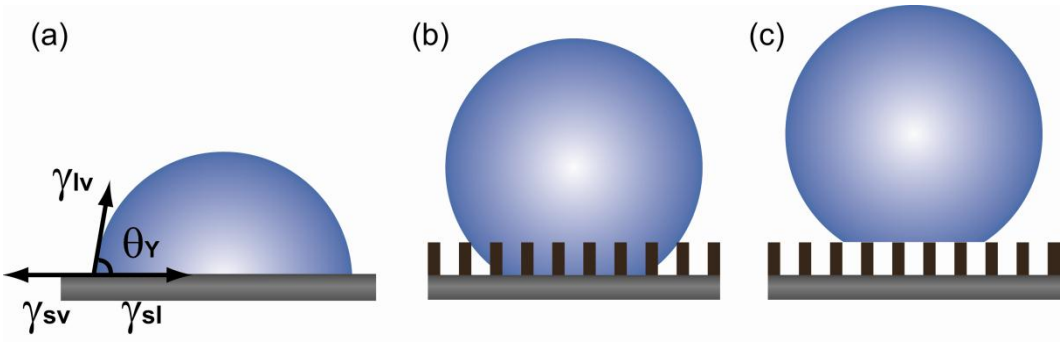

Figure 1.2 Schematic illustration of wetting state: (a) Drop on an ideal surface with CA θ and γ_{ij} indicated. (b) Wenzel state. (c) Cassie-Baxter state.

1.3.2. Non-ideal Surfaces

It was found at an early stage that surface roughness and morphological heterogeneities may lead to a deviation of CA from the value predicted by Young's equation.[70, 71] To correlate the CAs of real surfaces, two models i.e. Wenzel Model and Cassie-Baxter Model are commonly applied.

Wenzel Model Wenzel[70] introduced nondimentional surface roughness *r* to address the roughness amplified wetting properties of the smooth surface. *r* is the ratio of the actual area of liquid-solid contact to the projected area on the horizontal plane (Figure 1.2(b)). In this case, the actual area of the drop's solid-liquid interface is enlarged by a factor *r*. It follows that the CA on the rough surface, θ_W, is expressed as:

$$\cos\theta_W = r\cos\theta_Y \quad (1.3)$$

Eq. $\cos\theta_W = r\cos\theta_Y$ (1.3) implies that a flat hydrophobic surface with θ_Y>90° becomes more hydrophobic via increasing the surface roughness. Similarly, a flat hydrophilic surface with θ_Y<90° becomes more hydrophilic if the roughness is introduced. Meanwhile, if the *r* reaches a critical value as $1/\cos\theta_Y$, the CA turns to 0°, known as complete wetting or superwetting.

Cassie/Baxter Model Cassie and Baxter considered the effect of chemical heterogeneities of the surface on the measured apparent contact angle.[71] In their model, the total surface energy is considered as the average of respective component surface energy in the equilibrium state (Figure 1.2(c)). It follows that the contact angle θ_C on the heterogeneous surface, is expressed as:

$$\cos\theta_C = \sum_i \phi_i \cos\theta_i \quad (1.4)$$

where Φ_i is the area fraction of component surface and θ_i is the angle corresponding to area fraction *i* ($\sum \phi_i = 1$).

On rough materials characterized by very hydrophobic surface chemistries and/or pronounced degrees of roughness, drops often prefer to rest on top of the roughness features, with air trapped underneath (Figure 1.2(c)).[8, 77, 78] In this case, the heterogeneous surface can be simplified as a composited surface composed of solid and air, where the air parts of the interface are considered as

perfect non-wetting. It follows that the measured contact angle becomes: $\cos\theta = \phi(\cos\theta_{\mathrm{Y}} + 1) - 1$, where ϕ is the fraction of solid in contact with the liquid.

Eq. $\cos\theta_{\mathrm{W}} = r\cos\theta_{\mathrm{Y}}$ (1.3) and $\cos\theta_C = \sum_i \phi_i \cos\theta_i$ (1.4) have sometimes been combined to a more general form:[79]

$$\cos\theta_{\mathrm{C}} = \mathrm{r}\phi\cos\theta_{\mathrm{Y}} + \phi - 1 \tag{1.5}$$

where θ_{C} is the apparent contact angle on the rough surface and *r* refers to the degree of roughness of the solid area that contacts with liquid.

1.4. Dynamic Wetting Behavior

Both Wenzel's and Cassie-Baxter's theories predict the apparent CA in the equilibrium state, describing the static behavior of a liquid drop. In order to characterize the dynamic wetting behavior, advancing/receding angles and SA are measured to evaluate the repellency of a surface. By definition, the maximum/minimum values of CAs for a drop front which has been advanced/receded over a surface are termed the advancing/receding angles; the difference between advancing angle and receding angle renders the CA hysteresis. SA can be measured as an inclined plate tilts at a critical angle, beyond which a liquid drop will rolling off or sliding down the plate surface. The quantitative

relationship between the contact angle hysteresis and SA is provided by Eq. $\mathrm{mg}(\sin\alpha)/\mathrm{w} = \gamma_{\mathrm{LV}}(\cos\theta_{\mathrm{R}} - \cos\theta_{\mathrm{A}})$ (1.6)[80]

$$\mathrm{mg}(\sin\alpha)/\mathrm{w} = \gamma_{\mathrm{LV}}(\cos\theta_{\mathrm{R}} - \cos\theta_{\mathrm{A}}) \quad (1.6)$$

where θ_{A} and θ_{R} are the advancing and receding angles, respectively, *g* is the gravity force, *m* and *w* represent the mass and width of the drop, correspondingly. Eq. $\mathrm{mg}(\sin\alpha)/\mathrm{w} = \gamma_{\mathrm{LV}}(\cos\theta_{\mathrm{R}} - \cos\theta_{\mathrm{A}})$ (1.6) shows that small CA hysteresis results in small SA, indicating liquid drop rolling off or sliding down surfaces effortlessly. This equation also interprets one of the mechanisms of Stenocara beetle's back. Condensed water droplets roll off easily to be collected due to small SA on superhydrophobic surfaces.

1.5. Three-interface Contact Line Related Wetting Behavior

As discussed above, even though Wenzel's and Cassie's theories achieve great agreement with experimental results in many areas, unfortunately they make no statement about hysteresis. In the case of Cassie's theory, it simply describes an increasing ''most stable'' (in Marmur's notation)[81] CA in an equilibrium state with decreasing solid fraction ϕ. However, many experimental results show that drops may behave quite differently on two patterned surfaces of identical ϕ,[82]

thus, the solid fraction should not be the only parameter determining the contact angle hysteresis. Chen *et al*. suggested that the topology of rough surfaces played an important role in determining the contact angle hysteresis.[83] And they concluded that the contact angle hysteresis correlated to the continuity of TCL formed differently on varied patterns. When drops are in contact with a mesh-like porous structure, the TCL is in continuous contact with the roughness features and large contact angle hysteresis is found. Comparatively, for a surface consisting of isolated roughness features, like posts shown in the literature, they assumed that the energy barriers decreased between metastable states, giving rise to a lowered contact angle hysteresis. Öner and McCarthy followed the same principle, highlighting the significance of ‘‘destabilizing the contact line’’ in a way to obtain superhydrophobic materials.[42]

1.6. Wetting transitions

On some rough surfaces, drops can coexist in both Wenzel and Cassie states, depending on the way how the respective drop was deposited.[41, 84-88] From theoretical prediction, the Wenzel state is energetically favored for a given r and ϕ, if the CA on a smooth material θ_Y, is below a critical value θ_{Crit}. θ_{Crit} can be obtained by equating the Wenzel and the Cassie equation [Eq. $\cos\theta_W = r\cos\theta_Y$ (1.3) and $\cos\theta_C = r\phi\cos\theta_Y + \phi - 1$ (1.5)]:[89, 90]

$$r\cos\theta_{\text{Crit}} = \phi\cos\theta_{\text{Crit}} + \phi - 1 \tag{1.7}$$

In reality, kinetic barriers may stabilize drops in a metastable state instead of the minimum-energy state.[44, 88, 91-93] Consequently, drops in both Cassie and Wenzel wetting states may appear on the same material. Theoretically, Patankar derived a model on a post array to study the Cassie to Wenzel transition.[44] For a hydrophobic surface (i.e., θ_Y>90°), the initial impalement of a drop on the post array was found to be correlated with an increase in interfacial energy. Energy was then recovered when the drop was in contact with the bottom of the post surface and liquid-air interface was replaced by liquid-solid interface. Following similar line of thought, Nosonovsky and Bhushan provided an energy diagram of the Cassie-to-Wenzel transition, illustrating both states separated by an energy barrier.[93]

Varied external stimuli have been applied to introduce a transition of drops from the Cassie to the Wenzel state including pressure,[41, 85, 86, 90] vibrating,[94] electrical voltage,[95, 96] and evaporation.[93, 97] In principle, the driving force for the transition can be ascribed to the increased Laplace pressure ΔP across the drops' liquid-air interfaces.[98] The pressure difference ΔP can be calculated by Laplace equation which correlates surface tension, γ_{lg}, and the radius of the meniscus R:

$$\Delta P = \frac{2\gamma_{lg}}{R} \tag{1.8}$$

Theoretically, Bartolo *et al*. modeled the critical Cassie and Wenzel transition in "touching" and "sliding" scenarios based on the vertical aligned pillars. A Cassie-to-Wenzel transition takes place once the meniscus is so intensively curved that either direct contact with the bottom of the surface or the local advancing angle, which is defined as the advancing angle of the sidewalls of the rough structure is reached, so that the meniscus can slide down to bottom. In drop impact experiments, the energy necessary for inducing a Cassie-to-Wenzel transition as a function of the post height was measured on a structured post array.[99] For a transition to occur, Bartolo *et al*. found an approximately linear increase in the energy barrier with increasing post height and reached maximum upon a critical post height. This trend suggests that the "touching" mechanism determines the Cassie-to-Wenzel transition before critical post height, while "sliding" scenario occurs after that point. This model has been further proved in his following research by investigating the shape of the drop footprint during the Cassie-to-Wenzel transition.[97] For a similar post-type structure, Zheng *et al.* simulated the hydraulic pressure at which a transition begins, ΔP_{Crit}, as:[100]

$$\Delta P_{Crit} = \frac{\gamma_{lg}\phi\cos\theta_Y}{(1-\theta)\lambda} \tag{1.9}$$

where λ is the cross-sectional area of a post divided by its perimeter. In contrast, Extrand *et al.*'s results suggested that ΔP_{Crit} increased with an increase in the

λ_P-parameter.[101] Furthermore, Liu and Lange simulated the critical pressure on a surface composed of regularly arranged, microscale spheres[102]. Bormashenko *et al.* revealed that a critical threshold parameter responsible for the Cassie-to-Wenzel transition depended on the force per unit length of the triple line instead of pressure.[94]

Moreover, some recent experimental studies and simulations suggest that the transition from the Cassie to the Wenzel state starts from one or more nucleation sites instead of over the entire drop footprint at once.[103-106] How the transition proceeds is then determined by how easily the meniscus can move within the surface structure.

Compared to the Cassie-to-Wenzel transition, the Wenzel-to-Cassie transition has received much less attention, and it is mainly due to the rare observations. The Cassie-to-Wenzel transition is generally considered as an irreversible process for the case where the Wenzel state is at the absolute energy minimum.[91, 92, 107] However, recent studies on condensation of water on microstructure indicate that Wenzel-to-Cassie transitions are possible when the Wenzel state is metastable, and the Cassie state stay within lower energy state.[88] The solid experimental results showed that Wenzel, Cassie and mixed Wenzel-Cassie drops co-existed when water was condensed onto microscale post-type surfaces.[87, 88] In one series of experiments it was found that, Wenzel drops could sometimes make a

transition to the Cassie state either entirely or over part of their footprint area through coalescence during the condensation process.[88] The authors suggest that the calescence of two drops eliminates liquid-air interfacial area, and then enough energy is brought into the system for this energy barrier to be overcome.

Chapter 2

Materials Synthesis and Experimental Techniques

MnO_2 has increasingly attracted research attention because of its low cost, environmentally benign nature. Different nanostructures, ranging from nanowires, nanotubes, nano-sheets to hierarchical spheres and hollow urchins have been obtained experimentally.[108-111] According to the principles of roughness-enhanced superhydrophobicity and Three-phase-Contact-Line (TCL) continuity-related adhesive behavior, there is the possibility to tune the adhesion over a broad range in terms of various nanostructures and morphologies of MnO_2 nanocrystallites. In this chapter, the typical sample preparation of MnO_2 film by chemical bath deposition as well as growth mechanism will be discussed. In order to achieve superhydrophobicity, MnO_2 films were modified by surfactants and

Fourier transform infrared spectroscopy (FT-IR) was applied to verify the existence of surfactants assembly. Some other experimental techniques involving contact angle measurement and normal adhesive force measurement by self-designed setup will be covered.

2.1. Materials Synthesis

Chemical deposition is generally used for generating thin films of crystalline inorganic materials, such as ZnS, CuSe, InS, CdS, MnO_2 *etc*, with the materials self-assemble and deposit on some appropriate substrates. The chemical deposition encompasses different methods such as chemical bath deposition (CBD), chemical vapor deposition (CVD), and electrochemical deposition, in regard to corresponding deposition conditions. Various surface morphologies can be obtained ranging from nanopins, nanotubes to nanorods, by changing the material and tuning the deposition conditions.

CBD is implemented to create a nanopin film from a solution of $CoCl_2$ and NH_2CO in water by Hosono *et al.*.[32] The nanopin film with the top of the needle very sharp (a diameter of 6.5 nm) was deposited on borosilicate glass slides in an autoclave. Besides, the nanopin exhibits single crystalline-like structures because each metal complex in the solution is singly deposited on the surface owing to thermodymanic equilibrium conditions. Subsequently, the nanopin was treated

with lauric acid (with θ = 75.1) to acquire a superhydrophobic surface, of which the measured water CA of is 178°.

Wu *et al.*[112] also used CBD to prepare uniform and dense superhydrophobic surfaces of zinc oxide (ZnO) nanorods with diameters ranging from 400 to 600 nm on glass slides as substrate, using a solution mixture of $Zn(NO_3)_2$, NH_4Cl, urea, and ammonia. Surface modification with SAMs of alkanoic acids of different chain length generate substrates with high advancing contact angle (>150°), and different receding angles determined by the chain length of the alkanoic acids.

2.1.1. Synthesis of MnO_2 Nanotube array (MTA)

Synthesis of MTA membranes is the cornerstone for studying on functional superhydrophobic MnO_2 surface. Through investigating the mechanism and optimizing the growth process, many MnO_2 films with other various morphologies can be obtained. The typical MTA membranes were prepared by a simple hydrothermal approach. All the reagents were of analytical purity without further purification. In a typical experimental procedure, 2.5 mmol $KMnO_4$ and 10 mmol concentrated HCl were added to 45 mL deionized water to form the precursor solution, and then the solution was transferred into a Teflon-lined stainless steel autoclave with a capacity of 100 mL. In order to grow the single-layer aligned MnO_2 nanotube array, a piece of Si wafer (1 x 3 cm^2) coated

with 10 nm Pt seeds was placed in the autoclave. The autoclave was sealed and hydrothermally treated at 140° C for 12 hours. After the autoclave was cooled down to room temperature naturally, the samples were collected and washed several times by ethanol. The as-prepared sample was then dried in air overnight for further modification.

In order to elucidate the formation mechanism of the MTA, time evolution of the morphology has been investigated. The two typical growth stages selected from the different reaction time reveal clearly that the nanotube is formed by chemically etching the solid nanorod. As shown in Figure 2.1(a), the sample with a reaction time of 135 min grows into α-MnO_2 tetragonal nanorods, and no tube-like structure is found during this growth time. After 210 min of hydrothermal treatment, as shown in Figure 2.1(c), the top ends of nanorods are partly dissolved and the smooth ends of the nanorods change into coarse and irregular surface. This etching process starting from ends of nanorods is schematically illustrated in Figure 2.1(d). Prolonging the reaction time, these partly corroded nanorods eventually transform into the hollow nanotubes. The tetragonal open ends of nanotubes are clearly shown in Figure 2.1(e) and the thickness of tube walls is about 23 nm in average. The overall formation process of α-MnO_2 nanotubes traced with different reaction time is schematically shown in Figure 2.1(b), (d) and (f). The MnO_2 nanorods are first formed undergoing anisotropic growth driven by chemical potential in the hydrothermal process.

However, it might not be energetically stable to form solid MnO_2 nanorods due to the surface energy coming from large top areas of polar metastable (001) surface. Instead, the formation of hollow MnO_2 nanotubes will reduce the top metastable areas and increase the lateral areas of the most stable low-index nonpolar surfaces with respect to those of the corresponding solid nanorods. Similar processes have been observed in the formation of ZnO[113] and Fe_2O_3[114] nanotubes in CBD process. It is noted that the MnO_2 nanorods undergo a very fast etching process once the small pits on (001) surface of the MnO_2 nanorod end are shaped. However, increasing the reaction time is necessary to form smooth interior surface.

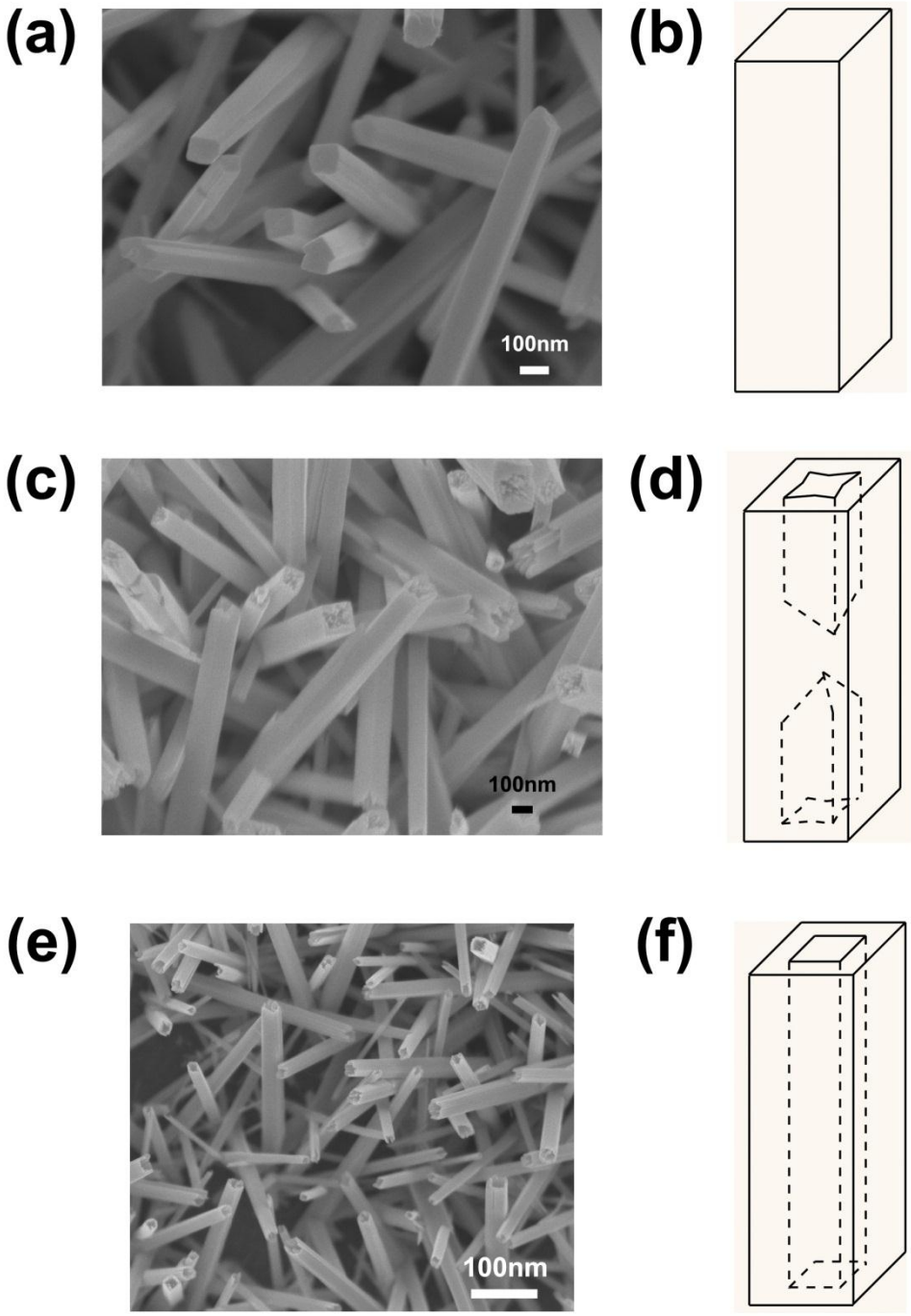

Figure 2.1 (a) SEM image of α-MnO_2 tetragonal nanorods with a reaction time of 135 min. (c) SEM image of α-MnO_2 tetragonal nanorods with partially open end after 210 min reaction time. (e) SEM image of α-MnO_2 tetragonal nanorods with full open end after 12 h reaction time. (b), (d) and (f) are schematic illustration of (a), (c) and (e), respectively.

2.1.2. Surface modification

Surface modification is the act of modifying the surface of a material by altering physical, chemical and/or biological characteristics different from those originally possessing on the surface of a material. Surface modification can be accomplished using plasma, corona, photolysis and chemicals. Comparatively, chemical processes are simple and there is no particular requirement for capital equipment. Therefore, the modification can be done in most work environments with proper storage and handling. The chemical preparation of materials and the cost per application is fairly low.

In our experiment, since the as-prepared α-MnO_2 nanotube array and other MnO_2 films with different morphologies were nearly superhydrophilic, surface modification becomes a crucial process for MnO_2 films to achieve superhydrophobicity with a CA of larger than 150°. Different types of surfactants including stearic acid sodium salt ($CH_3(CH_2)_{16}COONa$), oleic acid sodium salt ($CH_3(CH_2)_7CH=CH(CH_2)_7COONa$), sodium dodecanoate ($CH_3(CH_2)_{10}COONa$), and PFOTES (1H,1H,2H,2H-perfluorooctyltriethoxysilane ($CF_3(CF_2)_5CH_2CH_2Si(OCH_2CH_3)_3$) have been tested in surface modification.

To be specific, the as-prepared MTA membranes were treated in a 0.1 mol/L stearic acid sodium mixture solution of water /ethanol (4:1) for 1 hour at 60°C. After that the samples were collected and washed several times by ethanol. The

molecules of stearic acid can be firmly anchored on the surface of the MnO_2 nanotubes by forming a metal complex.[115]

2.2. Experimental techniques

2.2.1. Fourier Transform Infrared Spectroscopy (FT-IR)

The wettability of MnO_2 film surfaces changes from nearly superhydrophilic to superhydrophobic state after surface coating with surfactants. The change of wetting behavior of surfaces indicates the presence of the surfactant molecules assembling on the surface. To further verify the existence of surfactants on MnO_2 films, infrared spectra of the stearic acid sodium used to treat MnO_2 nanotube membrane were recorded on NICOLET 380 FT-IR spectrometer.

FT-IR is a technique which is applied to obtain an infrared spectrum of absorption, emission, or photoconductivity of a solid, liquid or vapor. Comparing to an obsolete dispersive spectrometer, an FT-IR spectrometer is able to collect spectral data in a wide range. The core structure of FT-IR spectrometer is the interferometer, and the most applied configuration is Michelson interferometer shown in Figure 2.2. A Michelson interferometer consists of two highly polished mirrors, a fixed mirror and a moving mirror. A source emits monochromatic light that hits a half-silvered mirror and then splits two lights to the two mirrors. Both two lights reflected from mirrors are recombined and collected from the detector.

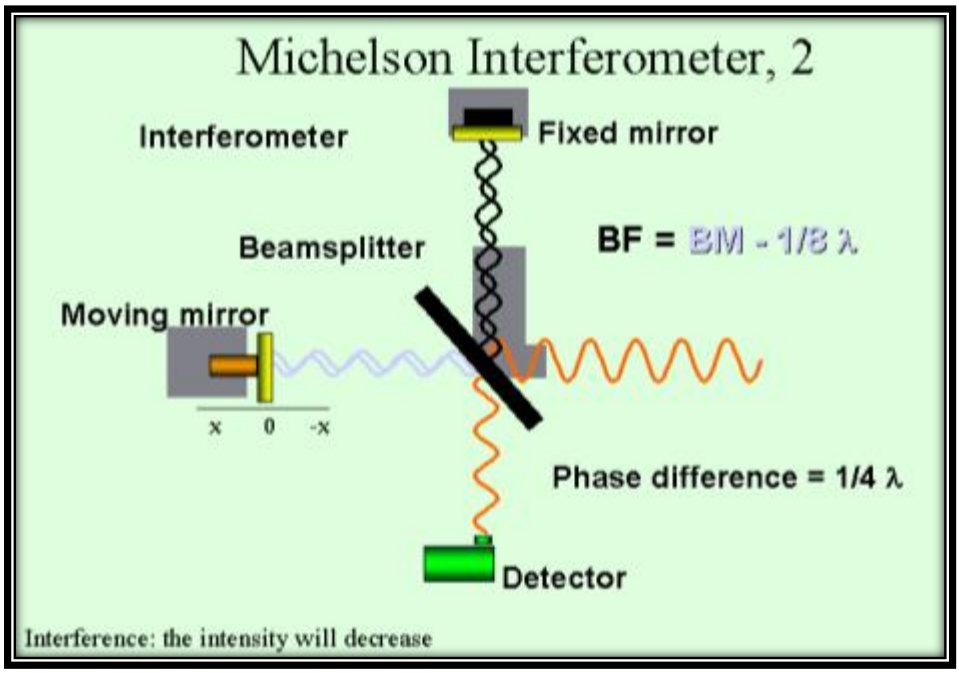

Figure 2.2 Schematic illustration of Michelson interferometer constructed of a fixed mirror, a moving mirror, a beamsplitter and a detector.

A typical FT-IR spectrum is shown in Figure 2.3(b), and the peaks at 2850 and 2917 cm^{-1} are identified as the symmetric and asymmetric vibration of CH_2 and CH_3 groups, respectively.[164] The specific peak positions verify the presence of the stearic acid on the surface of MnO_2 nanotubes after surfactant coating. Figure 2.3(a) shows the surface modification leading to dramatic change in the wettability of as-prepared MTA membrane from a nearly superhydrophilic CA of 6° to a superhydrophobic CA of 160.9° with a small slide angle (<5°).

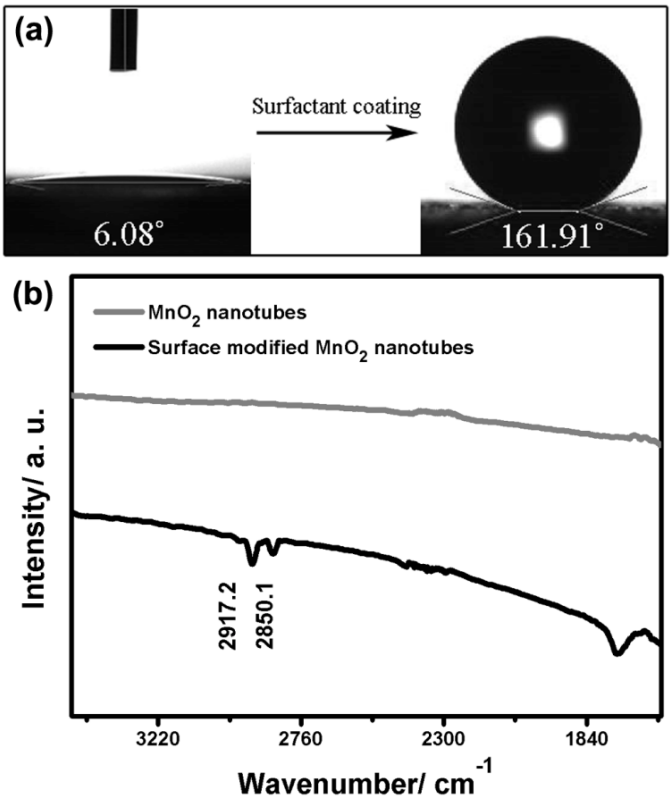

Figure 2.3 (a) Photos of water droplets on an as-prepared MTA membrane with a water CA of 6.08° and on a surface modified superhydrophobic MTA membrane with a water CA of 161.8°. (b) FT-IR spectra of MTA and surface modified MTA membranes.

2.2.2. Contact Angle Measurement

Contact angles are the commonly seen physical manifestation of the more fundamental concepts of surface energy and surface tension. The data of contact angle/ surface energy measurements are valuable in fundamental research and industrial applications, including determining surface cleanliness, bondability, wettability, adhesion, biocompatibility and coating quality. In general, two different approaches are utilized to measure contact angles of solid surface, optical tensiometry (goniometry) and force tensiometry. Optical tensiometry involves the observation of a sessile drop of test liquid on a solid substrate. While force tensiometry engages measuring the forces of interaction as a solid is in contact with a test liquid. Analysis of the shape of a drop of test liquid loaded on a solid surface is the basis for optical tensiometry. The basic elements of an optical tensiometer include light source, sample stage, lens, motorized syringe and image capture shown in Figure 2.4. The drop under analysis is observed in the side view; the optical tensiometer then employs a camera and a computer for detecting the droplet shape and extracting the contact angle. Contact angle can be assessed directly by measuring the angle formed between the solid and the tangent to the drop surface. The contact angle analysis software in general assumes the drop is part of a sphere, shown in

$$\theta = 90 - \tan^{-1}\left(\frac{r-b}{\sqrt{2rb-b^2}}\right) \tag{2.1}$$

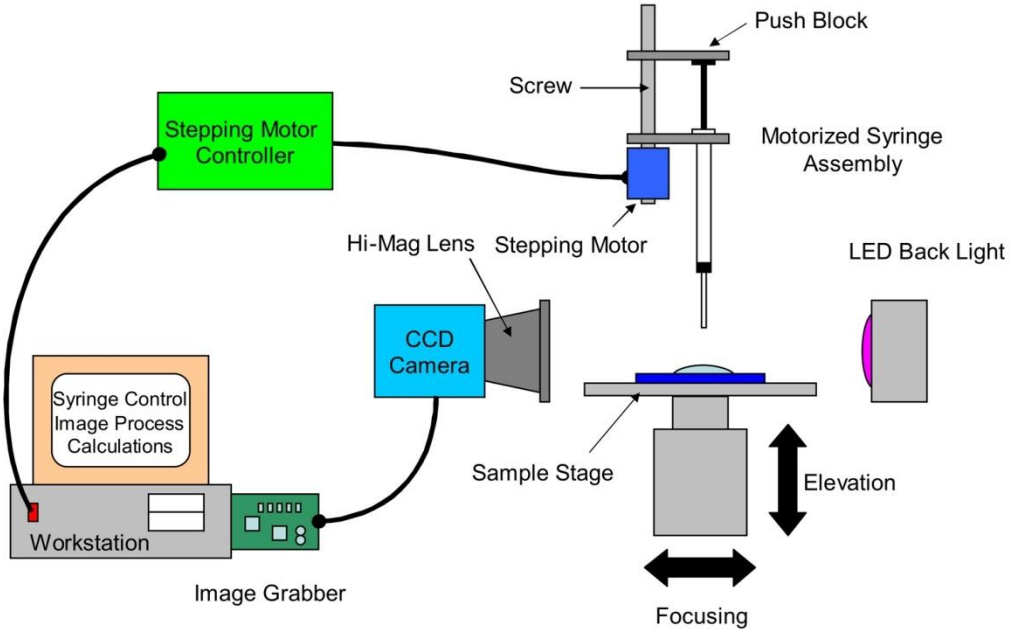

Figure 2.4 The basic elements of an optical tensiometer include light source, sample stage, lens, motorized syringe and image capture.

The size of the drop must be chosen such that, on one hand, the influence of evaporation on the drop shape can be neglected during the time scale of the experiment under certain humidity. This condition limits the minimum drop size. On the other hand, the drop must be small enough so that it is not significantly deformed due to gravitational forces. The deviation of CA measurements becomes obvious under gravitation in the case of water drops on superhydrophobic surfaces. The latter point is usually regarded satisfied if the diameter of drops is below the capillary length of the respective liquid.[77] The capillary length, λ_C, is defined as:

$$\lambda_C = \sqrt{\frac{\gamma_{lg}}{\rho g}} \tag{2.2}$$

Where ρ is the liquid density and g is the gravitational acceleration. For drop diameter below the critical value of λ_C, surface tension is assumed to be dominant. The capillary length for water is about 2.7 mm, which thus represents the upper limit in size for water drops. Therefore, all experiments for CA measurements were carried out by using a 3 μL deionized water droplet (1.8M Ω/cm) at ambient temperature with a relative humidity of around 60%. The values reported are averages of more than five measurements made on different areas of the sample surface.

The values of advancing/receding angles are important data to characterize the dynamic wetting property of a surface. The production of drops with advanced and receded edges, whereby the advancing and receding angles can be measured, involves three strategies. Firstly, drops can be made to have advanced edges by addition of liquid. Receded edges may be obtained by allowing sufficient evaporation or by withdrawing liquid from the drop. Alternatively, both advanced and receded edges are produced when the stage on which the solid is held is tilted to the point of incipient motion. Using an instrument with high speed image capture capabilities, shapes of drops in motion may be analyzed. Finally, advancing/receding angles can be obtained by using a drag-to-move method.[116] The water droplets were dragged to slide on the surface to measure the advancing angle (on the downhill side) and receding angle (on the uphill side). In this

process, we used 3 μL water droplets and kept the same distance between the needle and the surface (1.76 ± 0.04 mm) for all the measurements.

2.2.3. Normal Force Measurement

Normally, the liquid-solid adhesion is characterized by the CA hysteresis, which can be influenced by the surface structure, chemical heterogeneity. Jiang *et al.* [117] have pointed out that the measurement of CA hysteresis only indicates effects of adhesion along the shear direction (Figure 2.5 A). To thoroughly understand the adhesion behavior between liquid and solid, the normal adhesive force should be also considered. Particularly for high-adhesion superhydrophobic surfaces, water drops stick to them rather than roll or slide off, even if the surfaces is tilted a large angle or turned upside down. In this case, the water adhesion on surfaces can be assessed by the normal adhesion force measured by a high-sensitive balance system. As shown in Figure 2.5 B, a liquid droplet is suspended on the balance system, and the surface is controlled to contact and withdraw. The force required to pull the droplet away from the surface is thought to be the normal adhesion force between liquid and solid. This force is related to the preloading approaches, the volume of drops, etc.

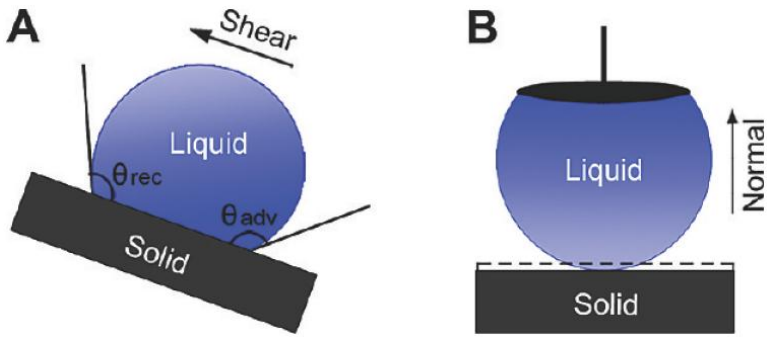

Figure 2.5 Schematic illustration of two models for adhesion characterization: (A) CAH measurement, indicating an adhesion along the shear direction; (B) NAF measurement, indicating an adhesion along the normal direction (Reprinted with permission from ref. [117])

The Processor Tensiometer System K14 (inset of Figure 2.6) is designed to measure liquid surface tension by ring method and Wilhelmy plate method etc. The core gear in this equipment is an electrical balance with the maximum loading capacity of 5000 *mg* and readability of 0.001 *mg*. According to the experimental data in the literatures, the largest water adhesion of 3μL volume on superhydrophobic surfaces is around 80μN. Hence, the electrical balance in the Processor Tensiometer System K14 is fairly capable to measure the normal adhesion. This process is similar to the method previous study used to characterize PS nanotube array.[48] Instead of a small metal ring, a TEM copper grid (SPI Supplies) was employed to contact and hold the water droplet. The copper grid exhibits suitable wetting condition with CA of 131.0°, and it can provide sufficient water adhesion to grab water drops off the measured MnO_2 samples.

This process was monitored by a video camera and the final data plotted reduced the gravity of a water droplet.

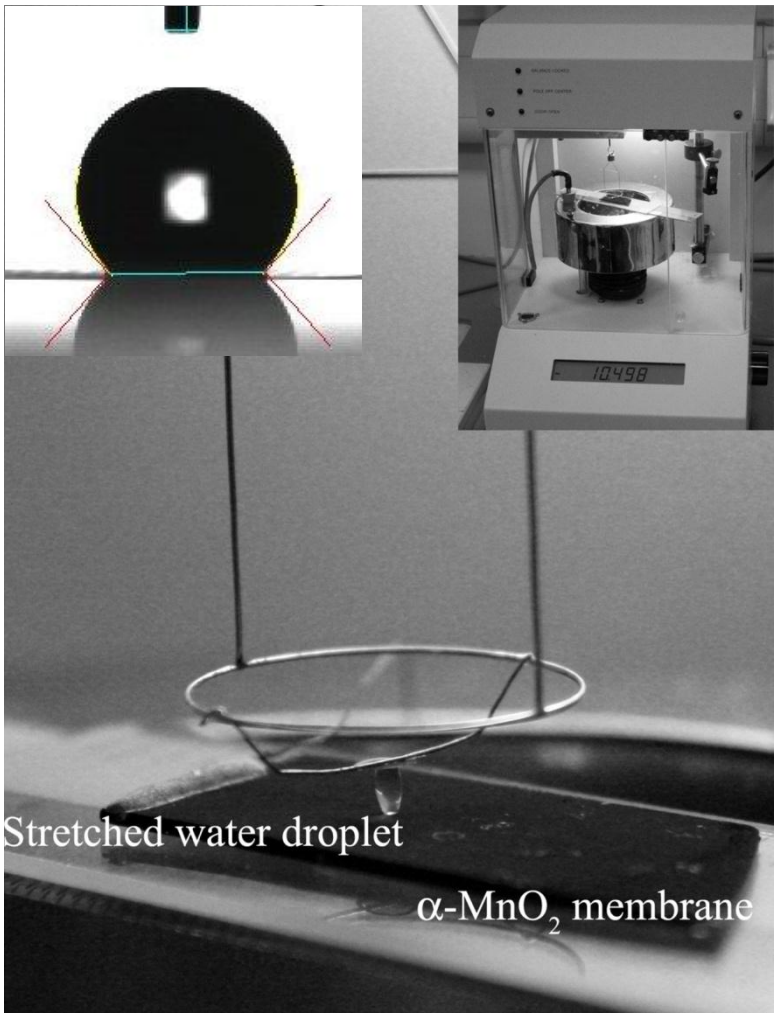

Figure 2.6 Self-designed setup for normal adhesion measurement. Photo of a stretched water droplet between a Cu grid hung on the pt ring and α-MnO_2 membranes. The inset on the left showing wettability of the Cu grid with a CA of 131.0 °and the right inset is a photo of the Processor Tensiometer System K14.

Figure 2.7 displays a typical force-distance curve for the normal force measurement on a MnO_2 film with small mesh-like structure. After the water droplet was loaded on the film, it was first brought into contact with the grid. Then the film was moved away from the grid at a rate of 0.02 mm s^{-1}, and the measured force increased gradually, reaching a maximum just before the detachment of the water droplet. Subsequently, the measured force decreased rapidly as the water droplet broke away from the film.

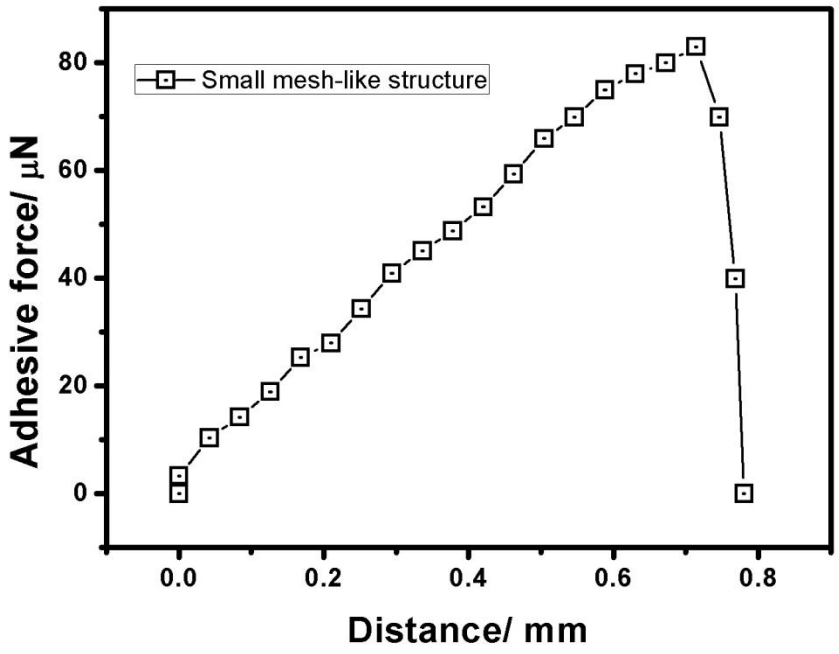

Figure 2.7 Force-distance curve as a water droplet is stretched and pulled off the substrate.

Chapter 3

Robust Superhydrophobic Surface

In this chapter, we study how to synthesize robust superhydrophobic surfaces based on MnO_2 films with various morphologies. The term of robustness relates to the stability of superhydrophobic surfaces and it is mostly referred to the dynamic wetting properties on superhydrophobic surfaces. Dynamic effects, such as the bouncing and vibration of a droplet, can destroy the composite solid-air-liquid interface. Therefore, the impact pressure of a bouncing droplet and the inertia force of a vibrating droplet affect the transition from a solid-air-liquid interface to a solid-liquid interface. Hence, the superhydrophobic states change and the overall wettability evolves as well. Since the stability is crucial for the functional superhydrophobic surfaces and lab-on-chip devices in real applications, it is necessary to study the dynamic effect of droplets under various system parameters (external pressure, impact velocity, frequency and amplitude of vibration).

3.1. Introduction

Lotus leaves exhibit extreme hydrophobicity, making the rain droplets falling off on their surfaces effortlessly. This impressive water-repellent property can be ascribed to its hierarchical structure: numbers of papillae covered with countless nanohairs.[118] Such complex micro/nanoscopic architecture of the surface has been utilized in a wide range of potential applications, including raindrop self-cleaning, oil spill cleanup, water-capture devices, laboratory-on-a-chip devices, bioinspired geckos/mussels feet and functional interface for cell and tissue engineering. In practical applications of superhydrophobic surfaces, surfaces should maintain their ability to repel penetrating of droplets under dynamic conditions. For example, bouncing droplet studies are of interest in rainwater and spray on surfaces, and vibrating droplet studies are of interest in micro/nanofluidics and microelectronics. These studies are of scientific interest in probing energy barriers responsible for contact angle hysteresis.[119]

The mechanism of these structure induced superhydrophobicity is addressed by Wenzel's and Cassie's theories. Wenzel introduced nondimentional surface roughness *r* to address the roughness enhanced superhydrophobicity. In his theory the measured contact angle is expressed as $\cos\theta = r\cos\theta_0$ (θ is the measured contact angle, θ_0 is the angle on a smooth surface and *r* is the ratio of the actual area of liquid-solid contact to the projected area on the horizontal plane). Cassie, in turn, considered drops were supported by a composite surface composed of

solid and air where the air parts of the interface were considered as perfect non-wetting. In this case, the measured contact angle becomes: $\cos\theta = \Phi_s(\cos\theta_0 + 1) - 1$, where Φ_s is the fraction of solid in contact with the liquid. In reality, kinetic barriers may lead to a stabilization of drops in a wetting situation that is not the minimum-energy state. As a consequence, drops in both wetting states (Cassie and Wenzel) may appear on one and the same substrate. Patankar studied the Cassie-to-Wenzel transition theoretically for a model surface composed of regularly arranged posts. For a hydrophobic surface (i.e., θ_Y>90°), he found the initial impalement of a drop on the post structure to be associated with an increase in interfacial energy. Energy was then recovered as the drop made contact with the bottom of the post surface and liquid-air was replaced by liquid-solid interface. Following similar considerations, Nosonovsky and Bhushan derived an energy diagram for the Cassie-to-Wenzel transition where both states were separated by an energy barrier.[120]

However, those theories may encounter their limits as applied to interpret the contact angle hysteresis as well as water adhesion on surface and ignore the significance of the dual length-scale topography. Recently Gao *et al*. proposed that the hierarchical structures reduce the contact angle hysteresis by lowering the transition state energy between metastable states from the kinetics perspective; from thermodynamic perspective, the increasing of the Laplace pressure makes water droplet harder to penetrate into the structures, yielding drag reduction.[10]

In addition, Lafuma *et al.* mentioned that a hierarchical structure did not only enhance the hydrophobicity, it also stabilized the Cassie regime, and thus favored water repellency.[86] Bo *et al*. designed a criterion for a robust hydrophobic rough surface on which the apparent contact angle would not change as a result of an external disturbance.[45] In particular, the overhang structure which generates a net force for lifting a liquid droplet upward has attracted increasing interests. [121-124]

3.2. Result and Dicussion

3.2.1. Structural Characterization of NPA

The hierarchical MnO_2 nanopropeller array (NPA) in this work was grown by a two-step hydrothermal method. In a typical experimental procedure, 2.5 mM $KMnO_4$ and 10 mM concentrated HCl were added to 45 mL deionized water to form the precursor solution, which was then transferred into a teflon-lined stainless steel autoclave with a capacity of 100 mL. To grow high oriented structure, 1×3 cm^2 Si (111) wafers were used as the substrates. The autoclave was sealed and hydrothermally treated at 140 °C for 14 h to obtain MnO_2 nanotube array (MTA). (Step I). The synthesized MTA film was used as the substrate; following the same procedure NPA was obtained. (Step II) To achieve the superhydrophobicity, as-prepared MnO2 films was immersed the in a methanol solution of hydrolyzed 1wt% PFOTES for 1 h at room temperature, and subsequently heated at 140 °C for 1 h.

Figure 3.1(a) and (b) show a top view of the well-aligned NPA on a silicon substrate. Each column of nanopropeller arrays consists of four arrays of small nanotubes of 1.1±0.09 μm in length. Columns of the nanopropellers remain their fourfold arrays of parallel small nanotubes around the central nanotubes. On each column, the arrays of the small nanotubes are at 90 °, corresponding to the fourfold symmetry of the center nanotube.

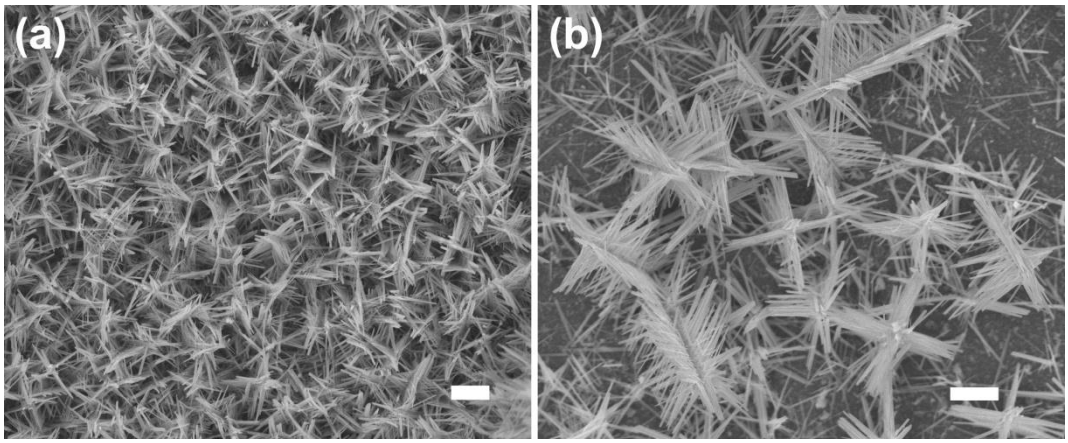

Figure 3.1 Low and high magnification SEM images of MnO_2 film with hierarchical nanopropeller structure. The scale bar is 1 μm.

The representative hollow nanostructure of the hierarchical NPA with a small nanotube growing from the side wall of a large nanotube is clearly shown in Figure 3.2(a-c). The diameter of the large tubes in the center is about 100 nm and the diameter of the small tubes on the side walls is about 40 nm. The angle between the large and small tubes is about 75 °, which agrees well to the tilting angle between the MnO_2 nanotube axis and the plane of the Si(111) substrate. The tilting angle of α-MnO_2 nanotubes might be formed during re-crystallization process from birnessite-type MnO_2 nanowalls[125, 126] and further investigation is required to reveal the mechanism. The inset of Figure 3.2(c) shows the selected area electron diffraction (SAED) of the sample. High-resolution transmission electron microscopy (HRTEM) image shown in Figure 3.2(d) reveals lattice spacing about 0.5 nm for (200) planes of the large and small tetragonal α-MnO_2 structure along the tubes. The SAED pattern and HRTEM analysis reveal that both the large and small nanotube axis are along the [001] direction (c axis).

These TEM investigations indicate the high quality single-crystalline natures of the obtained NPA and the results are in consistent with XRD pattern.

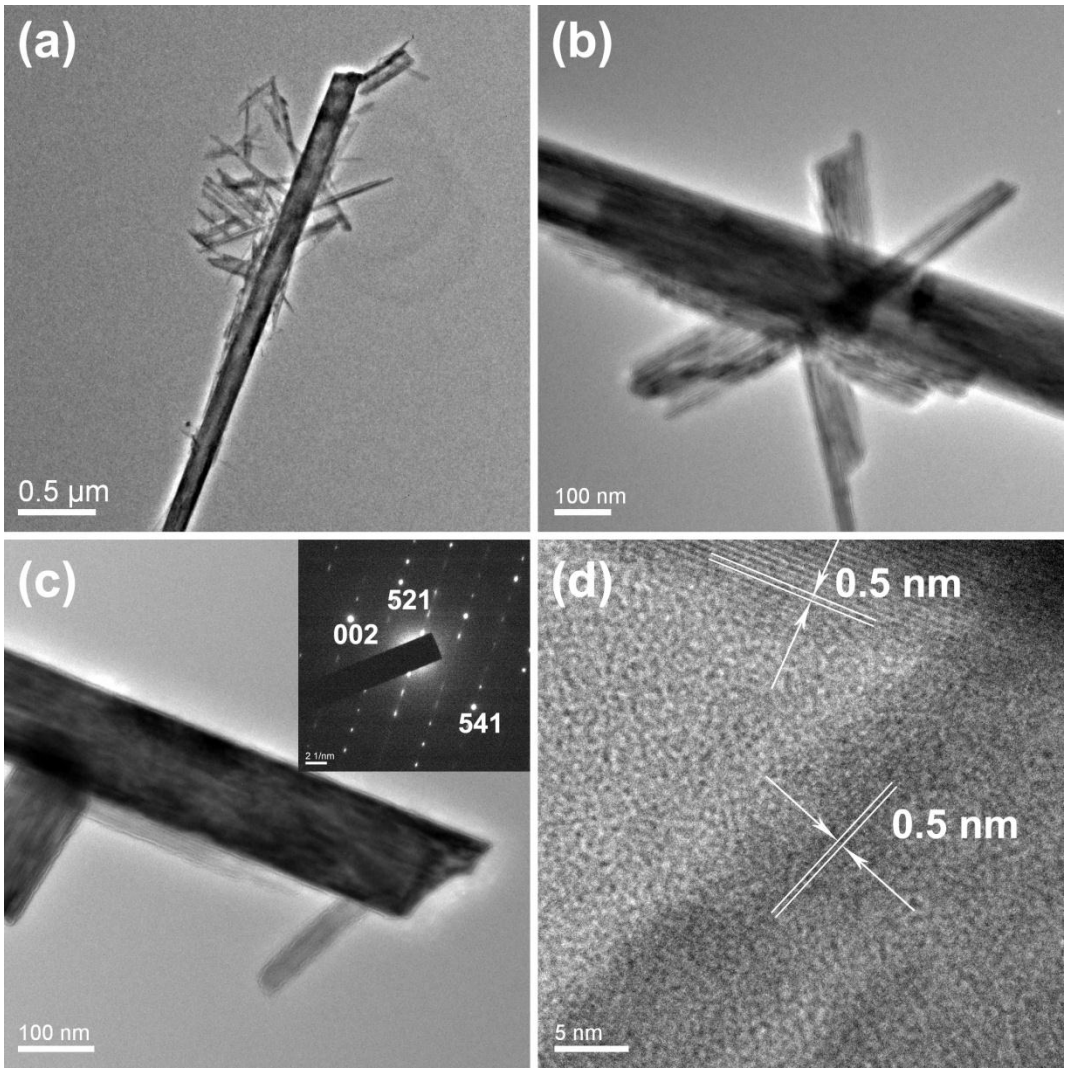

Figure 3.2 (a-c) TEM images of a representative hollow nanostructure of the hierarchical NPA with a small nanotube growing from the side wall of a large nanotube. Inset of (c) SAED pattern of the NPA. (d) HRTEM image of NPA focusing on the conjunction of the large nanotube and the small one.

The phase purity and crystal structure of the MnO_2 NPA have been examined by X-ray diffraction (XRD). The result shows that NPA has the same α-MnO_2 crystal phase structure as the MnO_2 nanotube membrane. As shown in Figure 3.3, all the diffraction peaks can be exclusively indexed as the tetragonal α-MnO_2 (JCPDS 44-0141), and no other impurities are observed.

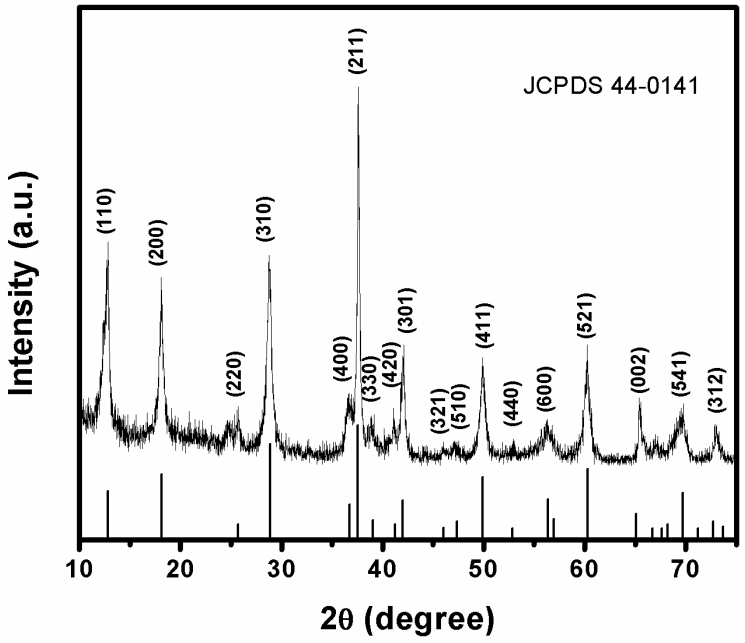

Figure 3.3 XRD pattern of the α-MnO_2 NPA.

3.2.2. Growth Mechanism of NPA and BCS

In order to elucidate the formation mechanism of the α-MnO_2 NPA, time dependent evolution of the morphology has been investigated. Top view SEM image in Figure 3.4(a) shows the as-prepared single layer α-MnO_2 nanotube array (MTA) synthesized in the Step I of CBD. The open end and the square cross-section of the nanotubes can be clearly observed. The average length is 2 μm; the outer diameter and wall thickness are 103 nm and 23 nm, respectively. In the Step II of CBD, the MTA film was used as a template to synthesize α-MnO_2 NPA. With a reaction time of 135 min, the MTA first grew into ball cactus-like structure (BCS). The top-view SEM image presented in Figure 3.4(b) shows that large scale BCS MnO_2 film has been successfully deposited on the Si(111) substrate. From the magnified view (Figure 3.5), the original open ends and side walls of nanotubes are covered by nanowalls. The nanowalls are thin flakes with the thickness of several to 20 nm. They connect and cross to form mesh-like structure on each post with the diameter from 0.6 to 1.5 μm, depending on the growth time of second step in the BCD process. The inset of Figure 3.4(b) indicates that the thin flasks grow on the surface of every individual nanotube rather than a layer of flasks covering the surface of MTA membrane. When prolonging the reaction time, the thin flasks dissolved and re-crystallized on the surface of each nanotube on MTA membrane, forming fourfold short nanorods array along each side of nanotubes, as shown in Figure 3.4(c). By increasing the reaction time, the length of nanorods increased and the prototype of NPA was

formed, as shown in Figure 3.4(d). The whole formation process of α-MnO_2 NPA is schematically illustrated in Figure 3.6. The nanowalls with amorphous structure are first formed on the nanotube, and then re-crystallize into short α-MnO_2 nanorods, which elongate along [001] direction.

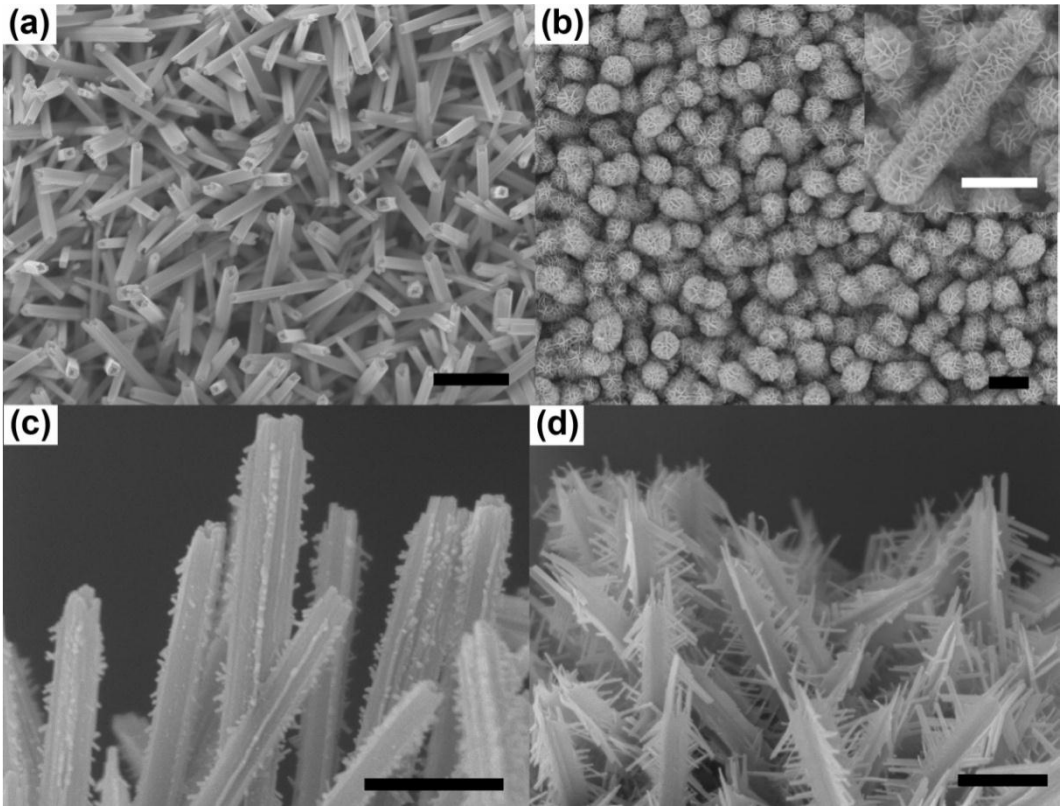

Figure 3.4 (a) Top-view SEM image of α-MnO_2 MTA. (b) Top-view SEM image of BCS and inset showing sides of nanotubes are covered by nanowalls. (c) Side-view SEM image of short nanorods growing on nanotube by re-crystallization of nanowalls. (d) Side-view SEM image of long nanorods growing on nanotube with increased reaction time. The scale bar is 1μm in a and b and 500nm in c and d.

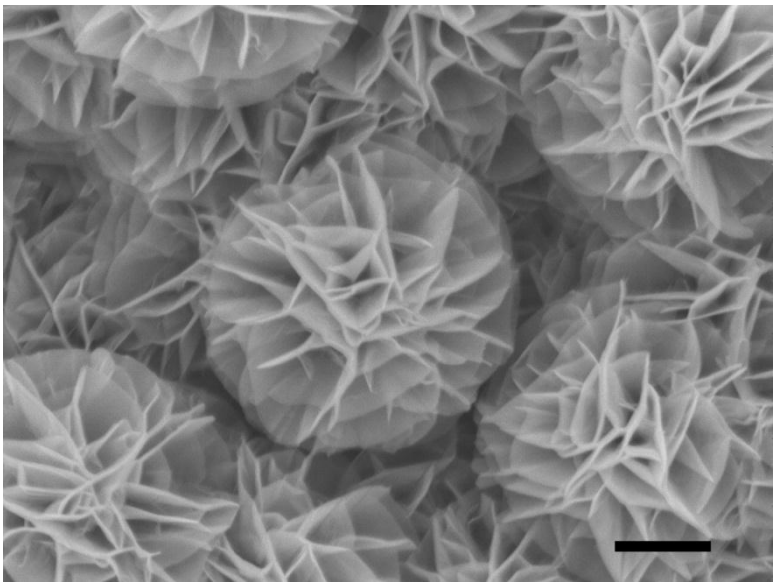

Figure 3.5 Top-view SEM image of BCS. The scale bar is 500 nm.

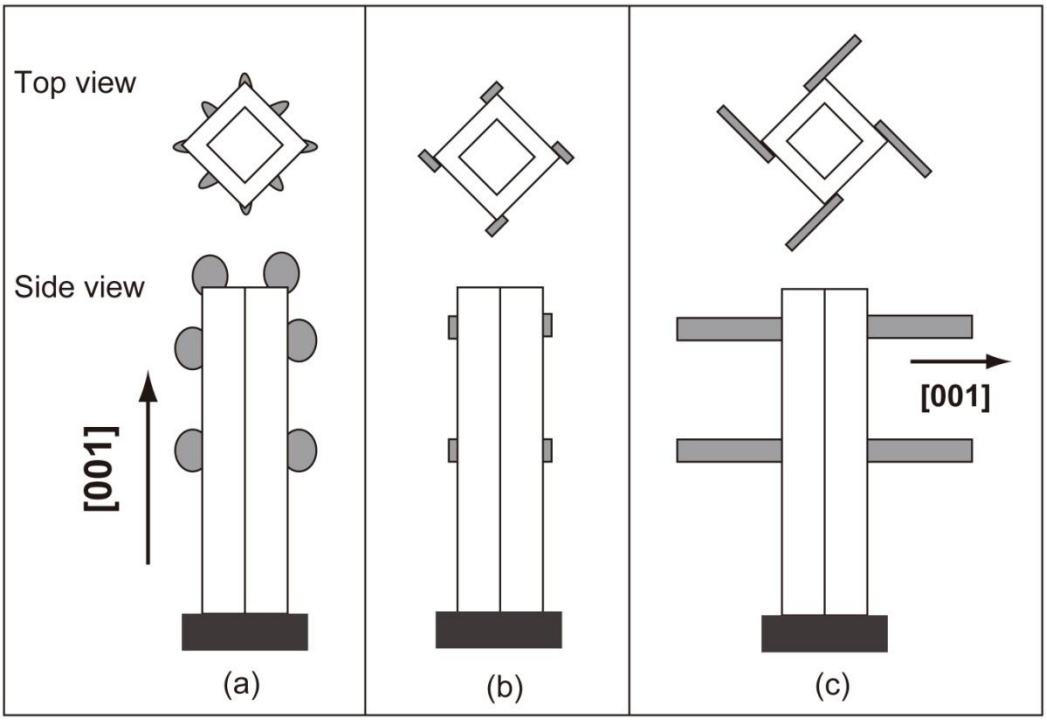

Figure 3.6 Schematic growth process of the α-MnO_2 NPA. The diagram shows only one column of NPA for simplicity of illustration.

According to the topographies of MnO_2 obtained from SEM images, we suggest that the growth mechanisms of large nanotubes in the MTA on Si(111) substrate and the small nanotubes as the sub-structure of NPA follow the similar process of anisotropic growth and etching. However, the growth of large nanotubes on Si(111) substrate underwent re-crystallization process from birnessite-type MnO_2 nanowalls,[125, 126] and this type of MnO_2 was not found in the small nanotubes formation. The TEM image of the representative BCS structure with nanowalls vertically growing on the nanotube and SAED results are shown in Figure 3.7. The SAED was performed in different area of the sample and the locations are marked in Figure 3.7(d). The patterns in SAED results shown in Figure 3.7 (a-c) indicate the amorphous structure MnO_2, instead of birnessite-type MnO_2 found in the MTA growth. Note that the SAED results obtained from the side and the top (Figure 3.7 (c)) of nanotube have different orientations of bright arcs, suggesting the preferred growth direction. The SAED result in Figure 3.7 (a) was obtained by shedding X-ray on BCS located at the circle marked as "a" in Figure 3.7(d). Similarly SAED results of Figure 3.7 (b) and (c) are corresponding to circle b and c in Figure 3.7(d). Note that the SAED result in Figure 3.7 (b) shows a blur circle pattern combined with crystal diffraction pattern shed from the α-MnO_2 nanotube.

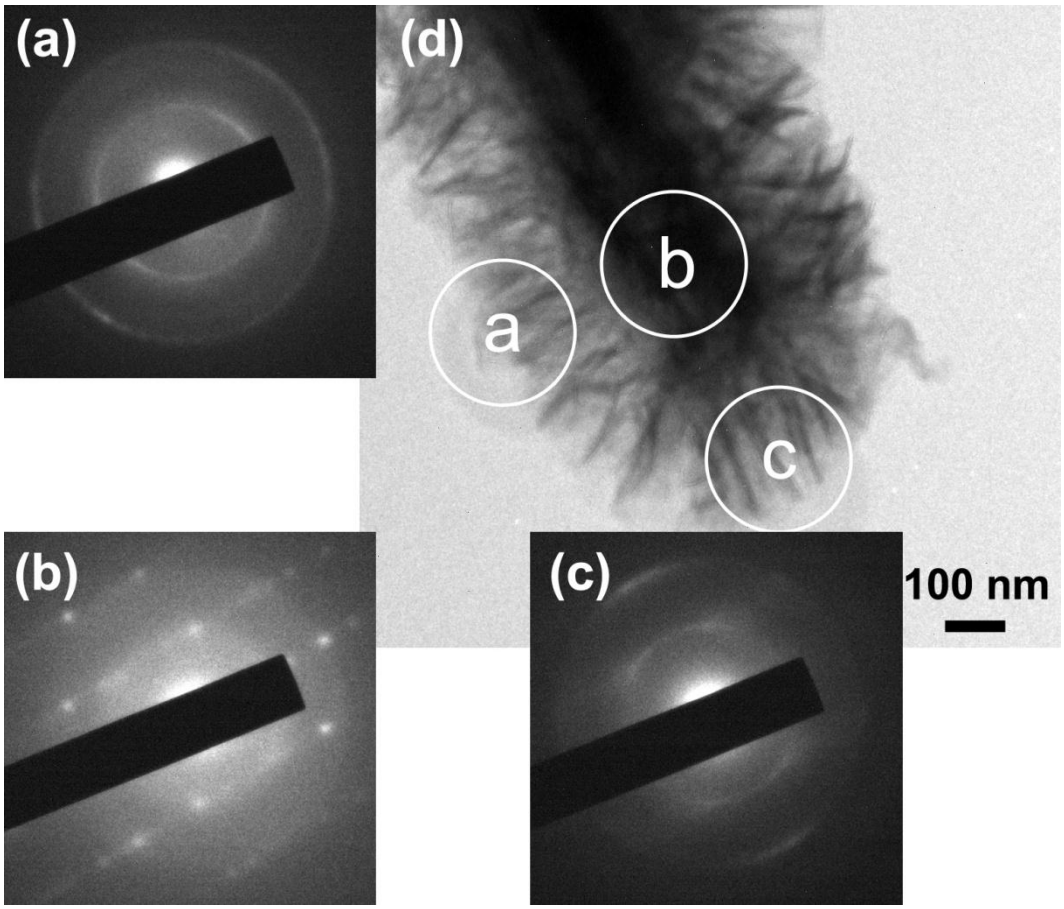

Figure 3.7 TEM image (d) and SAED patterns (a-c) in different locations of the representative BCS structure with nanowalls vertically growing on the nanotube.

3.2.3. MnO_2 Nanowire Membrane

The top-view SEM image presented in Figure 3.8(a) shows that MnO_2 film with nanowire structure (NWS) have been successfully deposited on the Si(111) substrate in a large scale. The magnified SEM image in Figure 3.8(b) shows that top ends of several nanowires are bundled and nanostructures in other morphologies are not observed in the sample, indicating the sample has a high morphological purity. Surprisingly, TEM images of NWS shown in Figure 3.9(a-d) reveal typical hollow nanostructures. In addition, the NWS shows a needle-like shape with a sharp tip of about 23 nm in diameter and the other end of 88 nm in diameter. The length of the nanowire is about 2.5 μm. The SAED pattern and HRTEM in Figure 3.9(e) and (f) analysis reveal that the nanowire axis is along the [001] direction (c axis). These TEM investigations also indicate the high quality, single-crystalline nature of the obtained NWS.

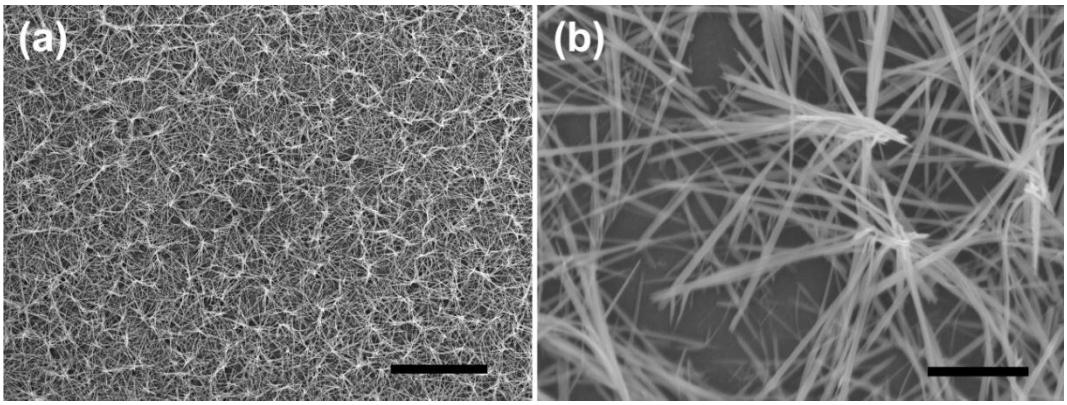

Figure 3.8 Low and high magnification SEM images of MnO_2 film with hierarchical nanowire structure. The scale bar in (a) is 10 μm and in (b) is 1 μm.

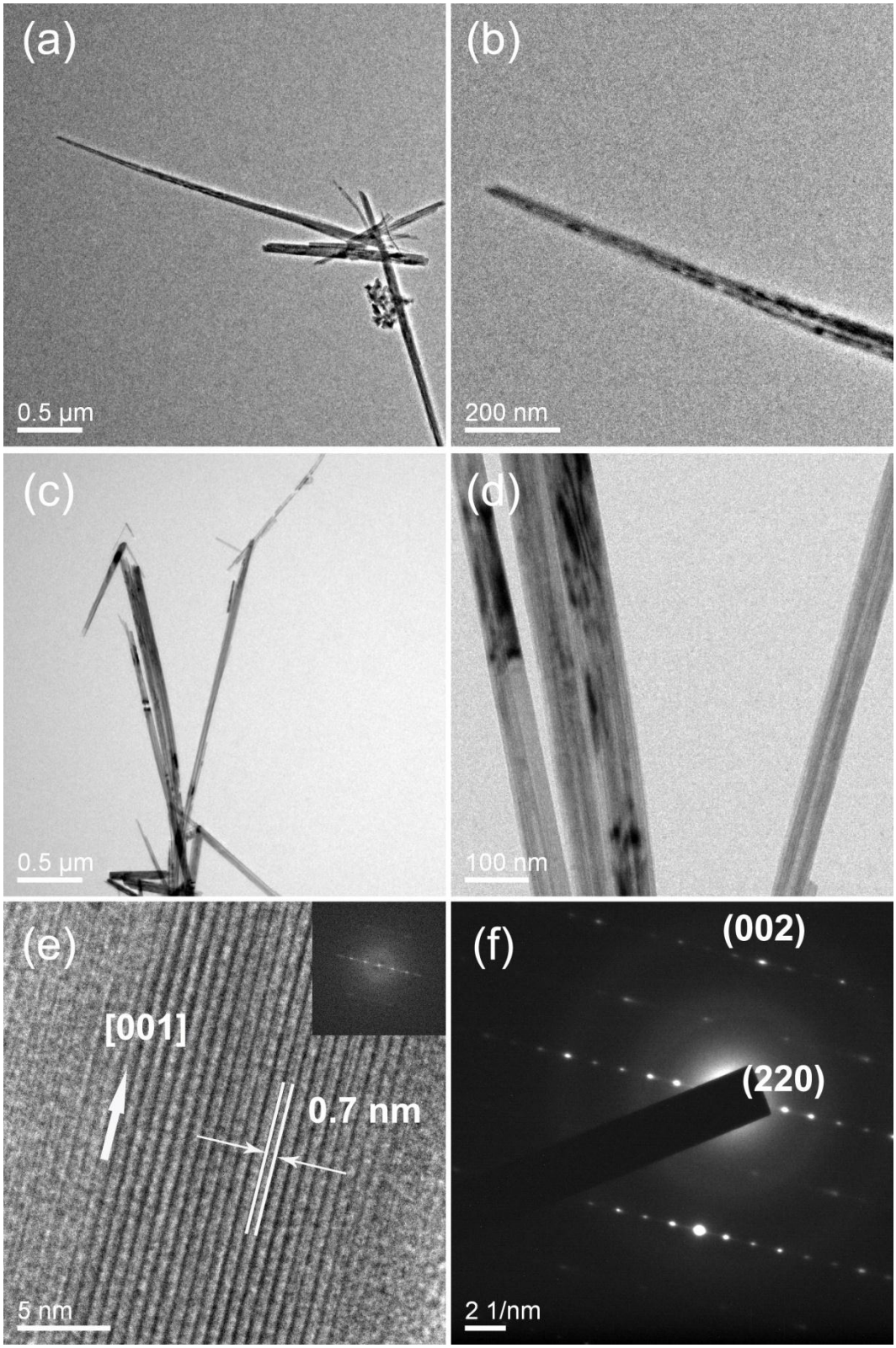

Figure 3.9 (a-d) TEM images of a representative hollow nanostructure of the MnO_2 NWS. (e) SAED pattern of the NWS. (f) HRTEM image of NWS.

3.3. Robustness Characterization

Theoretically, the energy barrier can be used to characterize the stability or the robustness of the superhydrophobicity. From theory, for a given r and ϕ, the Wenzel state is energetically favored if the contact angle on a smooth material, θ_Y, is below a critical value θ_{Crit}. θ_{Crit} follows by equating the Wenzel and the Cassie equation: $r\cos\theta_{Crit} = \phi_{Crit}\cos\phi_{Crit} + \phi - 1$ as derived in chapter 1. While researches use external pressure experimentally to control the Cassie's and Wenzel's state transition, in a way to characterize the robustness of the superhydrophobicity. [41, 99, 124, 127]

In a squeezing test, a water droplet was placed between two identical MnO_2 nanostructured NPA substrates which were controlled to compress by using a micrometric screw. This process was recorded by contact angle analyzer; the contact angle, radius of the droplet R, and the gap h between two substrates were ready to be measured (inset of Figure 3.10). In addition, the external pressure can be calculated based on Laplace-Young equation:

$$\Delta P = \gamma\left(\frac{1}{R_x} + \frac{1}{R_x}\right) = \gamma\left(\frac{1}{R} + \frac{2|\cos\theta|}{h}\right) \tag{3.1}$$

Where R_x and R_y are the radii of curvature in each axis that is parallel to the surface; h is the distance between the two substrates; R is the radius of the water droplet in the horizontal direction; θ is the water contact angle.

The strong robustness of the substrates was verified that even when a droplet was squeezed and forced to wet the nanostructure of NPA substrates, the contact angle remained large and the droplet sprang back to the spherical shape when released from squeezing. The quantitative correlation between the contact angles and the squeezed pressures was plotted in Figure 3.10(a), demonstrating that the contact angle hardly changed as the external pressure increased to 500 pa. The corresponding compress force was also derived, shown in the right y axis in Figure 3.10(a). A series of capturing photos of squeezed water droplets are shown in Figure 3.10(b).

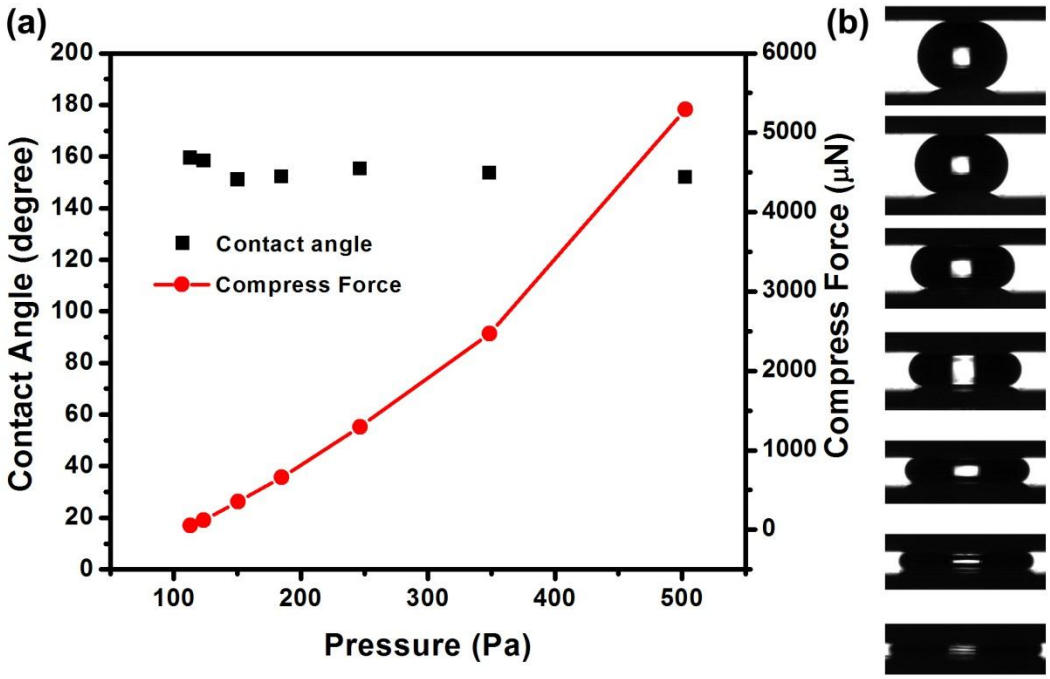

Figure 3.10 (a) A plot of correlation between the contact angles and the squeezed pressures. (b) Photos of the corresponding squeezed water droplets.

3.4. Conclusion

A robust superhydrophobic MnO_2 film with a structure of hierarchical nanopropeller array (NPA) was synthesized by a two-step hydrothermal method. Columns of the nanopropellers remain as fourfold arrays of parallel small nanotubes around the central nanotubes. In order to elucidate the formation mechanism of the NPA, time-dependent evolution of the morphology has been investigated. It is found that those tubes are formed through anisotropic growth and etching process. In addition, the robustness of superhydrophobicity was confirmed by the water droplet squeezing test of squeezing a water droplet within two NPA substrates. The results showed that the NPA film maintained its superhydrophobicity under the pressure of 500 Pa, which was sufficient to address bouncing droplets and/or vibrating droplets in superhydrophobic state. This facile route of fabricating superhydrophobic MnO_2 film with hierarchical nanostructures is expected to be applicable in micro/nanofluidics system and lab-on-chip devices.

Chapter 4

Pattern-Dependent Tunable Adhesion

In this chapter, tuning the adhesive force on a superhydrophobic MnO_2 nanostructured film was achieved by fabricating different patterns including meshlike, ball cactus-like and tilted nanorod structures. The marvelous modulation range of the adhesive forces from 132.4 to nearly 0 μN endows these superhydrophobic surfaces with extraordinarily different dynamic properties of water droplet. This pattern-dependent adhesive property is attributed to the kinetic barrier difference resulting the different continuity of the three-interface contact line. This finding will help to provide the general strategies for the adhesion adjustment on superhydrophobic surfaces.

4.1. Introduction

Superhydrophobic surfaces such as lotus leaves exhibit a large water contact angle (CA) of greater than 150° and a small critical tilting angle (TA) of less than 5°.[1, 77, 128, 129] The biomimetic synthesis of superhydrophobic surfaces has paved the way for both fundamental research and applications such as raindrop self-cleaning and oil spill cleanup.[3, 130, 131] Recently, special attention has been focused on the strong adhesive superhydrophobic or more properly superhydrophobic-like surfaces that enable a nearly spherical water droplet to be firmly pinned on the surfaces.[26, 132-136] Despite a debate on the definition of this kind of superhydrophobicity,[137] the pinning effect resulting from a large CA and TA on a superhydrophobic surface has attracted a large amount of attention. Recently, surfaces of this type having tunable adhesion[138-141] have attracted more interest because the tunable adhesion allows the manipulation of water droplets on superhydrophobic surfaces. They are expected to have particular applications in open microdroplet devices with respect to increasing the need for controlled transport of small volumes of liquids in localized chemical reactions, biochemical separation, bio/chem analysis assay, single-molecule spectroscopy, and tissue engineering.[5, 7, 136]

The molecular interaction, the solid-liquid contact manner, and the capillary effect collectively contribute to the adhesion of various surfaces.[48, 139-141] In general, two methods have been adopted to modulate the adhesion of

superhydrophobic surfaces: one is to change surface energy gradually[139, 141] the other is to design and fabricate the micro/nanopatterns by modulating the continuity of the three-phase contact line (TCL).[138, 140] Nevertheless, for the first approach, surfaces with different chemical groups may have a great influence on the surface-catalytic chemical reaction, and heterogeneous nucleation in crystallization.[142] In this respect, fabricating superhydrophobic surfaces with the same chemical materials becomes particularly interesting.

In this chapter, we will demonstrate a simple way to acquire superhydrophobic MnO_2 nanostructured films with tunable water adhesion by fabricating the different patterns of MnO_2 nanocrystallites. MnO_2 has increasingly attracted the attention because of its low cost, environmentally benign nature. Different nanostructures, ranging from nanowires, nanotubes, nano-sheets to hierarchical spheres and hollow urchins have been obtained experimentally.[108-111] According to the principles of roughness-enhanced superhydrophobicity[70] and TCL-continuity-related adhesive behavior,[83] there is the possibility to tune the adhesion over a broad range in terms of various nanostructures and morphologies of MnO_2 nanocrystallites. In this study, our aim is to explore the correlation between the microscopic pattern/nanostructure of the films and water adhesion and to identify the tuning mechanism.

4.2. Experimental Section

The different patterns of MnO_2 films to be prepared are as follows: meshlike structure (MLS), ball cactus-like structure (BCS), and a tilted nanorod structure (TNS) (cf Figure 4.1), were synthesized on the basis of the hydrothermal method.[95, 126] In a typical experimental procedure, 2.5 mM $KMnO_4$ and 10 mM concentrated HCl were added to 45 mL deionized water to form the precursor solution, which was then transferred into a Teflon-lined stainless steel autoclave with a capacity of 100 mL. Two types of Si wafers (1×3 cm^2) with and without a Pt coating were used as the substrates to grow highly oriented MLS films of different mesh sizes. The autoclave was sealed and treated hydrothermally at 140 °C for 50 min to obtain MnO_2 MLS films. The TNS films were synthesized by extending the reaction time to 135 min to form the α-MnO_2 layer. By employing the TNS films as the substrate, BCS films were obtained via the same procedures as for MLS. All of the as-fabricated films were rinsed with deionized water and dried in air overnight. To achieve surface superhydrophobicity, the as-prepared MnO_2 films were immersed in a methanol solution of hydrolyzed 1 wt % PFOTES (*1H,1H,2H,2H*-perfluorooctyltriethoxysilane $(CF_3(CF_2)_5CH_2CH_2Si(OCH_2CH_3)_3)$ for 1 h at room temperature. The samples were rinsed with ethanol and subsequently heated to 140 °C for 1 h to remove nonbonded PFOTES molecules. The whole process is illustrated in Figure 4.1.

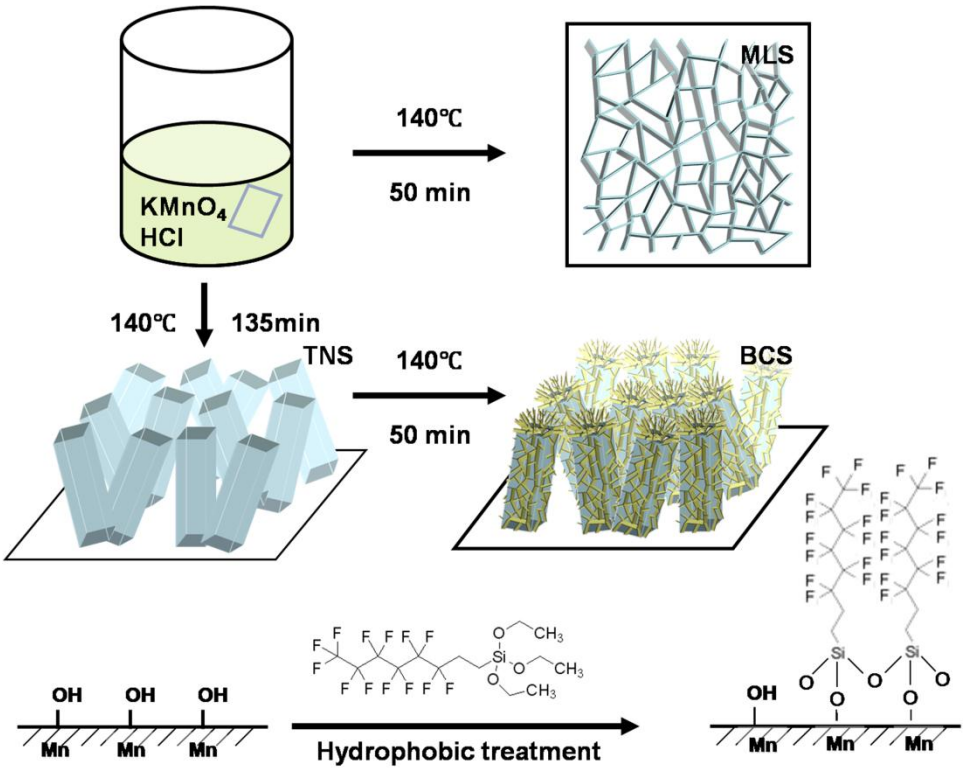

Figure 4.1 Schematic illustration of different morphologies of MnO_2 structures as to MLS, TNS, BCS and their synthesis conditions as well as surface treatment by PFOTES.

The topography and structure of MnO_2 films were examined by scanning electron microscopy (SEM, JEM 6700F, JEOL, Japan). The micrographs are given in Figure 4.3. The X-ray diffraction (XRD, PANalytical's X'Pert PRO MRD, The Netherlands) analysis shows that MLS MnO_2 belongs to monoclinic potassium birnessite (JCPDS 80-1098) (Figure 4.2(a)). The contact angle was measured by a contact angle analyzer (First Ten Ångstroms 1000B, America). The adhesion of the superhydrophobic films were characterized by the contact angle hysteresis (the difference between the advancing and receding angles), and the

direct measurement of the normal adhesive force was carried out by using a processor tensiometer system (K14 Kruss GmbH, Germany).

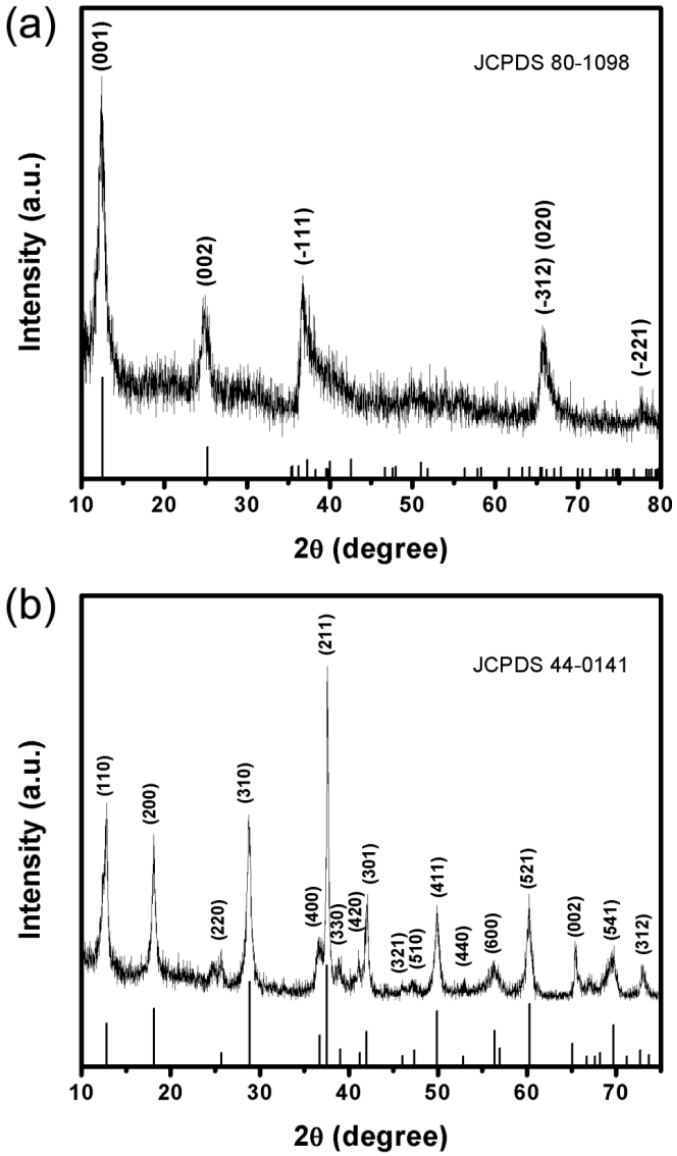

Figure 4.2 (a) XRD pattern of the birnessite-type MnO_2 powder. (b) XRD pattern of the α-MnO_2 nanorod powder.

4.3. Results and Discussion

Uniform MLS MnO_2 films with a mesh size of $(8.5 \pm 6)\times 10^4$ nm^2 were obtained on the Pt-coated Si(111) substrate (See Figure 4.3(a)). The nanowall sheets are connected and crossed, forming a mesh-like structure. The mesh size of the MLS film was found to be different on different substrates. A smaller mesh size ($(5.4 \pm 3)\times 10^3$ nm^2) MnO_2 film (S-MLS) was obtained on the Si (111) substrate without a Pt coating (Figure 4.3(b)). Notice that a longer hydrothermal reaction leads to the transformation of the birnessite phase to an α-MnO_2 phase (JCPDS 44-0141) (Figure 4.2(b)). Figure 4.3(c) shows α-MnO_2 film with tilted nanorod morphology, and the inset provides a higher-magnification SEM image of the nanorod with a tetragonal end. In addition, the MnO_2 nanowalls can also grow on the surface of the MnO_2 nanorod and finally, the hierarchical BCS film was obtained (Figure 4.3(d)). The high-magnification image shows that nanowall sheets are grown on both the top and the side of the individual nanorods.

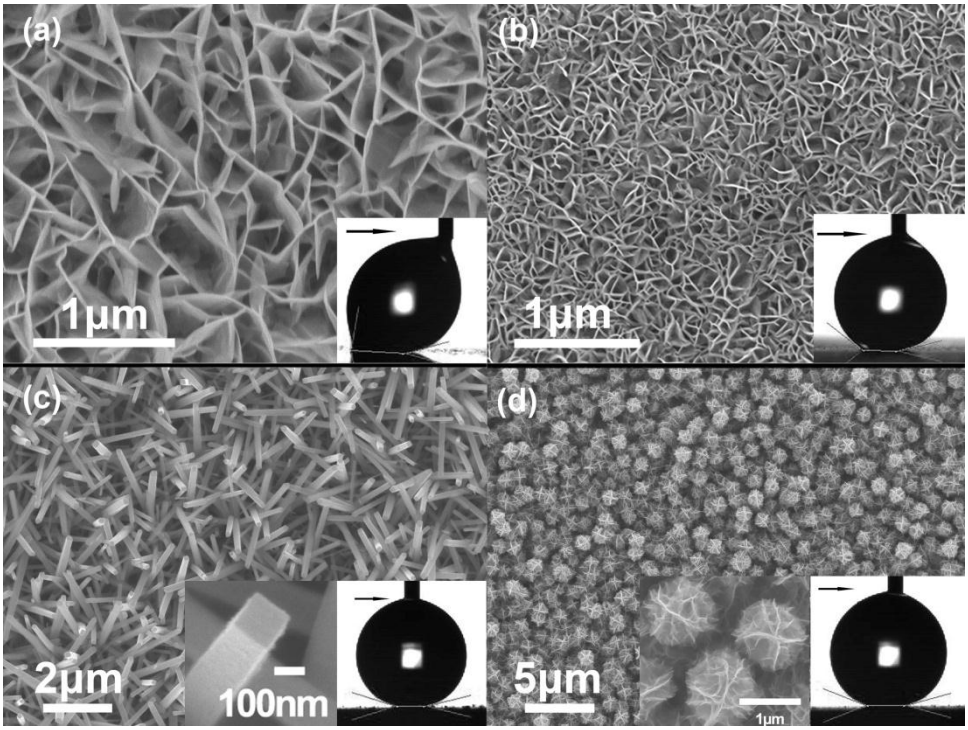

Figure 4.3 (a-d) SEM images of MnO_2 MLS, NTS, and BCS films. Insets show the dragging sessile water droplet. The black arrow indicates the drawing direction. (a-b) Large and small mesh size MLS. (c) TNS film. (d) BCS film.

The four different patterns of MnO_2 films all exhibit superhydrophobic feature with static contact angle larges larger than 150° after surface treatment with PFOTES. Such the superhydrophobicity can be explained by Cassie's theory assuming that the water droplet is supported by a composite surface composed of solid and air, where the air parts of the interface are considered to be perfect nonwetting. In this case, the measured static CA becomes $\cos\theta = \Phi_s(\cos\theta_0 + 1) - 1$, where Φ_s is the fraction of solid in contact with the liquid, θ_0 is the intrinsic CA on the flat surface. The intrinsic CA of PFOTES is 115 °.[140]

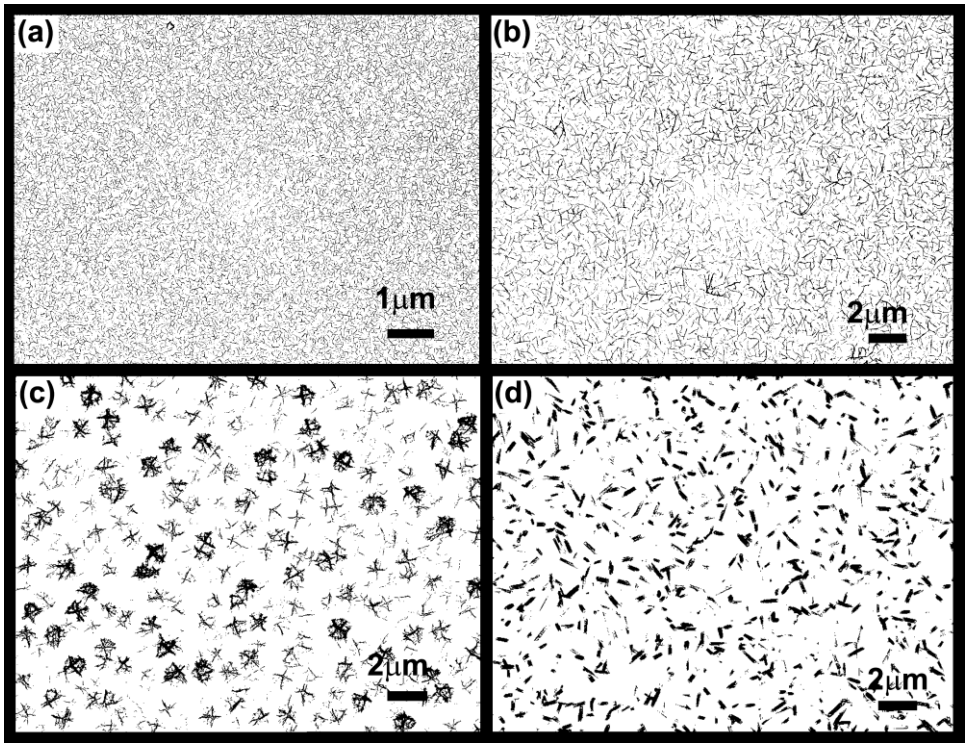

Figure 4.4 (a-d) High contrast black and white images converted from SEM micrographs of MnO_2 L-MLS, S-MLS, NTS, and BCS film, respectively.

To calculate Φ_s of MnO_2 films with different patterns, it is assumed that only the higher structures are in contact with a water droplet.[143] The fractional geometrical area of the top surface of MnO_2 films with the different patterns was calculated from top view SEM micrographs (Figure 4.3(c), (d) and Figure 4.5). The SEM images were converted to high-contrast black and white images through adjusting threshold (Figure 4.4). The increase in contrast eliminates lower structures, which were visible in the original SEM image. The higher structure led to white signals in the adjusted images. Furthermore, the possible relation between the contact angle and the roughness is strongly dependent on the scale of observation, which was unfortunately ignored in many studies.[144] Therefore,

the fractional geometrical area of the top nanostructured surface Φ_s of the different samples was measured on different scales shown in Table 4.1.

Table 4.1 Fractional geometrical area of the top nanostructured surfaces Φ_S of L-MLS, S-MLS, BCS, and TNS measured at different scales by high contrast black and white SEM images.

	Φ_S (%)		
	8μm×8μm	5μm×5μm	1μm×1μm
L-MLS	12.3±1	11.2±1	(15.2±3)
S-MLS	13.7±0.3	14.0±0.6	(13.2±2)
BCS	9.1±0.7	10.0±1	(10.7±9)
TNS	10.4±0.4	10.0±0.4	(11.0±7)

It shows that the fraction Φ_s determined from images acquired over a 5μm×5μm area instead of a 1μm×1μm area is more convincing with a smaller standard deviation. Large scale SEM images (8μm×10μm) of L-MLS and S-MLS used in these measurements are provided in Figure 4.5. The fraction Φ_s of L-MLS, S-MLS, BCS, and TNS was found to be 0.12, 0.14, 0.09, and 0.1. It follows that the values of static CAs calculated by Cassie theory are 158.5, 156.8, 161.4, and 160.4 °, which are comparable to the measured advancing angles shown in Table 4.2.

Table 4.2. Advancing angle θ_a, receding angle θ_r, CA hysteresis θ_h, normal adhesive force and force per unit length on MnO_2 superhydrophobic surfaces with different patterns

Patterns	θ_a （deg）	θ_r （deg）	$\Delta\theta_h$ （deg）	Adhesion (μN)	Adhesion/TCLlength (N/m)
L-MLS	165±1	88±1	77±1	(13±2)×10	$(6\pm1)\times10^{-2}$
S-MLS	165±1	128±1	37±1	(8±1) ×10	$(3.9\pm0.5)\times10^{-2}$
BCS	166±1	159±1	7±1	(4±1) ×10	$(2.3\pm0.7)\times10^{-2}$
TNS	165±1	163±1	2±1	0	0

L-MLS, S-MLS stand for MLS with large and small mesh scale, respectively.

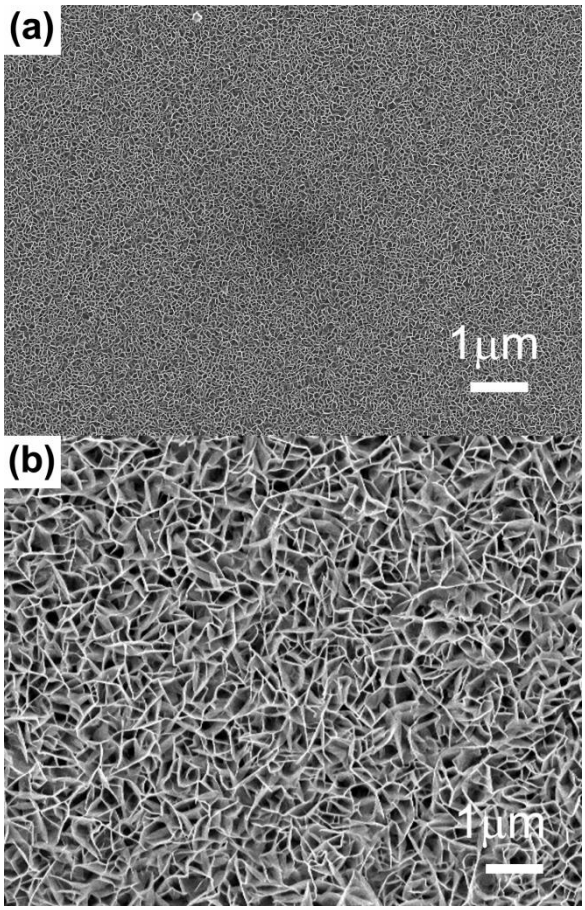

Figure 4.5 (a, b) SEM images of MnO_2 S-MLS and L-MLS films in large observation scale.

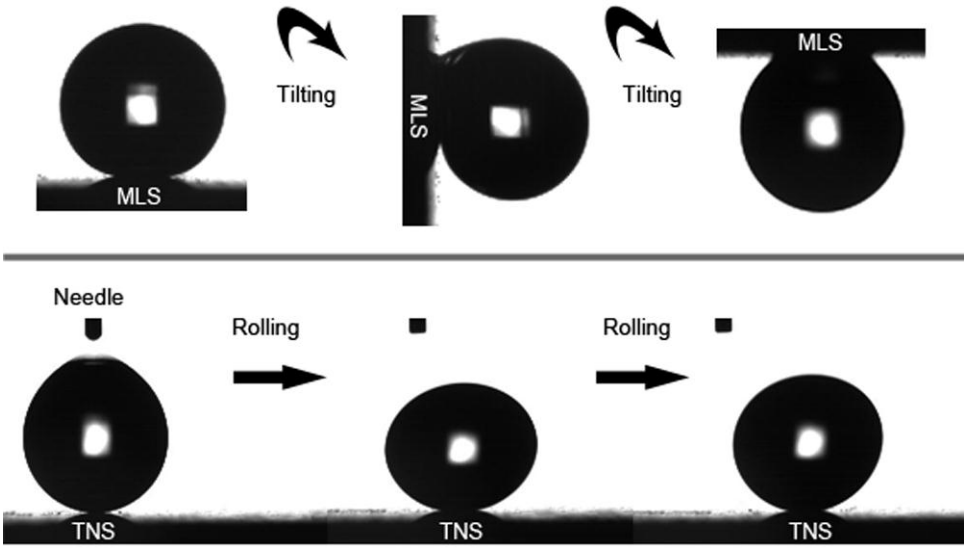

Figure 4.6 (a) Snapshots of water droplets sticking to the L-MLS film as it is turned vertically and upside down. (b) Snapshots of water droplet rolling on the TNS film.

However, a static CA cannot solely reflect the overall wetting properties of the surface. The different patterns of MnO_2 films were found to give rise to different adhesions. A water droplet was firmly pinned on the large MLS (L-MLS) film when the sample was placed in a vertical position or even on the film turned upside down (Figure 4.6(a)). In contrast, a water droplet can hardly stand on a leveled TNS film (tilting angle of less than 1 °, Figure 4.6(b)) and would immediately roll off[145] the surface once falling under gravitation. The adhesion of a water droplet on the surface of superhydrophobic MnO_2 film was characterized by CA hysteresis using a drag-to-move method.[116] The sessile water droplets were dragged to slide on the surface and the advancing angle (on the downhill side) and receding angle (on the uphill side) were measured. In this process, the volume of the water droplet (3 μL) and the distance between the

needle and the surface (1.76 ± 0.04 mm) were kept the same in all measurements (insets of Figure 4.3). As a complementary method, the adhesive force in the normal direction was directly measured by a highly sensitive microforce balance tensiometer.[117, 138] Table 4.2 summarizes the results of advancing and receding angles, the CA hysteresis, and the normal adhesive force. It demonstrates that the L-MLS MnO_2 film has the highest adhesive force $(13 \pm 2) \times 10$ μN among the films that we have synthesized so far, when 3μL water droplets were used in the measurements. In addition, films of this kind can fetch water droplets as large as 25 μL, which is 1.5 times larger than the reported 10 μL droplet.[134] This result suggests that the absolute value of the normal adhesive force is related to the length of TCL when the volume of the water droplets changes. Therefore, the normal adhesive force per unit length of TCL was calculated, as shown in Table 4.2. In the meantime, the film with a smaller mesh size (S-MLS, only 6% of the L-MLS's) exhibits a medium adhesive force (12% of the L-MLS's). Comparatively, nonadhesion (an adhesive force of nearly 0 μN) is observed for the TNS MnO_2 film. Furthermore, by combining the meshlike and rodlike characters together, the fabricated BCS film also possesses the medium adhesive force ($(4 \pm 1) \times 10$ μN).

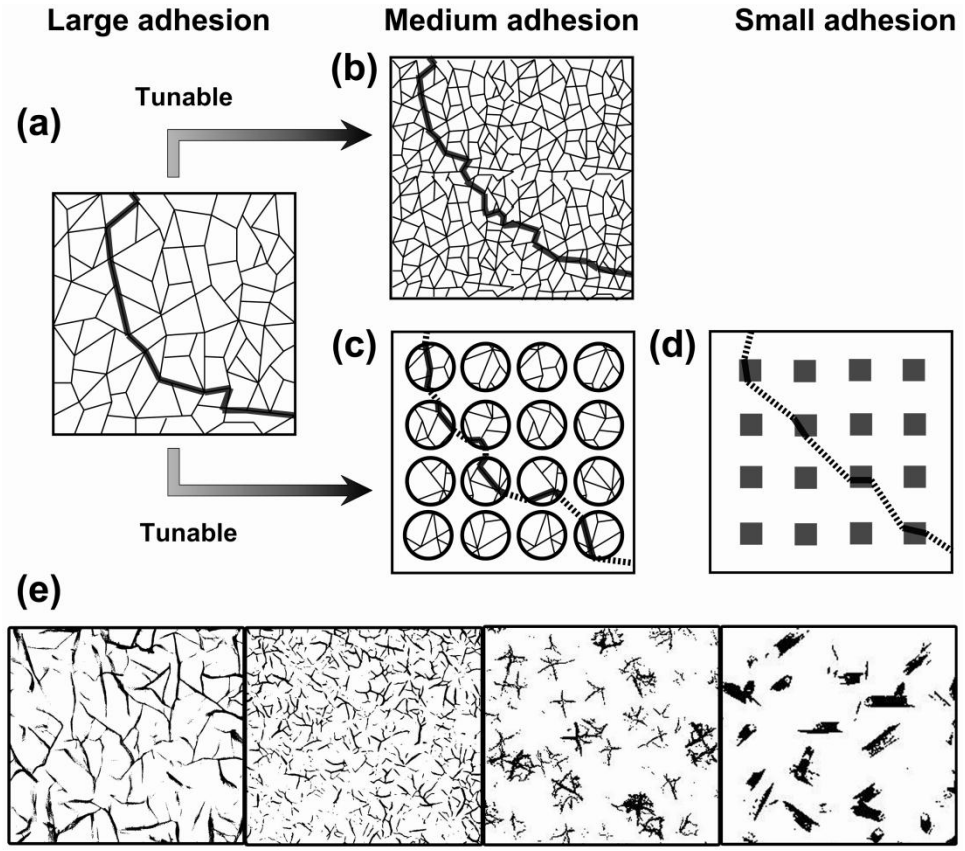

Figure 4.7 Schematic illustration of TCL on MnO_2 films. The solid lines demonstrate the possible solid-liquid-air interface contact line, and the dash lines demonstrate the liquid-air boundary for a droplet, respectively. (a) A continuous contact line forms on the L-MLS which exhibits large adhesion. (b) TCL on S-MLS. (c) Dash-line like TCL forms on BCS. (d) A highly discontinuous dot-like TCL forms on TNS, which exhibits extremely small adhesion. (e) High contrast black and white images converted from SEM images of L-MLS, S-MLS, BCS, and TNS, respectively.

Because all of the surfaces are made of MnO_2 and treated with the same molecule (PFOTES) in this study, the modulation of the adhesion of these films can be ascribed to the change in surface topography and patterns of MnO_2 films.

From a microscopic point of view, the adhesion of patterned films depends on the way of the solid-liquid contact modes (i.e., the TCL).[73, 75, 146, 147] The surface topography and patterns of MnO_2 films were simplified according to the high-contrast black-and-white SEM images shown in Figure 4.7. The solid lines describe the possible TCL for a droplet in contact with these patterns, showing different continuity.[83, 148] To be specific, Figure 4.7(a-d) illustrates two strategies for controlling the TCL continuity adopted to tune the adhesion. Figure 4.7(e) shows high-contrast black-and-white SEM images with different magnifications (cf Figure 4.4 for the actual dimensions) in order to make a comparison with patterned illustration in Figure 4.7(a-d). When a droplet is placed on most surfaces, it will come to rest at a local energy minimum. The contact line will be pinned at a metastable state, and there will be an energy barrier for any advancing or receding of the water droplet on the surface.[83, 149] This kinetic barrier difference in the advancing and receding modes gives rise to CA hysteresis, leading to the adhesive force. As for the MLS film, continuous linelike TCL is formed on the top of nanowall sheets as shown in Figure 4.7(a). Because of the large energy barrier between the two metastabe pinning states, the L-MLS film generates high CA hysteresis and thus a very high adhesive force. With decreasing mesh size, the energy barrier decreased as well. Consequently, the adhesive force is reduced as the mesh size shrinks (Figure 4.7(b)). Unlike the MLS structure, a highly discontinuous dotlike TCL forms on the TNS film (Figure 4.7(d)). Herein, the energy barrier between the metastabe pinning states is negligible. As a result,

the TNS film is nonadhesive, and water droplets will roll off effortlessly even the surface tilts slightly (Figure 4.6(b)). Furthermore, an intermediate state between these two distinct TCL modes can be obtained by mixing the patterns (linelike and dotlike TCL) (i.e. Figure 4.7(c)). On the hierarchical BCS film, the contact line is a combination of continuous linelike and discontinuous dotlike TCL, illustrated as a separated dash-line-like TCL. Correspondingly, a medium CA hysteresis and adhesive force are found on this pattern (Table 4.2).

4.4. Conclusions

Tuning the adhesion on the superhydrophobic surfaces of a given chemical material is accomplished in a real metal oxides system synthesized by an easy, cheap bottom-up approach. By changing the pattern of MnO_2 films from L-MLS to TNS, the acquired adhesive force varies from a very strong (132.4μN) to a nonadhesive force. Accordingly, two distinctive strategies of controlling the scale and distribution of the meshlike pattern to modulate the adhesion of superhydrophobic surfaces are proposed. The mechanism of adhesion on hydrophobic surfaces with special patterns is attributed to TCL continuity. Furthermore, the demonstrated kinetic control of the adhesion in our system can be extended to other low toxicity or nontoxic systems. We believe that the developed approach in tuning the adhesion of the superhydrophobic surfaces in a pattern-controlled manner will allow us to fabricate smart superhydrophobic surfaces, which will spin off various novel applications in materials science and engineering and bio/microengineering.

Chapter 5

Electrically Adjustable, Super Adhesion

We report a superhydrophobic membrane of MnO_2 nanotube arrays on which a water droplet can be immobilized by application of a small DC bias, despite of its large contact angle. For a 3 μL water droplet, the measured adhesive force increases monotonically with increasing negative voltage, reaching a maximum of 130 μN at 22 V, 25 times higher than the original value. It follows that the nearly spherical water droplet can be controllably pinned on the substrate, even if the substrate is turned upside down. Moreover, the electrically adjustable adhesion is strongly polarity-dependent; only a five-fold increase is found when a positive bias of 22 V is applied. This remarkable electrically controlled adhesive property is ascribed to the change of contact geometries between the water droplet and MnO_2 nanotube arrays, on which water droplets exhibit different continuities of

three-phase contact line (TCL). As the modulation in this manner is *in situ*, fast, efficient and environment-friendly, this kind of smart material with electrically adjustable adhesive property is expected to find various applications in biotechnology and in lab-on-chip devices.

5.1. Introduction

Recently, there has been growing interest in developing advanced micro/nanostructure surfaces with unique wetting properties for both fundamental research and practical applications.[129] Superhydrophobic surfaces with the contact angle (CA) larger than 150° and tilting angle smaller than 5° have received much attention due to a wide range of potential applications, including raindrop self-cleaning,[150] oil spill cleanup,[3] water-capture devices,[4] laboratory-on-a-chip devices,[5] bioinspired geckos/mussels feet[6] and functional interface for cell and tissue engineering.[7] The process for fabrication of a superhydrophobic surface via altering the surface energy and roughening of the surface has been well accepted.[32, 70, 71, 151, 152] Currently, one of the challenges in this area is to design and fabricate smart surface systems that are able to adjust the wetting properties on demand.[129, 153-155] For example, smart surfaces capable of reversible switching from a superhydrophobic to a superhydrophilic state in response to external stimuli, i.e., UV-light irradiation, electric field, temperature and pH, have been reported.[153-157] Of these,

electrowetting (EW) is a more promising technique to adjust the wetting and flow properties of water droplets due to its fast response, nonabrasive and easy application nature.[154, 158-162]

Wenzel's[70] and Cassie's[71] theories as well as the state transitions between them are commonly invoked to explain the micro-mechanism of wetting behavior on structured superhydrophobic surfaces. Wenzel introduced nondimentional surface roughness *r* to address the roughness enhanced superhydrophobicity. In his theory the measured contact angle is expressed as $\cos\theta = r\cos\theta_0$ (θ is the measured contact angle, θ_0 is the angle on a smooth surface and *r* is the ratio of the actual area of liquid-solid contact to the projected area on the horizontal plane.) Cassie, in turn, considered drops were supported by a composite surface composed of solid and air, where the air parts of the interface were considered as perfect non-wetting. In this case, the measured contact angle becomes $\cos\theta = \Phi_s(\cos\theta_0 + 1) - 1$, where Φ_s is the fraction of solid in contact with the liquid.

Even though conceptual problems may exist within Wenzel's and Cassie's theories, they still have merits to be applied at certain situations as advocated by their critics.[73-75] It is fairly straightforward to use them to characterize two distinguishable superhydrophobic states: the "slippy" Cassie state and the "sticky" Wenzel state. In general, water droplets adhere more strongly to the textured

surface in the Wenzel state than in the Cassie state, causing stronger contact angle hysteresis (the difference between advancing and receding angle). In many cases, water droplets on structured surfaces are in the metastable Cassie state and the transition from Cassie to Wenzel state can be induced by external stimuli, such as pressure, electric voltage, or vibration. Theoretically, Patankar[44] modeled the Cassie and Wenzel transition on a surface composed of regularly arranged posts. Ishino *et al*[91] (Quere) presented "phase diagrams" in the two-dimensional space of texture parameters. Following the same principle, Nosonovsky and Bhushan[93] derived an energy diagram for the Cassie and Wenzel states which were separated by energy barriers. Bartolo *et al*[99] pictured two scenarios for a transition occurrence according to how the meniscus contacted with the surface structure. One is for the meniscus directly contacting with the bottom of the surface and the other is for the meniscus sliding down into the structure of the surface. Therefore, developing novel nano/micro structures and investigating their wetting properties are very useful to clarify these theories and to apply them for new applications.

For many relevant applications such as microfluidic pumping systems, *in-situ* detection of analytes and lab-on-chip devices, it is desirable to develop a functional superhydrophobic surface with both a large CA and tunable adhesion. These applications also require such superhydrophobic surfaces with long durability, low fabrication costs and ease of mass production. Nevertheless,

significant challenges still remain, as the transition from a low to high adhesion state (e.g., hydrophilic state) is usually accompanied by a dramatic decrease in CA.[86, 159] Very recently, a series of superhydrophobic nanostructured surfaces with both a large CA and high adhesion have been obtained.[26, 48, 133-136, 139, 140] Among these studies, special attention has been focused on the superhydrophobic nanotube/nanopore structures because of the high adhesion that enables a water droplet to be firmly pinned on a surface without any movement, even when the substrate is turned upside down.[48, 140] Even though these studies have also led to a debate on the definition of superhydrophobicity and the microscopic mechanism for this remarkable pinning effect,[137, 163] they have indeed provided a practical and feasible route to an artificial Gecko-mimicking surface with both large CA and high adhesion. Unfortunately, despite the reports that these superhydrophobic surfaces have exhibited the ability to tailor water adhesion to some extent via control of the pore density, length and diameter of nanotubes as well as their contact geometries,[48, 140] the obtained adhesion is inherently determined by the fabrication process and cannot be adjusted once the surface is prepared. Therefore, these superhydrophobic surfaces may not be compatible with smart device applications, where the modulation must be *in situ*, fast and tunable.

The aim of this study is to identify a general and robust approach of producing smart superhydrophobic surfaces with both a large CA and electrically adjustable

adhesive force. In this regard, we will report the development of a novel superhydrophobic surface consisting of tilt-aligned conducting MnO_2 nanotube arrays (MTA) treated by stearic acid sodium. An electric-field is applied as an external stimulus to control the wetting behavior. The effect of the electric field on the adhesive force between water and the surface of the MTA membrane will be systematically examined. The findings obtained from this work will advance our understandings on the wettability of solid surfaces with special surface morphologies.

5.2. Results and Discussion

5.2.1. Microstructure of MnO2 nanotube arrays

The MTA membrane used in this study was prepared by the simple and low-cost hydrothermal treatment of a solution of $KMnO_4$ and HCl.[125] Figure 5.1(a) and (b) present typical SEM images of the as-prepared single-layer MTA membrane on a Si substrate, showing an inclined array of the MnO_2 nanotubes, with tilting angle of 74°± 8.6° between the tube axis and the plane of the substrate. (Figure 5.1(c)) The tilting angle of α-MnO_2 nanotubes might be formed during re-crystallization process from birnessite-type MnO_2 nanowalls[125, 126] and further investigation is required to reveal the mechanism. The open end and the square cross-section of the nanotubes can be clearly observed as shown in the

inset of Figure 5.1(b). The average length is 2μm and outer diameter and wall thickness are 103 nm and 23 nm, respectively. The density of the MAT membrane is about 2.38 tubes per μm^2. An optical image of the MTA membrane is shown in Figure 5.1(d). After surface modification, the MTA surface exhibits superhydrophobic wettability with very low water adhesion as water droplets roll off its surface easily. The small adhesion is different from the superhydrophobic polycrystalline TiO_2 nanotube arrays[140] and polystyrene (PS) nanotube arrays[48] which demonstrate large adhesion. This difference can be attributed to this inclined alignment of the MnO_2 nanotube arrays, of which the sharp protruding corners of the square nanotube ends are randomly distributed on the liquid-solid interface forming a discrete "point-contact" geometry. The discontinuous TCL is energetically favored by a hydrophobic surface with a lower adhesion, in contrast to the quasi-continuous "line-contact" TCL at the interface of TiO_2 nanotube arrays and water. In addition, the single-layer MTA membrane can be peeled off from the Si substrate by immersing the sample in hot water for 10 hours, and then transferred onto other substrates, i.e., flexible polypropylene (PE) and transparent glass etc. (Figure 5.1(e)), depending on the requirement of various potential applications.

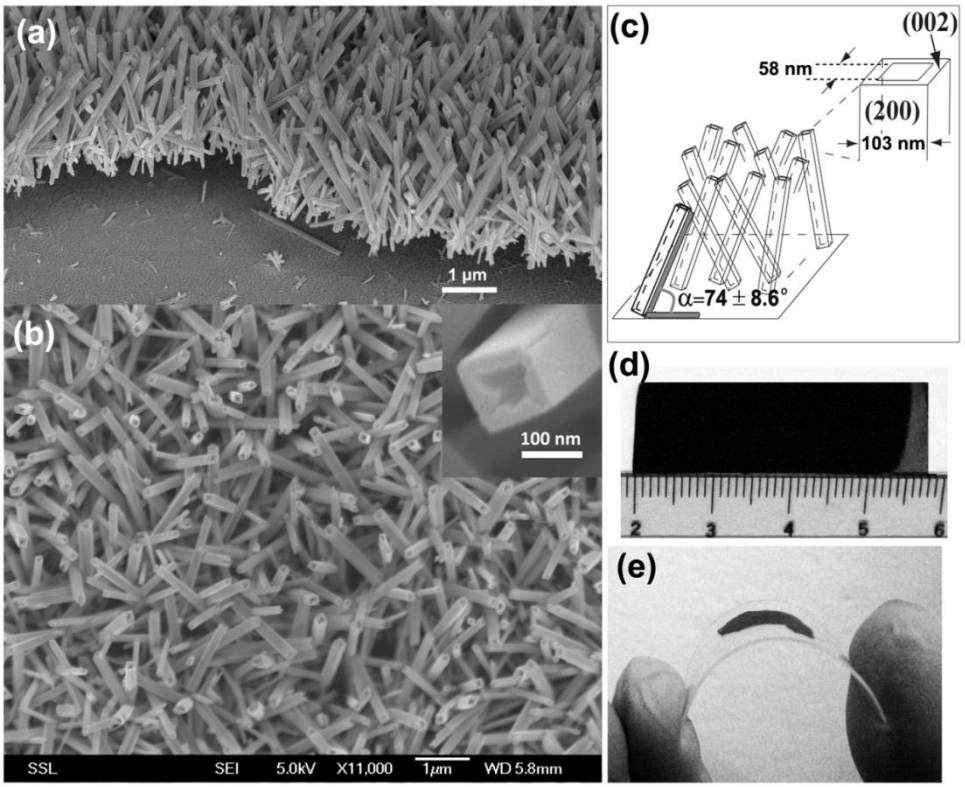

Figure 5.1 (a), (b) SEM images of α-MnO_2 nanotube membranes. The inset in (b) shows the typical tubular structure with a square open end. (c) Schematic illustration of an inclined alignment of MnO_2 nanotubes. (d), (e) Optical images of the MTA membrane on Si and flexible PE substrates, respectively.

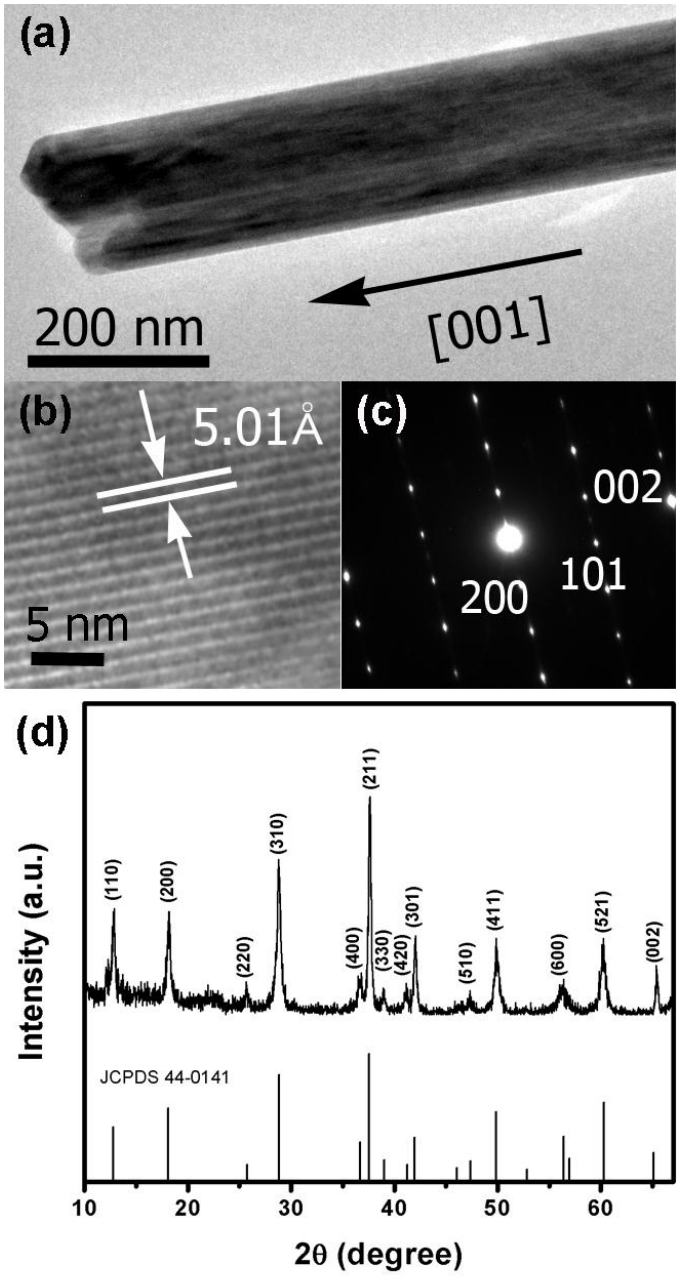

Figure 5.2 (a) TEM, (b) HRTEM and (c) SAED of the individual MnO_2 nanotube. (d) XRD patterns of MnO_2 nanotubes.

Transmission electron microscopy (TEM) analyses indicate that the obtained MnO_2 nanotubes are in a single-crystalline state and of a tetragonal Hollandite-type structure (Figure 5.2(a)-(c)). The selected area electron diffraction (SAED) pattern and high-resolution transmission electron microscopy (HRTEM) analysis reveal that the tube axis is in the [001] direction (c axis), and the lateral faces of the nanotubes are bounded by the stable low-energy {200} facets. The phase purity and crystal structure of the MnO_2 nanotubes have been characterized by X-ray diffraction (XRD). As shown in Figure 5.2(d), all the diffraction peaks can be exclusively indexed as the tetragonal MnO_2 (JCPDS 44-0141), and no other impurities are observed. The MnO_2 nanotubes have a band gap of ~1.03 eV and a low electrical resistivity (pressed pellet) of ~ 0.035 $\Omega \cdot$ cm at room temperature determined by the optical absorption spectrum and the four-point probe method, respectively.

5.2.2. Electrowetting and adhesive properties of MnO_2 nanotube membrane

In this work, the phenomenon of electrically adjustable adhesion in the superhydrophobic MTA membrane was initially observed in an advancing/receding angle measurement after application of a controlled DC

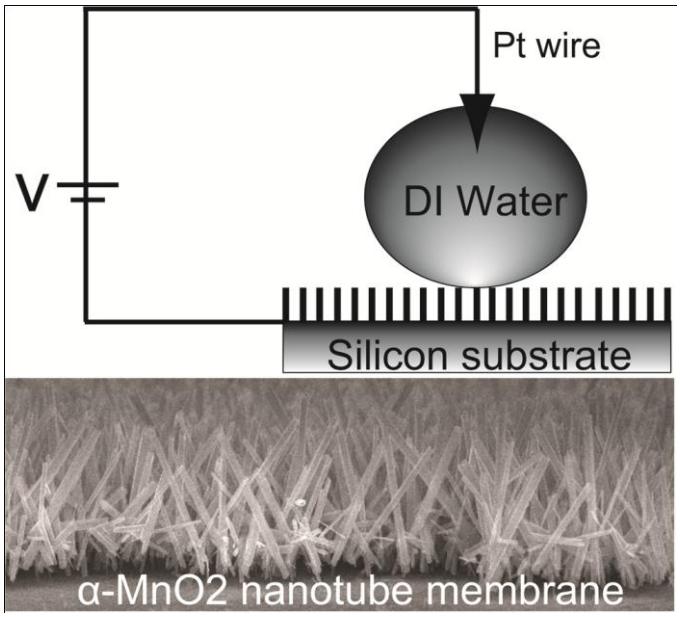

Figure 5.3 Scheme of the experimental setup for the EW test. A Pt wire probe is inserted into the droplet to establish electrical contact.

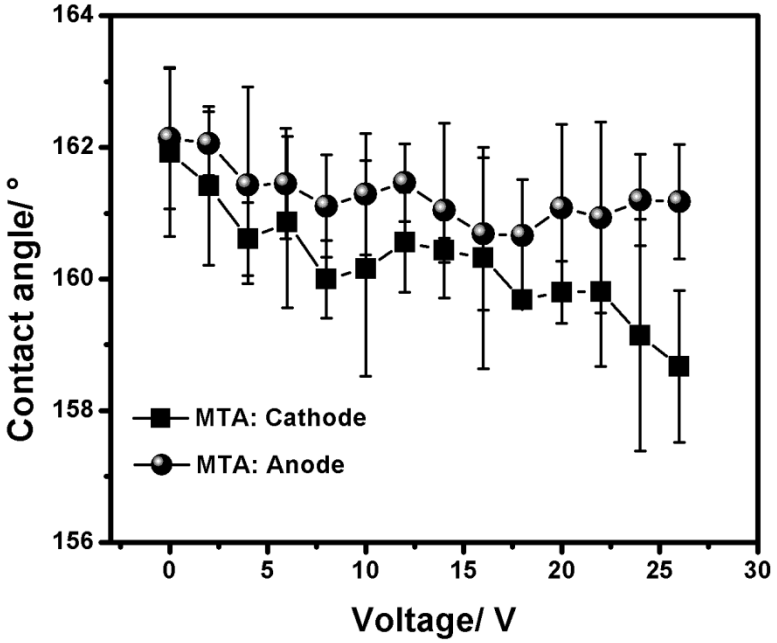

Figure 5.4 Apparent contact angle variation of a deionized water droplet for different positive/negative bias voltages.

bias. To establish electrical contact, a Pt wire was inserted into a water droplet as shown in Figure 5.3. The bias was applied for 5s and the behavior of the water droplet was measured after removing the bias. All experiments were carried out using a 3 μL deionized water droplet in an ambient environment with a relative humidity of around 60%. Figure 5.4 shows the CA of the water droplet on the superhydrophobic MTA membrane as a function of positive and negative bias voltage. As seen in Figure 5.4, the CA remained apparently unchanged with increasing voltage when a positive bias was applied to the MTA membrane (MTA membrane as an anode). However, when the negative bias was applied to the MTA membrane (MTA membrane as a cathode), the CA was found to decrease slightly from 162° to 157° as the bias voltage increased. The droplet displays an intangible sinking into the membrane with the reduced CA. The observation of polarity-dependent EW property can be attributed to possible weak electrolysis occurring at the liquid-solid interface, where a very small amount of MnO_2 is reduced. This is similar to the change in CA observed in EW measurements of aligned carbon nanotube arrays.[161, 162] Moreover, it is surprising to see a dramatic change in the CA hysteresis angle in contrast to the small decrease in CA. As shown in Figure 5.5, a large receding angle (~159.64°) and a small hysteresis angle (~5.25°) were observed without bias, consistent with the superhydrophobic Cassie state.

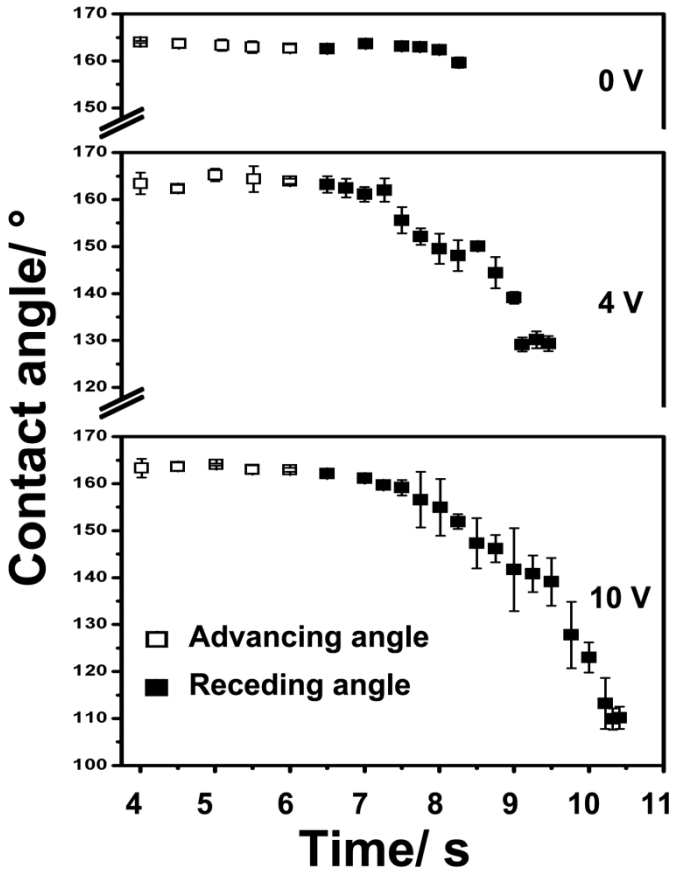

Figure 5.5 Advancing/receding angle measurements of a water droplet for the negative bias of 0, 4 and 10 V respectively.

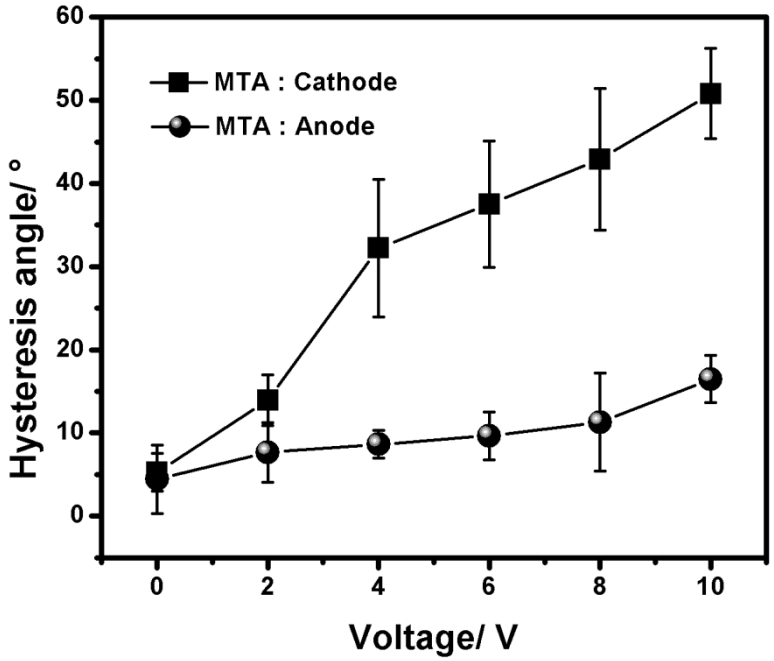

Figure 5.6 Hysteresis angles as a function of positive/negative bias voltage.

When a voltage of 4 V was applied, the advancing angle remained as high as 160°, but the receding angle was drastically reduced to 129.14°. As the bias increased to 10 V, the receding angle dropped to 110.2° and the hysteresis angle increased to 50.8°. Figure 5.6 plots the hysteresis angle as a function of bias voltage. The hysteresis angle increased as the voltage increased when the MTA was adopted as a cathode, while only a slight increase was observed when MTA was adopted as an anode. This result is quite different from the previous work in which hydrophobic surfaces with a high CA hysteresis usually have a CA smaller than 150 °, but is similar to the observations from the superhydrophobic nanotube/nanopore surface.[48, 140] More significantly, these results indicate that the adhesion between the water droplet and the MTA membrane can be modulated by applying a small bias voltage without losing large CA.

We have calculated the adhesive force according to the shape deformation of a water droplet just before detachment from a substrate.[165] Figure 5a shows a schematic illustration of the deformation of a water droplet. The vertical force balance of the water droplet is considered for simplicity.

$$F_{\gamma} - \Delta P \cdot S - G - f = 0 \qquad (5\text{-}1)$$

where f is the adhesive force between the MTA membrane and the water droplet, G is the gravity of the lower part of water droplet illustrated/indicated by the black bold line, F_{γ} denotes the surface tension force obtained from

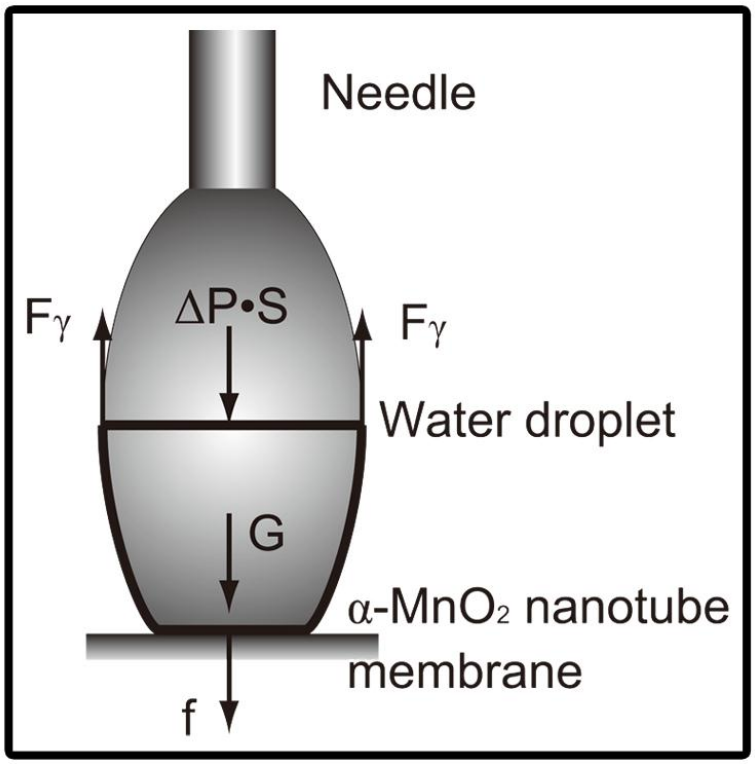

Figure 5.7 Sketch of the shape deformation for a stretched water droplet. For simplicity, the force balance along the vertical direction for the lower part of water droplet(indicated by the black bold line) was considered. F_γ and f are the surface tension force and the adhesive force, respectively. G is the gravitational force experienced by the lower part of the water droplet, and ΔP is the pressure difference between water and air.

$F_\gamma = 2\pi R_X \cdot \gamma$ (R_x: radius of water droplet; γ surface tension of water) and ΔP is the pressure difference between the liquid and vapor phases, which can be calculated by the curvature of its interface. Combining this relation with the Laplace equation,

$$\Delta P = \gamma\left(\frac{1}{R_x} + \frac{1}{R_y}\right) \tag{5-2}$$

yields the following equation:

$$f = \pi R_X \gamma\left(1 - \frac{R_x}{R_y}\right) - \rho V g \tag{5-3}$$

where R_x and R_y denote the principal radii of curvature.

The adhesive force between the water droplet and the MTA membrane is estimated based on this model and plotted in Figure 5.8. The insets of Figure 5.8 show snapshots of the water droplet just before detachment from the substrate under different biases. As seen in Figure 5.8, a small increase in adhesive force was observed up to 22 μN at 10 V when a positive bias was applied, while the adhesive force changed dramatically from 5.2 to 100 μN when a negative bias was applied, indicating the polarity-dependent nature of this adhesive property. The increasing adhesive force is also consistent with the trend of the hysteresis angle shown in Figure 5.6. As the water adhesion reached about 100 μN under 10V, which can firmly pin the water droplet onto the surface, thus the droplet would break away from the needle at voltages larger than 10 V.

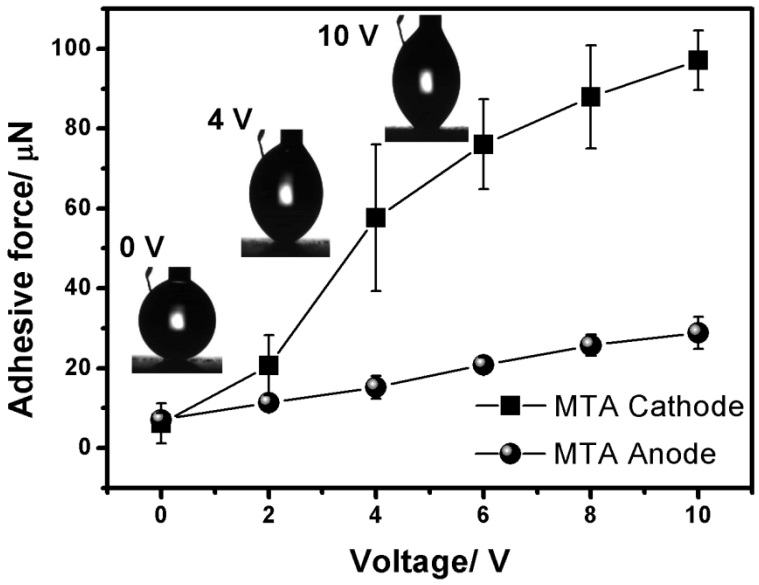

Figure 5.8 The adhesive force calculated as a function of applied voltage. The insets are snapshots of water droplets just before detachment from superhydrophobic MTA membranes.

To further examine the electric-field-dependent adhesive property at a negative bias voltage larger than 10 V, direct force measurements were conducted using the processor tensiometer system (inset of Figure 5.9). Figure 5.9 displays a typical force-distance curve for the force measurement. After the water droplet was pinned on the MTA membrane under certain voltage, it was first brought into contact with the grid. Then the MTA membrane was moved away from the grid at a rate of 0.02 mm s^{-1}, and the measured force increased gradually, reaching a maximum just before the detachment of the water droplet. Subsequently, the measured force decreased rapidly as the water droplet broke away from MTA

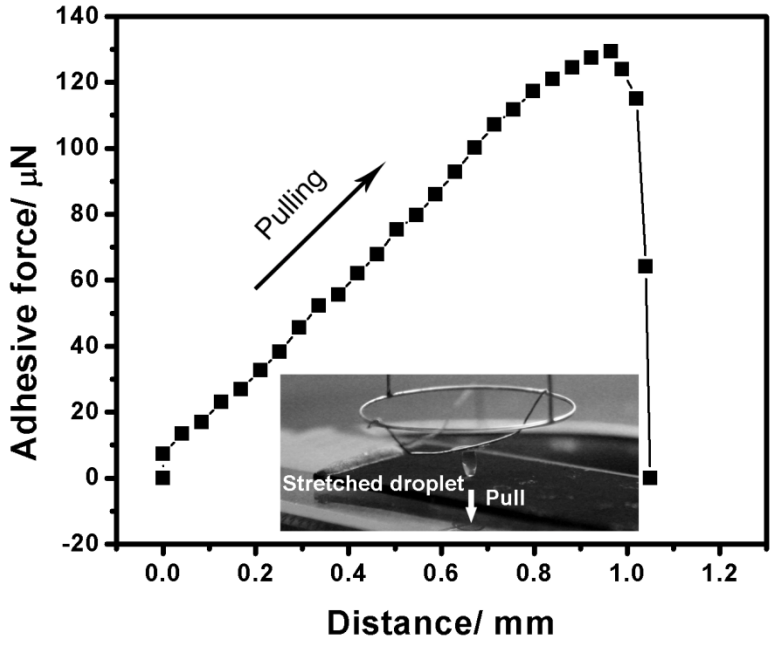

Figure 5.9 Force-distance curve as a water droplet is stretched and pulled off the substrate. The inset is an optical image of the stretched droplet.

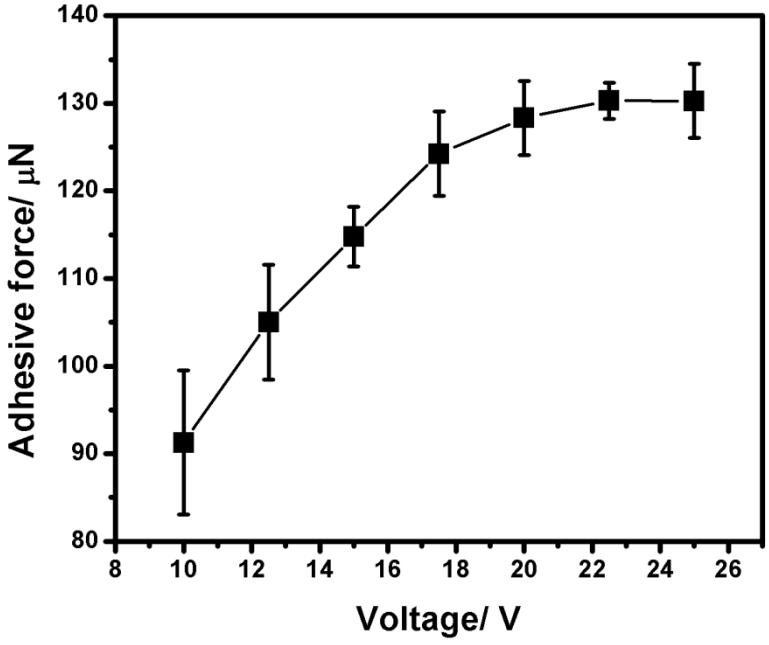

Figure 5.10 The adhesive force as a function of applied negative voltage obtained by direct force measurement.

membrane. The voltage-dependent adhesive force measured by the balance system is shown in Figure 5.10. At voltages below 22 V, the measured adhesive force increased monotonically with increasing bias voltage. The maximum force was about 130 μN at 22 V. When the voltage was higher than 22 V, the maximum force remained but the water droplet broke into two parts. This phenomenon indicates that the maximum adhesive force surpasses the maximum water surface tension under this measurement. As calculated, the maximum surface tension was about 137 μN for a 3 μL water droplet with a CA of 160° at room temperature when it was pulled vertically. Such a superhigh adhesive force has never been observed with a CA larger than 150° in other superhydrophobic surfaces. The magnitude of the adhesive force is about two or three times higher than that reported for superhydrophobic PS and TiO_2 nanotube arrays. Therefore, the water droplet can be controllably immobilized by application of the electric field on the substrate without any movement, even if the substrate is turned upside down.

5.2.3. Modulation Mechanism of Adhesive Force

According to previous results,[26, 48, 133-136, 139, 140] the adhesive behavior of a water droplet on a superhydrophobic surface is mainly determined by the van der Waals' force, contact geometry, and capillary interaction. One possible mechanism explaining the electrically adjustable adhesive force of the superhydrophobic MTA membrane is illustrated in Figure 5.11, and is mainly attributed to the promoted continuity of TCL and multi-metastable states. As shown in left side of Figure 5.11, without the bias voltage, a droplet sitting on the MTA membrane shows a superhydrophobic Cassie state with large CA and low adhesion. The lower depiction describes corners of MnO_2 posts supporting a sessile water droplet. The liquid-solid contact geometry in this condition is a discrete "point contact". The black line describes the possible TCL for a water droplet in contact with this surface. In this geometry, the contact line cannot make continuous contact with the surface. And there is little or no difference in energy between different states during advancing and receding, thus no stable meta-stable states.[83] In this case, it will move spontaneously on the surface by small incremental advances or recessions without contact angle hysteresis. When a negative bias is applied, the CA reduces accompanied by the increase of adhesion showed in right side of Figure 5.11. In the meantime, water impales into the surface structure, and this penetration leads to a change of contact geometry from a discontinuous "point contact" to a quasi-continuous "line contact" TCL. In microscopic view, the contact line deviates from a circular shape to the one with

maximum contact with the sides of nanotubes and minimum contact with airy area due to minimum total free energy. Therefore the TCL has to overcome certain energy barrier before advancing or receding. Apparent difference between advancing and receding contact angle leads to large hysteresis and this large hysteresis explains why such a surface can possess super-high adhesion.

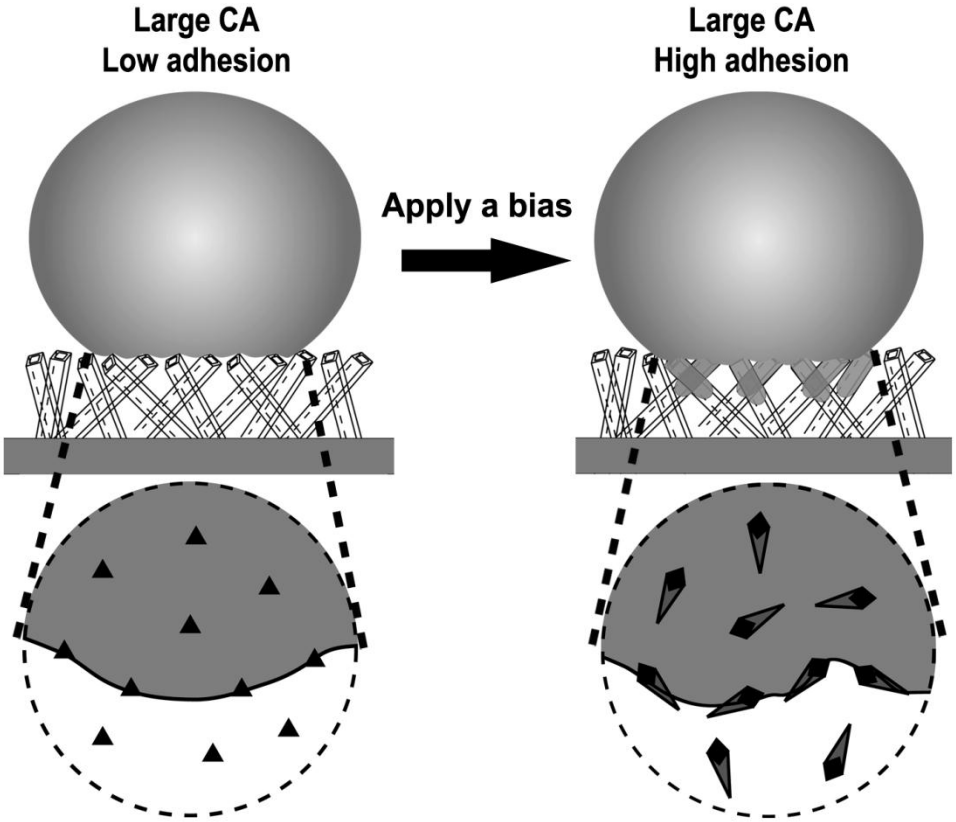

Figure 5.11 Schematic illustration of the transition of a water droplet behavior induced by the electric field. The lower part displays different contact geometries and possible TCL with and without bias, respectively.

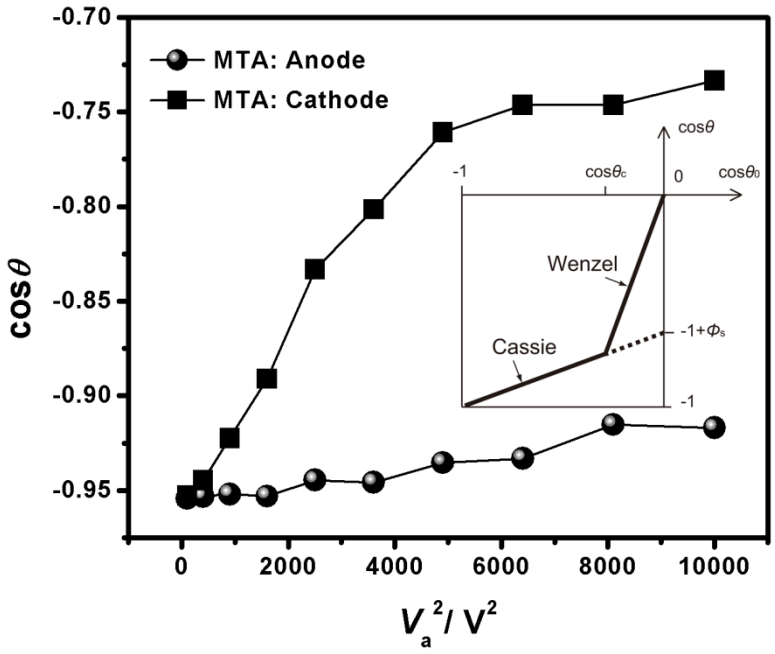

Figure 5.12 Plots of $\cos\theta_v$ as a function of the squared applied potential V_a^2 for deionized water under different electrodes. The inset shows plots of the Cassie and Wenzel angles as a function of the contact angle on smooth surfaces.

Another feature is that there is no sharp transition observed from Cassie to Wenzel state in our experiments. Theoretically Wenzel state should be favored if CA is smaller than the critical CA θ_c ($\cos\theta_c = (\Phi_s - 1)/(r - \Phi_s)$, where Φ_s and r are defined in Cassie's and Wenzel's theories above) based on minimum interfacial energy concern. Therefore Cassie-Wenzel state transition will occur as CA gradually decreases as shown in inset of Figure 5.12.[86] The plot of $\cos\theta_v$ as a function of the squared applied potential V_a^2 for deionized water under different electrodes is presented in Figure 5.12, where θ_v is the contact angle with the applied potential V_a based on the Lippamnn equation $\cos\theta_V = \cos\theta_0 + \frac{C}{2\gamma_L} V_A^2$

.[161, 166, 167] As seen in Figure 5.12, $\cos\theta_v$ gradually increased as the applied bias increased and saturated at higher voltage. This result is different from the observations in vertical arrays of silicon nanopost[168] and carbon nanotube[166], where a clear Cassie-Wenzel transition point is found. This phenomenon can be ascribed to the successive transition of multi-metastable states induced by the special contact geometry of the inclined arrays of MnO_2 nanotubes.

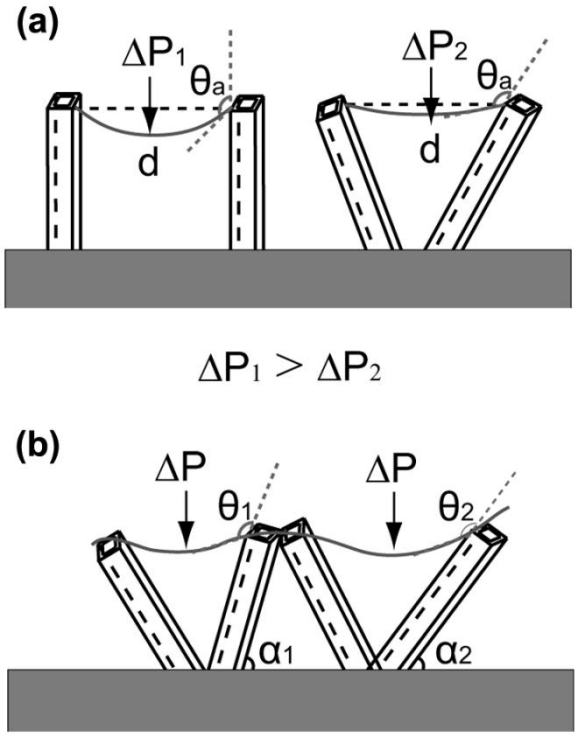

Figure 5.13 Sketch of (a) different requirements of Laplace pressure for TCL to reach the "local advancing angle" on vertical posts and inclined ones. (b) Local contact angles are different depending on different tilting angles of posts under certain Laplace pressure.

Theoretically, Bartolo *et al*.[99] modeled the critical Cassie and Wenzel transition in "touching" and "sliding" scenario based on the vertical aligned pillars. The "local advancing angle" was defined in "sliding" scenario to characterize the critical point beyond which the TCL would spontaneously slide downwards along the pillars. We extend this concept to inclined posts as shown in Figure 5.13(a) and (b); Larger Laplace pressure is required for TCL to reach the "local advancing angle" on the vertical posts compared with inclined ones, because the mean curvature in the former case is larger (Figure 5.13(a)), where ΔP is the Laplace pressure, θ_a is the "local advancing angle" and d is the spacing distance. Therefore on inclined MnO_2 nanotubes, the local angles vary from each other depending on different tilting angles of posts at a constant Laplace pressure shown in Figure 5.13(b), where θ_1 and θ_2 are different local contact angles and α_1 and α_2 are different tilting angles of posts. With gradual increase of Laplace pressure, the TCL will continuously increase by partially sliding down only at some locations where local angles exceed the "local advancing angle". And this is the reason why we can continuously adjust the adhesion to certain extent.

In addition, the packed MnO_2 nanotubes sealed by water emerge at the solid-liquid interface with slight decrease in CA as shown in right side of Figure 5.11. In the meantime, increased contact area produces more packed MnO_2 nanotubes. The trapped air in MnO_2 may also contribute to the superhigh adhesion in the form of capillary attraction because of the negative pressure induced by the

increase in the volume of an air pocket when the droplet is pulled away from the surface.[138] Therefore, another experiment was carried out to compare the negative bias-dependent adhesive property of aligned MnO_2 nanorod array (MRA) with the results obtained from the MTA. The SEM image of MRA is shown in Figure 5.14. Figure 5.15 summarizes the adhesive force measured by CA for the MTA and MRA membranes. The enhanced adhesive force with elevated voltage was also observed on the MRA membrane but was lower than that on the MTA membrane. Assuming that the extra contact area arising from the inner wall of the nanotube is negligible, the enhanced adhesive force for the MTA membrane (in contrast to the MRA membrane) can be attributed to the contribution of capillary attraction induced by negative pressure.

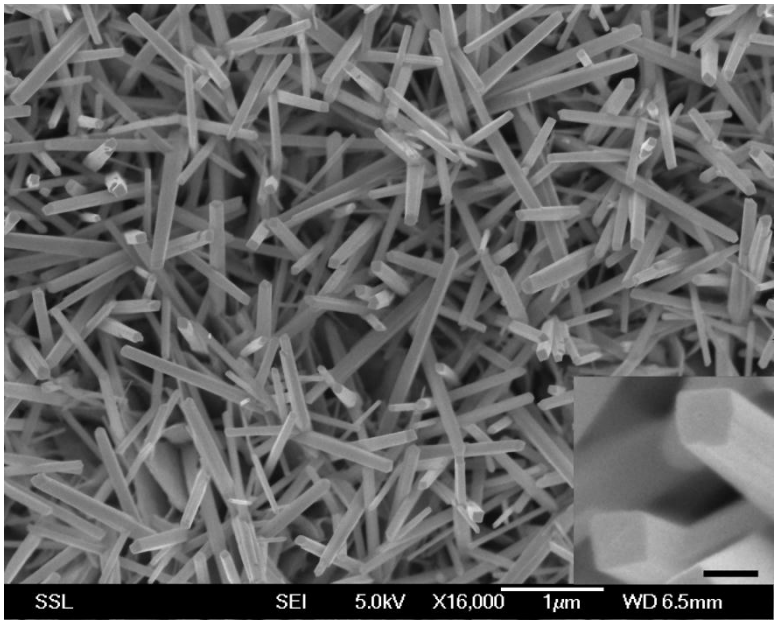

Figure 5.14 SEM images of MnO_2 nanorod membranes.

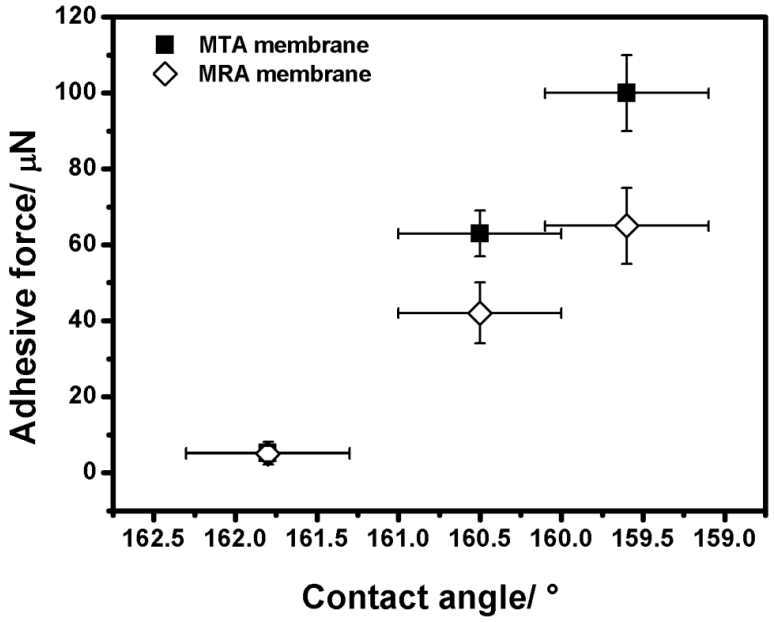

Figure 5.15 Comparison of the adhesive properties of the MTA and MRA membranes as measured by CA.

5.2.4. Electrically controlled transfer of water droplets

The superhydrophobicity of the MTA substrate as well as the high adhesion between substrates and water droplets also retain after the removal of bias, as shown in Figure 5.16(a). The adhesive force between the water droplet and the MTA membrane can be kept at a fixed value for a long time even when the bias is removed and then elevated again on demand by increasing the applied voltage. Furthermore, this substrate is robust and reusable within a working voltage ranging from 0 to 25 V to electrically control the adhesive forces. The superhydrophobic MTA membrane can maintain its function for at least three months when stored at 4 °C. All of these features of the superhydrophobic MTA

membrane will enable many practical applications related to controllable manipulation and immobilization of water droplets.

To demonstrate the advantages of the superhydrophobic MTA membrane, this membrane was used as "smart mechanical hand" to continuously transport a small water droplet from one MTA membrane to another by controlling electrode polarity and magnitude of the applied voltage. As shown in Figure 5.16(b), a water droplet was first placed on an MTA membrane (M1) with no voltage applied. Next, another MTA membrane (M2), adopted as a cathode, was slowly moved towards M1 to make contact and adhere the water droplet by application of 5 V voltage, as shown in the left side of Figure 5.16(b). Then, M2 was moved away from M1 and the water droplet was completely transferred from M1 to M2. Following the same procedure, this water droplet can be transferred back to M1 by switching the electrode polarity and applying a 15 V voltage. The final CA of the water droplet was still higher than 150 ^{o}. This water transport process has been repeated more than 30 times in one day using the same MTA membranes, indicating good durability of the MTA membrane.

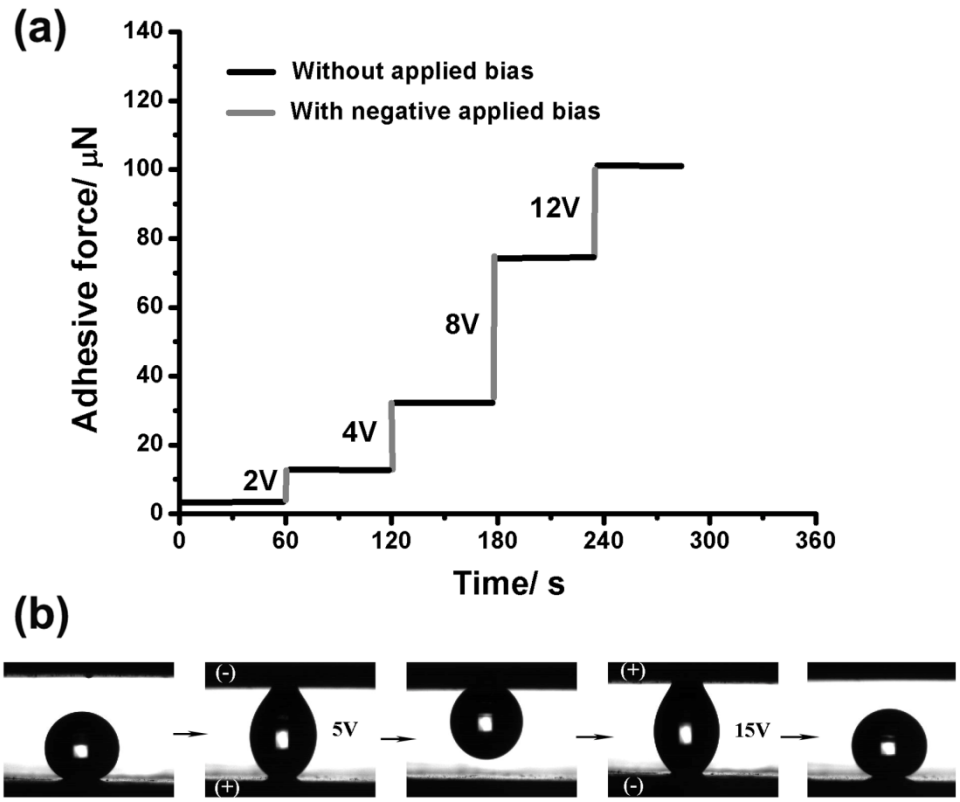

Figure 5.16 (a) Successive adjustment of the adhesive force on a water droplet by control of the bias voltage. (b) Controllable pinning and transport of a nearly spherical water droplet between two superhydrophobic MTA membranes.

5.3. Conclusion

In summary, the present study reports a novel superhydrophobic MTA membrane with both large CA and an electrically adjustable super adhesive force. This adhesive force can be continuously modulated in a wide range so that a nearly spherical water droplet can be flexibly transferred from one MTA substrate to another on demand. Typically, for a 3 μL water droplet, the measured adhesive force increases monotonically with increasing negative voltage, reaching a maximum of 130 μN at 22 V which is 25 times higher than the original value. The adhesive force is strongly dependent on polarity, and only a five-fold increase has been found when a positive bias of 22 V is applied. Continuity of TCL and multi-metastable states are invoked to explain the macro mechanism of electrical adjustment of adhesive force on MTA membrane. The modulation of adhesive force in this manner is *in situ*, fast, and repeatable. This fast and repeatable adjustment of adhesive force in a wide range without losing its large CA reported here is a key step towards the design and fabrication of novel interfacial materials and smart devices for future applications. Therefore, this kind of smart MTA membrane with remarkable adhesive properties is expected to find a wide variety of applications in biotechnology, lab-on-chip devices and microfluidic plumbing systems.

Chapter 6

Conclusions

Superhydrophobic materials attract extensive attention from both scientific and engineering field due to their water-repellent and self-cleaning properties. Beyond these studies, abnormal superhydrophobic surfaces with both large CA and large adhesion open a new realm of wettability investigation. Despite the argument of definition on superhydrophobicity, these superhydrophobic-like materials find their potential applications in localized chemical reactions, biochemical separation, bio/chem analysis assay, and single-molecule spectroscopy. One of the main obstacles which inhibit the further development in micro-fluidic system and lab-on-chip devices is the challenge to control the liquid adhesion on these special superhydrophobic surfaces. Hence, the ultimate goals of my research project are to reveal the intrinsic correlation between the structural features and the adhesion

on superhydrophobic surfaces and to further identify a new technique to control the adhesion in a fast and *in-situ* manner. Several closely relevant topics, as discussed in respective chapters, uncover a facet of the patterned-adhesion on superhydrophobic surfaces and possible techniques to modulate the adhesive force on superhydrophobic surfaces. Besides, some feasible orientations of the adhesion study on superhydrophobic surfaces where further dedication of endeavor is worthwhile will be pointed out in this chapter, including their potential and currently encountered difficulties and applications.

6.1. Conclusive Remarks

The investigation from the synthesis of MnO_2 superhydrophobic surfaces to their robust and adhesive properties was discussed from Chapter 2 to Chapter 5.

In Chapter 2, the reason why we chose MnO_2 as a good candidate for superhydrophobic study is explained. A cheap and robust hydrothermal approach of fabricating MnO_2 membrane is introduced and this method is further developed in Chapter 3 to finely control the topographic structures of MnO_2 membrane. The formation mechanism of MnO_2 nanotubes is investigated based on time evolution of the morphology. The two typical growth stages selected from the different reaction time reveal clearly that the nanotube is formed by chemically etching the solid nanorod. In addition, some important experimental techniques including

FT-IR, contact angle and normal adhesive force measure were introduced. The contact angle analyzer was conducted to get advancing/ receding angles and to record dynamic wetting process which were valuable information for wettability investigation. Since the measurement of CA hysteresis only indicates effects of adhesion along the shear direction, the normal adhesive force was performed to make a complementary study.

Chapter 3 reported the synthesis of robust superhydrophobic surfaces based on MnO_2 films with various morphologies. Theoretically, the hierarchical structures reduce the contact angle hysteresis by lowering the transition state energy between metastable states from the kinetics perspective; from thermodynamic perspective, the increasing of the Laplace pressure makes water droplet harder to penetrate into the structures, indicating the robustness of superhydrophobic surfaces.[10] Therefore, the hierarchical MnO_2 nanopropeller array (NPA) was designed and fabricated by a two-step hydrothermal method. The formation mechanism of the α-MnO_2 NPA was revealed by investigating on time dependent evolution of the morphology. The robustness of superhydrophobicity was confirmed by the water droplet squeezing test. The results showed that the NPA film maintained its superhydrophobicity under the pressure of 500 Pa, which was sufficient to address bouncing droplets and/or vibrating droplets in superhydrophobic state. This facile route of fabricating superhydrophobic MnO_2 film with hierarchical nanostructures is expected to be applied in micro/nanofluidics system and lab-on-chip devices.

Since we have successfully fabricated MnO_2 membrane with different topographic morphologies, it is important to correlate the topographic patterns with the adhesive property. And this issue was addressed in Chapter 4. Meshlike structure (MLS), ball cactus-like structure (BCS), and a tilted nanorod structure (TNS) were synthesized on the basis of the hydrothermal method. By changing the pattern of MnO_2 films from L-MLS to TNS the acquired adhesive force varies from a very strong (132.4μN) to a nonadhesive force. Since all of the surfaces are made of MnO_2 and treated with the same molecule (PFOTES) in this study, the modulation of the adhesion of these films was ascribed to the change of TCL continuity. Accordingly, two distinctive strategies of controlling the scale and distribution of the meshlike pattern to modulate the adhesion of superhydrophobic surfaces are proposed. This patterned-dependent adhesive investigation has universal value indicating that the demonstrated kinetic control of the adhesion in our system can be extended to other low toxicity or nontoxic system.

It is our aim to further fabricate smart surfaces which is able to respond to external stimuli. Therefore, we turned to utilize the electric field to control the adhesive force on the superhydrophobic MnO_2 membrane in a fast and *in-situ* manner. In Chapter 5, we reported the superhydrophobic membrane of MnO_2 nanotube arrays on which a water droplet was immobilized by application of a small DC bias, keeping the large contact angle. Typically, for a 3 μL water

droplet, the measured adhesive force increased monotonically with increasing negative voltage, reaching a maximum of 130 μN at 22 V which is 25 times higher than the original value. This result demonstrates that the adhesive force can be continuously modulated in a wide range by a small electrical bias.

Continuity of TCL and multi-metastable states are invoked to explain the macro mechanism of electrical adjustment of adhesive force on MTA membrane. The interpretation is consistent with the mechanism of pattern-dependent adhesive property on the MnO_2 membrane with varied topographic structures. This fast and repeatable adjustment of adhesive force in a wide range without losing its large CA is a key step towards the design and fabrication of novel interfacial materials and smart devices for future applications. Therefore, this kind of smart MTA membrane with remarkable adhesive properties is expected to find a wide variety of applications in biotechnology, lab-on-chip devices and microfluidic plumbing systems.

6.2. Outlook to Future Research Perspective

Further studies based on the results and the techniques developed in my research works which are worthwhile to undertake are suggested in the following directions.

First, the one-step hydrothermal method used in our research can shed light on developing other facile approaches to fabricate more membranes with different topographic morphologies in large scale and good homogeneity, suitable for industrial scale production.

In addition, the two proposed strategies of controlling the scale and distribution of the meshlike pattern to modulate the adhesion on superhydrophobic surfaces discussed in Chapter 4 can be extended from oxide system to other low toxic or nontoxic systems in bio/ microengineering.

Besides, although the TCL dependent adhesion was investigated in the study of pattern related adhesive force and the superhydrophobic state transition on MnO_2 membrane, its origin is still not fully understood. There is a need to establish the quantitative relationship between the TCL and the adhesive property of the superhydrophobic surfaces.

Last but not least, the electrical modulation of adhesion on superhydrophobic surfaces discussed in Chapter 5 may provide interesting functional materials in the field of stimuli-responsive surfaces. Based on this technique of tuning the water adhesion in a fast and *in-situ* manner, more potential applications can be anticipated apart from the application of transferring water drops which is demonstrated in Chapter 5. One of the prospective applications is the optimization

of the air-retaining feature, which contributes in the fluidic drag reduction. The application of electric bias which increases the water adhesion of the membrane suggests a good way to enhance the stability of the air-retaining features, as shown in the schematic illustration in Figure 6.1.

As shown in the upper part of Figure 6.1, when the MnO_2 nanotube membrane is immersed in water, a thin layer of air would be sealed within the nanostructured surface. However, the as-formed air layer is not stable, depending on the depth and the mobility of the water.[169] As the electric bias applied, shown in the lower part of Figure 6.1, the water adhesion on the MnO_2 nanotube membrane increases simultaneously due to the change of contact geometry discussed in Chapter 5. In the meantime, some water would inevitably penetrate into the nanostructure of the membrane. The trapped air in MnO_2 nanotube may also contribute to the increased adhesion in the form of capillary attraction because of the negative pressure induced by the increase in the volume of an air pocket when the water is pulled away from the surface.[138] Therefore, a more stable air layer is expected to be confined on the superhydrophobic surfaces.

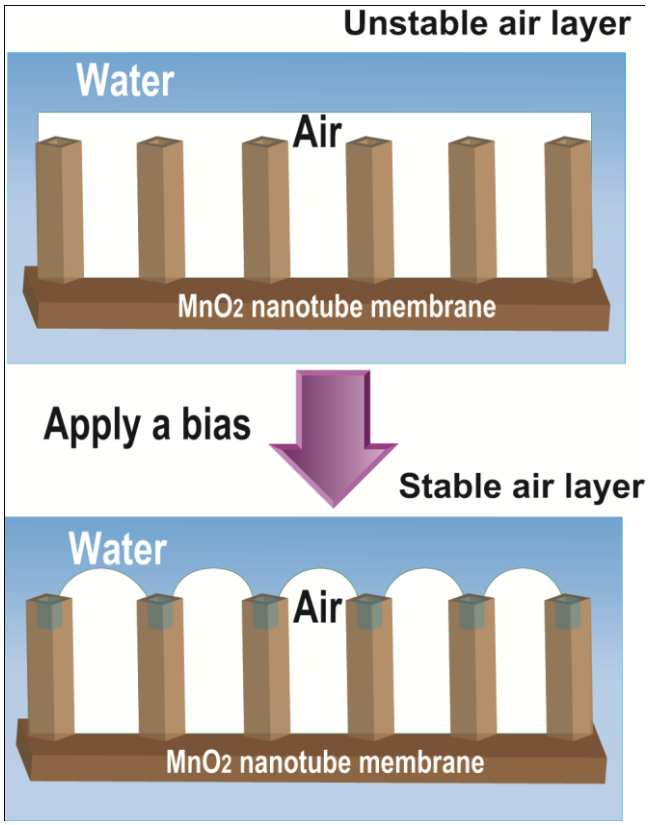

Figure 6.1 Scheme of stabilizing air layer under water on superhydrophobic MnO_2 nanotube membrane by electric bias.

In summary, the study of superhydrophobic surfaces originates from mimicking nature, but it can be also extended to create new functional materials beyond those found in nature. Therefore, it is a multidisciplinary field interfacing with surface chemistry, physics, nanomaterials, biosurface, mechanics, where researchers can make full use of their imagination.

References

1. Gao, L.; McCarthy, T. J., A Commercially Available Perfectly Hydrophobic Material (θA/θR = 180 °/180 °). *Langmuir* **2007,** *23* (18), 9125-9127.
2. Li, Y.; Zhang, J.; Zhu, S.; Dong, H.; Jia, F.; Wang, Z.; Sun, Z.; Zhang, L.; Li, Y.; Li, H.; Xu, W.; Yang, B., Biomimetic Surfaces for High-Performance Optics. *Adv Mater* **2009,** *21* (46), 4731-4734.
3. Yuan, J. K.; Liu, X. G.; Akbulut, O.; Hu, J. Q.; Suib, S. L.; Kong, J.; Stellacci, F., Superwetting nanowire membranes for selective absorption. *Nature Nanotechnology* **2008,** *3* (6), 332-336.
4. Parker, A. R.; Lawrence, C. R., Water capture by a desert beetle. *Nature* **2001,** *414* (6859), 33-34.
5. Dorvee, J. R.; Derfus, A. M.; Bhatia, S. N.; Sailor, M. J., Manipulation of liquid droplets using amphiphilic, magnetic one-dimensional photonic crystal chaperones. *Nature Materials* **2004,** *3* (12), 896-899.
6. Lee, H.; Lee, B. P.; Messersmith, P. B., A reversible wet/dry adhesive inspired by mussels and geckos. *Nature* **2007,** *448* (7151), 338-U4.
7. Suh, K.-Y.; Park, M. C.; Kim, P., Capillary Force Lithography: A Versatile Tool for Structured Biomaterials Interface Towards Cell and Tissue Engineering. *Adv Funct Mater* **2009,** *19* (17), 2699-2712.
8. Barthlott, W.; Neinhuis, C., Purity of the sacred lotus, or escape from contamination in biological surfaces. *Planta* **1997,** *202* (1), 1-8.
9. Patankar, N. A., Mimicking the Lotus Effect: Influence of Double Roughness Structures and Slender Pillars. *Langmuir* **2004,** *20* (19), 8209-8213.
10. Gao, L. C.; McCarthy, T. J., The "lotus effect" explained: Two reasons why two length scales of topography are important. *Langmuir* **2006,** *22* (7), 2966-2967.
11. Gao, X.; Jiang, L., Biophysics: Water-repellent legs of water striders. *Nature* **2004,** *432* (7013), 36-36.
12. Cong, Q.; Chen, G. H.; Fang, Y.; Ren, L. Q., Study on the super-hydrophobic characteristic of butterfly wing surface. *J. Bionics Eng.* **2004,** *1*, 249.
13. Shibuichi, S.; Onda, T.; Satoh, N.; Tsujii, K., Super water-repellent surfaces resulting from fractal structure. *Journal of Physical Chemistry* **1996,** *100* (50), 19512-19517.
14. Xue, C. H.; Jia, S. T.; Zhang, J.; Tian, L. Q., Superhydrophobic surfaces on cotton textiles by complex coating of silica nanoparticles and hydrophobization. *Thin Solid Films* **2009,** *517* (16), 4593-4598.
15. Li, J.; Fu, J.; Cong, Y.; Wu, Y.; Xue, L.; Han, Y., Macroporous fluoropolymeric films templated by silica colloidal assembly: A possible route to super-hydrophobic surfaces. *Appl Surf Sci* **2006,** *252* (6), 2229-2234.
16. Stelmashuk, V.; Biederman, H.; Slavínská, D.; Zemek, J.; Trchová, M., Plasma polymer films rf sputtered from PTFE under various argon pressures. *Vacuum* **2005,** *77* (2), 131-137.
17. Kim, S. H.; Kim, J.-H.; Kang, B.-K.; Uhm, H. S., Superhydrophobic CFx Coating via In-Line Atmospheric RF Plasma of He−CF4−H2. *Langmuir* **2005,** *21* (26), 12213-12217.
18. Carpentier, J.; Grundmeier, G., Chemical structure and morphology of thin bilayer and composite organosilicon and fluorocarbon microwave plasma polymer films. *Surface and Coatings Technology* **2005,** *192* (2-3), 189-198.

19. Fresnais, J.; Benyahia, L.; Poncin-Epaillard, F., Dynamic (de)wetting properties of superhydrophobic plasma-treated polyethylene surfaces. *Surf Interface Anal* **2006,** *38* (3), 144-149.
20. Kiuru, M.; Alakoski, E., Low sliding angles in hydrophobic and oleophobic coatings prepared with plasma discharge method. *Mater Lett* **2004,** *58* (16), 2213-2216.
21. Teshima, K.; Sugimura, H.; Inoue, Y.; Takai, O.; Takano, A., Transparent ultra water-repellent poly(ethylene terephthalate) substrates fabricated by oxygen plasma treatment and subsequent hydrophobic coating. *Appl Surf Sci* **2005,** *244* (1-4), 619-622.
22. Teshima, K.; Sugimura, H.; Inoue, Y.; Takai, O.; Takano, A., Wettablity of Poly(ethylene terephthalate) Substrates Modified by a Two-Step Plasma Process: Ultra Water Repellent Surface Fabrication. *Chem Vapor Depos* **2004,** *10* (6), 295-297.
23. Wu, Y.; Bekke, M.; Inoue, Y.; Sugimura, H.; Kitaguchi, H.; Liu, C.; Takai, O., Mechanical durability of ultra-water-repellent thin film by microwave plasma-enhanced CVD. *Thin Solid Films* **2004,** *457* (1), 122-127.
24. Han, J. T.; Zheng, Y.; Cho, J. H.; Xu, X.; Cho, K., Stable Superhydrophobic Organic−Inorganic Hybrid Films by Electrostatic Self-Assembly. *The Journal of Physical Chemistry B* **2005,** *109* (44), 20773-20778.
25. Schondelmaier, D.; Cramm, S.; Klingeler, R.; Morenzin, J.; Zilkens, C.; Eberhardt, W., Orientation and Self-Assembly of Hydrophobic Fluoroalkylsilanes. *Langmuir* **2002,** *18* (16), 6242-6245.
26. Song, X.; Zhai, J.; Wang, Y.; Jiang, L., Fabrication of Superhydrophobic Surfaces by Self-Assembly and Their Water-Adhesion Properties. *The Journal of Physical Chemistry B* **2005,** *109* (9), 4048-4052.
27. Zhang, G.; Wang, D.; Gu, Z.-Z.; Möhwald, H., Fabrication of Superhydrophobic Surfaces from Binary Colloidal Assembly. *Langmuir* **2005,** *21* (20), 9143-9148.
28. Zhao, N.; Shi, F.; Wang, Z.; Zhang, X., Combining Layer-by-Layer Assembly with Electrodeposition of Silver Aggregates for Fabricating Superhydrophobic Surfaces. *Langmuir* **2005,** *21* (10), 4713-4716.
29. Shi, F.; Wang, Z.; Zhang, X., Combining a Layer-by-Layer Assembling Technique with Electrochemical Deposition of Gold Aggregates to Mimic the Legs of Water Striders. *Adv Mater* **2005,** *17* (8), 1005-1009.
30. Ma, M.; Mao, Y.; Gupta, M.; Gleason, K. K.; Rutledge, G. C., Superhydrophobic Fabrics Produced by Electrospinning and Chemical Vapor Deposition. *Macromolecules* **2005,** *38* (23), 9742-9748.
31. Liu, H.; Feng, L.; Zhai, J.; Jiang, L.; Zhu, D. B., Reversible wettability of a chemical vapor deposition prepared ZnO film between superhydrophobicity and superhydrophilicity. *Langmuir* **2004,** *20* (14), 5659-5661.
32. Hosono, E.; Fujihara, S.; Honma, I.; Zhou, H. S., Superhydrophobic perpendicular nanopin film by the bottom-up process. *J Am Chem Soc* **2005,** *127* (39), 13458-13459.
33. Han, J. T.; Lee, D. H.; Ryu, C. Y.; Cho, K., Fabrication of Superhydrophobic Surface from a Supramolecular Organosilane with Quadruple Hydrogen Bonding. *J Am Chem Soc* **2004,** *126* (15), 4796-4797.
34. Hikita, M.; Tanaka, K.; Nakamura, T.; Kajiyama, T.; Takahara, A., Super-Liquid-Repellent Surfaces Prepared by Colloidal Silica Nanoparticles Covered with Fluoroalkyl Groups. *Langmuir* **2005,** *21* (16), 7299-7302.

35. Li, Y.; Cai, W.; Cao, B.; Duan, G.; Sun, F., Fabrication of the periodic nanopillar arrays by heat-induced deformation of 2D polymer colloidal monolayer. *Polymer* **2005,** *46* (26), 12033-12036.

36. Nakajima, A.; Saiki, C.; Hashimoto, K.; Watanabe, T., Processing of roughened silica film by coagulated colloidal silica for super-hydrophobic coating. *J Mater Sci Lett* **2001,** *20* (21), 1975-1977.

37. Jiang, L.; Zhao, Y.; Zhai, J., A Lotus-Leaf-like Superhydrophobic Surface: A Porous Microsphere/Nanofiber Composite Film Prepared by Electrohydrodynamics. *Angewandte Chemie International Edition* **2004,** *43* (33), 4338-4341.

38. Singh, A.; Steely, L.; Allcock, H. R., Poly[bis(2,2,2-trifluoroethoxy)phosphazene] Superhydrophobic Nanofibers. *Langmuir* **2005,** *21* (25), 11604-11607.

39. Acatay, K.; Simsek, E.; Ow-Yang, C.; Menceloglu, Y. Z., Tunable, Superhydrophobically Stable Polymeric Surfaces by Electrospinning. *Angewandte Chemie International Edition* **2004,** *43* (39), 5210-5213.

40. Suh, K. Y.; Jon, S., Control over Wettability of Polyethylene Glycol Surfaces Using Capillary Lithography. *Langmuir* **2005,** *21* (15), 6836-6841.

41. He, B.; Patankar, N. A.; Lee, J., Multiple Equilibrium Droplet Shapes and Design Criterion for Rough Hydrophobic Surfaces. *Langmuir* **2003,** *19* (12), 4999-5003.

42. Öner, D.; McCarthy, T. J., Ultrahydrophobic Surfaces. Effects of Topography Length Scales on Wettability. *Langmuir* **2000,** *16* (20), 7777-7782.

43. Fürstner, R.; Barthlott, W.; Neinhuis, C.; Walzel, P., Wetting and Self-Cleaning Properties of Artificial Superhydrophobic Surfaces. *Langmuir* **2005,** *21* (3), 956-961.

44. Patankar, N. A., Transition between Superhydrophobic States on Rough Surfaces. *Langmuir* **2004,** *20* (17), 7097-7102.

45. Patankar, N. A., On the Modeling of Hydrophobic Contact Angles on Rough Surfaces. *Langmuir* **2003,** *19* (4), 1249-1253.

46. Martines, E.; Seunarine, K.; Morgan, H.; Gadegaard, N.; Wilkinson, C. D. W.; Riehle, M. O., Superhydrophobicity and Superhydrophilicity of Regular Nanopatterns. *Nano Letters* **2005,** *5* (10), 2097-2103.

47. Yoshimitsu, Z.; Nakajima, A.; Watanabe, T.; Hashimoto, K., Effects of Surface Structure on the Hydrophobicity and Sliding Behavior of Water Droplets. *Langmuir* **2002,** *18* (15), 5818-5822.

48. Jin, M. H.; Feng, X. J.; Feng, L.; Sun, T. L.; Zhai, J.; Li, T. J.; Jiang, L., Superhydrophobic aligned polystyrene nanotube films with high adhesive force. *Adv. Mater.* **2005,** *17* (16), 1977-+.

49. Nakajima, A.; Abe, K.; Hashimoto, K.; Watanabe, T., Preparation of hard super-hydrophobic films with visible light transmission. *Thin Solid Films* **2000,** *376* (1-2), 140-143.

50. Nakajima, A.; Fujishima, A.; Hashimoto, K.; Watanabe, T., Preparation of Transparent Superhydrophobic Boehmite and Silica Films by Sublimation of Aluminum Acetylacetonate. *Adv Mater* **1999,** *11* (16), 1365-1368.

51. Minko, S.; Müller, M.; Motornov, M.; Nitschke, M.; Grundke, K.; Stamm, M., Two-Level Structured Self-Adaptive Surfaces with Reversibly Tunable Properties. *J Am Chem Soc* **2003,** *125* (13), 3896-3900.

52. Khorasani, M. T.; Mirzadeh, H., In vitro blood compatibility of modified PDMS surfaces as superhydrophobic and superhydrophilic materials. *J Appl Polym Sci* **2004,** *91* (3), 2042-2047.

53. Khorasani, M. T.; Mirzadeh, H.; Kermani, Z., Wettability of porous polydimethylsiloxane

surface: morphology study. *Appl Surf Sci* **2005,** *242* (3-4), 339-345.

54. Li, M.; Zhai, J.; Liu, H.; Song, Y.; Jiang, L.; Zhu, D., Electrochemical Deposition of Conductive Superhydrophobic Zinc Oxide Thin Films. *The Journal of Physical Chemistry B* **2003,** *107* (37), 9954-9957.

55. Daoud, W. A.; Xin, J. H.; Tao, X., Superhydrophobic Silica Nanocomposite Coating by a Low-Temperature Process. *J Am Ceram Soc* **2004,** *87* (9), 1782-1784.

56. Jung, D.-H.; Park, I. J.; Choi, Y. K.; Lee, S.-B.; Park, H. S.; Rühe, J., Perfluorinated Polymer Monolayers on Porous Silica for Materials with Super Liquid Repellent Properties. *Langmuir* **2002,** *18* (16), 6133-6139.

57. Li, X. H.; Cao, Z.; Liu, F.; Zhang, Z. J.; Dang, H. X., A novel method of preparation of superhydrophobic nanosilica in aqueous solution. *Chem Lett* **2006,** *35* (1), 94-95.

58. Mahltig, B.; Böttcher, H., Modified Silica Sol Coatings for Water-Repellent Textiles. *J Sol-gel Sci Techn* **2003,** *27* (1), 43-52.

59. Nakagawa, T.; Soga, M., A new method for fabricating water repellent silica films having high heat-resistance using the sol-gel method. *J Non-cryst Solids* **1999,** *260* (3), 167-174.

60. Venkateswara Rao, A.; Kulkarni, M. M.; Amalnerkar, D. P.; Seth, T., Superhydrophobic silica aerogels based on methyltrimethoxysilane precursor. *J Non-cryst Solids* **2003,** *330* (1-3), 187-195.

61. Rao, A. V.; Pajonk, G. M.; Bhagat, S. D.; Barboux, P., Comparative studies on the surface chemical modification of silica aerogels based on various organosilane compounds of the type RnSiX4-n. *J Non-cryst Solids* **2004,** *350*, 216-223.

62. Roig, A.; Molins, E.; Rodriguez, E.; Martinez, S.; Moreno-Manas, M.; Vallribera, A., Superhydrophobic silica aerogels by fluorination at the gel stage. *Chem Commun* **2004,** (20), 2316-2317.

63. Shirtcliffe, N. J.; McHale, G.; Newton, M. I.; Perry, C. C., Intrinsically Superhydrophobic Organosilica Sol−Gel Foams. *Langmuir* **2003,** *19* (14), 5626-5631.

64. Ming, W.; Wu, D.; van Benthem, R.; de With, G., Superhydrophobic Films from Raspberry-like Particles. *Nano Letters* **2005,** *5* (11), 2298-2301.

65. Sun, T.; Wang, G.; Liu, H.; Feng, L.; Jiang, L.; Zhu, D., Control over the Wettability of an Aligned Carbon Nanotube Film. *J Am Chem Soc* **2003,** *125* (49), 14996-14997.

66. Mulder, M., Basic Principles of Membrane Technology, Kluwer Academic, Dordrecht. **1991**.

67. Zhao, N.; Xie, Q.; Weng, L.; Wang, S.; Zhang, X.; Xu, J., Superhydrophobic Surface from Vapor-Induced Phase Separation of Copolymer Micellar Solution. *Macromolecules* **2005,** *38* (22), 8996-8999.

68. Xie, Q.; Fan, G.; Zhao, N.; Guo, X.; Xu, J.; Dong, J.; Zhang, L.; Zhang, Y., Facile Creation of a Bionic Super-Hydrophobic Block Copolymer Surface. *Adv Mater* **2004,** *16* (20), 1830-1833.

69. Huang, Z.-M.; Zhang, Y. Z.; Kotaki, M.; Ramakrishna, S., A review on polymer nanofibers by electrospinning and their applications in nanocomposites. *Compos Sci Technol* **2003,** *63* (15), 2223-2253.

70. Wenzel, R. N., RESISTANCE OF SOLID SURFACES TO WETTING BY WATER. *Industrial & Engineering Chemistry* **1936,** *28* (8), 988-994.

71. Cassie, A. B. D.; Baxter, S., Wettability of porous surfaces. *Transactions of the Faraday Society* **1944,** *40*, 0546-0550.

72. Pease, D. C., The Significance of the Contact Angle in Relation to the Solid Surface. *The Journal of Physical Chemistry* **1945,** *49* (2), 107-110.

73. Gao, L.; McCarthy, T. J., How Wenzel and Cassie Were Wrong. *Langmuir* **2007,** *23* (7), 3762-3765.
74. Gao, L.; McCarthy, T. J., Wetting 101°†. *Langmuir* **2009,** *25* (24), 14105-14115.
75. Gao, L.; McCarthy, T. J., An Attempt to Correct the Faulty Intuition Perpetuated by the Wenzel and Cassie "Laws". *Langmuir* **2009,** *25* (13), 7249-7255.
76. Young, T., An Essay on the Cohesion of Fluids. *Phil. Trans. R. Soc. Lond.* **1805,** *95*, 23.
77. Quere, D., Non-sticking drops. *Rep Prog Phys* **2005,** *68* (11), 2495-2532.
78. Herminghaus, S., Roughness-induced non-wetting. *EPL (Europhysics Letters)* **2000,** *52* (2), 165.
79. Marmur, A., Wetting on Hydrophobic Rough Surfaces: To Be Heterogeneous or Not To Be? *Langmuir* **2003,** *19* (20), 8343-8348.
80. Furmidge, C. G. L., Studies at phase interfaces. I. The sliding of liquid drops on solid surfaces and a theory for spray retention. *Journal of Colloid Science* **1962,** *17* (4), 309-324.
81. Marmur, A., Soft contact: measurement and interpretation of contact angles. *Soft Matter* **2006,** *2* (1), 12-17.
82. Dorrer, C.; Rühe, J., Advancing and Receding Motion of Droplets on Ultrahydrophobic Post Surfaces. *Langmuir* **2006,** *22* (18), 7652-7657.
83. Chen, W.; Fadeev, A. Y.; Hsieh, M. C.; Oner, D.; Youngblood, J.; McCarthy, T. J., Ultrahydrophobic and Ultralyophobic Surfaces: Some Comments and Examples. *Langmuir* **1999,** *15* (10), 3395-3399.
84. Callies, M.; Quere, D., On water repellency. *Soft Matter* **2005,** *1* (1), 55-61.
85. Bico, J.; Marzolin, C.; Quere, D., Pearl drops (vol 47, pg 220, 1999). *Europhys Lett* **1999,** *47* (6), 743-744.
86. Lafuma, A.; Quere, D., Superhydrophobic states. *Nature Materials* **2003,** *2* (7), 457-460.
87. Wier, K. A.; McCarthy, T. J., Condensation on ultrahydrophobic surfaces and its effect on droplet mobility: Ultrahydrophobic surfaces are not always water repellant. *Langmuir* **2006,** *22* (6), 2433-2436.
88. Dorrer, C.; Rühe, J., Condensation and Wetting Transitions on Microstructured Ultrahydrophobic Surfaces. *Langmuir* **2007,** *23* (7), 3820-3824.
89. Bico, J.; Thiele, U.; Quéré, D., Wetting of textured surfaces. *Colloids and Surfaces A: Physicochemical and Engineering Aspects* **2002,** *206* (1-3), 41-46.
90. Quéré, D.; et al., Slippy and sticky microtextured solids. *Nanotechnology* **2003,** *14* (10), 1109.
91. Ishino, C.; Okumura, K.; Quere, D., Wetting transitions on rough surfaces. *Europhys Lett* **2004,** *68* (3), 419-425.
92. Barbieri, L.; Wagner, E.; Hoffmann, P., Water Wetting Transition Parameters of Perfluorinated Substrates with Periodically Distributed Flat-Top Microscale Obstacles. *Langmuir* **2007,** *23* (4), 1723-1734.
93. Nosonovsky, M.; Bhushan, B., Biomimetic superhydrophobic surfaces: Multiscale approach. *Nano Letters* **2007,** *7* (9), 2633-2637.
94. Bormashenko, E.; Pogreb, R.; Whyman, G.; Erlich, M., Cassie−Wenzel Wetting Transition in Vibrating Drops Deposited on Rough Surfaces: Is the Dynamic Cassie−Wenzel Wetting Transition a 2D or 1D Affair? *Langmuir* **2007,** *23* (12), 6501-6503.
95. Zhao, X.-D.; Fan, H.-M.; Luo, J.; Ding, J.; Liu, X.-Y.; Zou, B.-S.; Feng, Y.-P., Electrically Adjustable, Super Adhesive Force of a Superhydrophobic Aligned MnO2 Nanotube Membrane. *Adv*

Funct Mater **2011,** *21* (1), 184-190.
96. Krupenkin, T.; Taylor, J. A.; Kolodner, P.; Hodes, M., Electrically tunable superhydrophobic nanostructured surfaces. *Bell Labs Tech J* **2005,** *10* (3), 161-170.
97. Moulinet, S.; Bartolo, D., Life and death of a fakir droplet: Impalement transitions on superhydrophobic surfaces. *The European Physical Journal E: Soft Matter and Biological Physics* **2007,** *24* (3), 251-260.
98. Reyssat, M.; et al., Impalement of fakir drops. *EPL (Europhysics Letters)* **2008,** *81* (2), 26006.
99. Bartolo, D.; Bouamrirene, F.; Verneuil, E.; Buguin, A.; Silberzan, P.; Moulinet, S., Bouncing or sticky droplets: Impalement transitions on superhydrophobic micropatterned surfaces. *Europhys Lett* **2006,** *74* (2), 299-305.
100. Zheng, Q. S.; Yu, Y.; Zhao, Z. H., Effects of Hydraulic Pressure on the Stability and Transition of Wetting Modes of Superhydrophobic Surfaces. *Langmuir* **2005,** *21* (26), 12207-12212.
101. Extrand, C. W., Designing for Optimum Liquid Repellency. *Langmuir* **2006,** *22* (4), 1711-1714.
102. Liu, B.; Lange, F. F., Pressure induced transition between superhydrophobic states: Configuration diagrams and effect of surface feature size. *J Colloid Interf Sci* **2006,** *298* (2), 899-909.
103. Schwartz, L. W.; Garoff, S., Contact angle hysteresis on heterogeneous surfaces. *Langmuir* **1985,** *1* (2), 219-230.
104. Chatain, D.; Lewis, D.; Baland, J.-P.; Carter, W. C., Numerical Analysis of the Shapes and Energies of Droplets on Micropatterned Substrates. *Langmuir* **2006,** *22* (9), 4237-4243.
105. Ishino, C.; Okumura, K., Nucleation scenarios for wetting transition on textured surfaces: The effect of contact angle hysteresis. *EPL (Europhysics Letters)* **2006,** *76* (3), 464.
106. Sbragaglia, M.; Peters, A. M.; Pirat, C.; Borkent, B. M.; Lammertink, R. G. H.; Wessling, M.; Lohse, D., Spontaneous Breakdown of Superhydrophobicity. *Phys Rev Lett* **2007,** *99* (15), 156001.
107. Zhang, J.; Kwok, D. Y., Contact Line and Contact Angle Dynamics in Superhydrophobic Channels. *Langmuir* **2006,** *22* (11), 4998-5004.
108. Feng, Z.-P.; Li, G.-R.; Zhong, J.-H.; Wang, Z.-L.; Ou, Y.-N.; Tong, Y.-X., MnO2 multilayer nanosheet clusters evolved from monolayer nanosheets and their predominant electrochemical properties. *Electrochem Commun* **2009,** *11* (3), 706-710.
109. Li, B.; Rong, G.; Xie, Y.; Huang, L.; Feng, C., Low-Temperature Synthesis of α-MnO2 Hollow Urchins and Their Application in Rechargeable Li+ Batteries. *Inorg Chem* **2006,** *45* (16), 6404-6410.
110. Wang, H.-e.; Qian, D.; Lu, Z.; Li, Y.; Cheng, R.; Li, Y., Facile synthesis and electrochemical properties of hierarchical MnO2 submicrospheres and LiMn2O4 microspheres. *J Phys Chem Solids* **2007,** *68* (7), 1422-1427.
111. Wang, X.; Li, Y., Selected-Control Hydrothermal Synthesis of α- and β-MnO2 Single Crystal Nanowires. *J Am Chem Soc* **2002,** *124* (12), 2880-2881.
112. Wu, X.; Zheng, L.; Wu, D., Fabrication of Superhydrophobic Surfaces from Microstructured ZnO-Based Surfaces via a Wet-Chemical Route. *Langmuir* **2005,** *21* (7), 2665-2667.
113. Vayssieres, L.; Keis, K.; Hagfeldt, A.; Lindquist, S.-E., Three-Dimensional Array of Highly Oriented Crystalline ZnO Microtubes. *Chem Mater* **2001,** *13* (12), 4395-4398.
114. Jia, C.-J.; Sun, L.-D.; Yan, Z.-G.; You, L.-P.; Luo, F.; Han, X.-D.; Pang, Y.-C.; Zhang, Z.; Yan, C.-H., Single-Crystalline Iron Oxide Nanotubes. *Angewandte Chemie International Edition* **2005,**

44 (28), 4328-4333.
115. Price, D. J.; Batten, S. R.; Moubaraki, B.; Murray, K. S., Synthesis, structure and magnetism of a new manganese carboxylate cluster: [Mn16O16(OMe)6(OAc)16(MeOH)3(H2O)3][middle dot]6H2O. *Chem Commun* **2002,** (7), 762-763.
116. Han, J. T.; Kim, S.; Karim, A., UVO-tunable superhydrophobic to superhydrophilic wetting transition on biomimetic nanostructured surfaces. *Langmuir* **2007,** *23* (5), 2608-2614.
117. Liu, M.; Zheng, Y.; Zhai, J.; Jiang, L., Bioinspired Super-antiwetting Interfaces with Special Liquid−Solid Adhesion. *Accounts Chem Res* **2009,** *43* (3), 368-377.
118. NEINHUIS, C.; BARTHLOTT, W., Characterization and Distribution of Water-repellent, Self-cleaning Plant Surfaces. *Ann Bot* **1997,** *79* (6), 667-677.
119. Jung, Y. C.; Bhushan, B., Dynamic Effects Induced Transition of Droplets on Biomimetic Superhydrophobic Surfaces. *Langmuir* **2009,** *25* (16), 9208-9218.
120. Dorrer, C.; Ruhe, J., Some thoughts on superhydrophobic wetting. *Soft Matter* **2009,** *5* (1), 51-61.
121. Ahuja, A.; Taylor, J. A.; Lifton, V.; Sidorenko, A. A.; Salamon, T. R.; Lobaton, E. J.; Kolodner, P.; Krupenkin, T. N., Nanonails: A Simple Geometrical Approach to Electrically Tunable Superlyophobic Surfaces. *Langmuir* **2007,** *24* (1), 9-14.
122. Cao, L.; Hu, H.-H.; Gao, D., Design and Fabrication of Micro-textures for Inducing a Superhydrophobic Behavior on Hydrophilic Materials. *Langmuir* **2007,** *23* (8), 4310-4314.
123. Tuteja, A.; Choi, W.; Ma, M.; Mabry, J. M.; Mazzella, S. A.; Rutledge, G. C.; McKinley, G. H.; Cohen, R. E., Designing Superoleophobic Surfaces. *Science* **2007,** *318* (5856), 1618-1622.
124. Tuteja, A.; Choi, W.; Mabry, J. M.; McKinley, G. H.; Cohen, R. E., Robust omniphobic surfaces. *Proceedings of the National Academy of Sciences of the United States of America* **2008,** *105* (47), 18200-18205.
125. Luo, J.; Zhu, H. T.; Fan, H. M.; Liang, J. K.; Shi, H. L.; Rao, G. H.; Li, J. B.; Du, Z. M.; Shen, Z. X., Synthesis of single-crystal tetragonal alpha-MnO2 nanotubes. *Journal of Physical Chemistry C* **2008,** *112* (33), 12594-12598.
126. Zhu, H. T.; Luo, J.; Yang, H. X.; Liang, J. K.; Rao, G. H.; Li, J. B.; Du, Z. M., Birnessite-type MnO2 Nanowalls and Their Magnetic Properties. *The Journal of Physical Chemistry C* **2008,** *112* (44), 17089-17094.
127. Chhatre, S. S.; Choi, W.; Tuteja, A.; Park, K.-C.; Mabry, J. M.; McKinley, G. H.; Cohen, R. E., Scale Dependence of Omniphobic Mesh Surfaces. *Langmuir* **2009,** *26* (6), 4027-4035.
128. Parkin, I. P.; Palgrave, R. G., Self-cleaning coatings. *J Mater Chem* **2005,** *15* (17), 1689-1695.
129. Xia, F.; Jiang, L., Bio-inspired, smart, multiscale interfacial materials. *Adv Mater* **2008,** *20* (15), 2842-2858.
130. Blossey, R., Self-cleaning surfaces [mdash] virtual realities. *Nat Mater* **2003,** *2* (5), 301-306.
131. Ma, M. L.; Hill, R. M., Superhydrophobic surfaces. *Curr Opin Colloid In* **2006,** *11* (4), 193-202.
132. Guo, Z.-G.; Liu, W.-M., Sticky superhydrophobic surface. *Appl Phys Lett* **2007,** *90* (22), 223111.
133. Bormashenko, E.; Stein, T.; Pogreb, R.; Aurbach, D., "Petal Effect" on Surfaces Based on Lycopodium: High-Stick Surfaces Demonstrating High Apparent Contact Angles. *Journal of Physical Chemistry C* **2009,** *113* (14), 5568-5572.
134. Feng, L.; Zhang, Y. A.; Xi, J. M.; Zhu, Y.; Wang, N.; Xia, F.; Jiang, L., Petal effect: A

superhydrophobic state with high adhesive force. *Langmuir* **2008,** *24* (8), 4114-4119.
135. Liao, C. S.; Wang, C. F.; Lin, H. C.; Chou, H. Y.; Chang, F. C., Fabrication of Patterned Superhydrophobic Polybenzoxazine Hybrid Surfaces. *Langmuir* **2009,** *25* (6), 3359-3362.
136. Winkleman, A.; Gotesman, G.; Yoffe, A.; Naaman, R., Immobilizing a drop of water: Fabricating highly hydrophobic surfaces that pin water droplets. *Nano Letters* **2008,** *8* (4), 1241-1245.
137. Li, W.; Amirfazli, A., Superhydrophobic Surfaces: Adhesive Strongly to Water? *Adv Mater* **2007,** *19* (21), 3421-3422.
138. Jin, M. H.; Feng, X. J.; Feng, L.; Sun, T. L.; Zhai, J.; Li, T. J.; Jiang, L., Superhydrophobic aligned polystyrene nanotube films with high adhesive force. *Adv Mater* **2005,** *17* (16), 1977-1981.
139. Zhao, N.; Xie, Q. D.; Kuang, X.; Wang, S. Q.; Li, Y. F.; Lu, X. Y.; Tan, S. X.; Shen, J.; Zhang, X. L.; Zhang, Y.; Xu, J.; Han, C. C., A novel ultra-hydrophobic surface: Statically non-wetting but dynamically non-sliding. *Adv Funct Mater* **2007,** *17* (15), 2739-2745.
140. Yuekun Lai, X. G., Huifang Zhuang, Jianying Huang, Changjian Lin, Lei Jiang, Designing Superhydrophobic Porous Nanostructures with Tunable Water Adhesion. *Adv Mater* **2009,** *21*, 1-5.
141. Lai, Y.; Lin, C.; Huang, J.; Zhuang, H.; Sun, L.; Nguyen, T., Markedly Controllable Adhesion of Superhydrophobic Spongelike Nanostructure TiO2 Films. *Langmuir* **2008,** *24* (8), 3867-3873.
142. Dai, H., Carbon Nanotubes: Synthesis, Integration, and Properties. *Accounts Chem Res* **2002,** *35* (12), 1035-1044.
143. Bhushan, B.; Koch, K.; Jung, Y. C., Nanostructures for superhydrophobicity and low adhesion. *Soft Matter* **2008,** *4* (9), 1799-1804.
144. Borras, A.; González-Elipe, A. n. R., Wetting Properties of Polycrystalline TiO2 Surfaces: A Scaling Approach to the Roughness Factors. *Langmuir* **2010,** *26* (20), 15875-15882.
145. Richard, D.; Quéré, D., Viscous drops rolling on a tilted non-wettable solid. *EPL (Europhysics Letters)* **1999,** *48* (3), 286.
146. McHale, G., Cassie and Wenzel: Were They Really So Wrong? *Langmuir* **2007,** *23* (15), 8200-8205.
147. Bormashenko, E., A Variational Approach to Wetting of Composite Surfaces: Is Wetting of Composite Surfaces a One-Dimensional or Two-Dimensional Phenomenon? *Langmuir* **2009,** *25* (18), 10451-10454.
148. Bormashenko, E., Why does the Cassie-Baxter equation apply? *Colloid Surface A* **2008,** *324* (1-3), 47-50.
149. Chung, J. Y.; Youngblood, J. P.; Stafford, C. M., Anisotropic wetting on tunable micro-wrinkled surfaces. *Soft Matter* **2007,** *3* (9), 1163-1169.
150. Li, Y.; Zhang, J.; Zhu, S.; Dong, H.; Jia, F.; Wang, Z.; Sun, Z.; Zhang, L.; Li, Y.; Li, H.; Xu, W.; Yang, B., Biomimetic Surfaces for High-Performance Optics. *Adv Mater* **2009,** *9999* (9999), NA.
151. Erbil, H. Y.; inodot; ld; Demirel, A. L.; Avc; , Y.; Mert, O., Transformation of a Simple Plastic into a Superhydrophobic Surface. *Science* **2003,** *299* (5611), 1377-1380.
152. Woodward, J. T.; Gwin, H.; Schwartz, D. K., Contact Angles on Surfaces with Mesoscopic Chemical Heterogeneity. *Langmuir* **2000,** *16* (6), 2957-2961.
153. Lim, H. S.; Kwak, D.; Lee, D. Y.; Lee, S. G.; Cho, K., UV-Driven reversible switching of a roselike vanadium oxide film between superhydrophobicity and superhydrophilicity. *J Am Chem Soc* **2007,** *129* (14), 4128-+.
154. Lahann, J.; Mitragotri, S.; Tran, T. N.; Kaido, H.; Sundaram, J.; Choi, I. S.; Hoffer, S.; Somorjai,

G. A.; Langer, R., A reversibly switching surface. *Science* **2003,** *299* (5605), 371-374.
155. Verplanck, N.; Galopin, E.; Camart, J.-C.; Thomy, V.; Coffinier, Y.; Boukherroub, R., Reversible Electrowetting on Superhydrophobic Silicon Nanowires. *Nano Letters* **2007,** *7* (3), 813-817.
156. Sun, T.; Wang, G.; Feng, L.; Liu, B.; Ma, Y.; Jiang, L.; Zhu, D., Reversible Switching between Superhydrophilicity and Superhydrophobicity13. *Angewandte Chemie International Edition* **2004,** *43* (3), 357-360.
157. Jiang, Y.; Wang, Z.; Yu, X.; Shi, F.; Xu, H.; Zhang, X.; Smet, M.; Dehaen, W., Self-Assembled Monolayers of Dendron Thiols for Electrodeposition of Gold Nanostructures: Toward Fabrication of Superhydrophobic/Superhydrophilic Surfaces and pH-Responsive Surfaces. *Langmuir* **2005,** *21* (5), 1986-1990.
158. Bodre, C.; Pauporte, T., Nanostructured ZnO-Based Surface with Reversible Electrochemically Adjustable Wettability. *Adv Mater* **2009,** *21* (6), 697-+.
159. Kakade, B.; Mehta, R.; Durge, A.; Kulkarni, S.; Pillai, V., Electric field induced, superhydrophobic to superhydrophilic switching in multiwalled carbon nanotube papers. *Nano Letters* **2008,** *8* (9), 2693-2696.
160. Chen, J. Y.; Kutana, A.; Collier, C. P.; Giapis, K. P., Electrowetting in Carbon Nanotubes. *Science* **2005,** *310* (5753), 1480-1483.
161. Zhu, L. B.; Xu, J. W.; Xiu, Y. H.; Sun, Y. Y.; Hess, D. W.; Wong, C. P., Electrowetting of aligned carbon nanotube films. *J Phys Chem B* **2006,** *110* (32), 15945-15950.
162. Wang, Z. K.; Ci, L. J.; Chen, L.; Nayak, S.; Ajayan, P. M.; Koratkar, N., Polarity-dependent electrochemically controlled transport of water through carbon nanotube membranes. *Nano Letters* **2007,** *7* (3), 697-702.
163. Wang, S.; Jiang, L., Definition of superhydrophobic states. *Adv Mater* **2007,** *19* (21), 3423-3424.
164. Jing, Z. H.; Wu, S. H., Preparation and magnetic properties of spherical alpha-Fe2O3 nanoparticles via a non-aqueous medium. *Mater Chem Phys* **2005,** *92* (2-3), 600-603.
165. Lambert, P., *Capillary forces in microassembly: modeling, simulation, experiments, and case study*
2007; p 45-49.
166. Han, Z. J.; Tay, B.; Tan, C. M.; Shakerzadeh, M.; Ostrikov, K., Electrowetting Control of Cassie-to-Wenzel Transitions in Superhydrophobic Carbon Nanotube-Based Nanocomposites. *Acs Nano* **2009,** *3* (10), 3031-3036.
167. Mugele, F.; Baret, J. C., Electrowetting: From basics to applications. *J Phys-condens Mat* **2005,** *17* (28), R705-R774.
168. Krupenkin, T. N.; Taylor, J. A.; Schneider, T. M.; Yang, S., From Rolling Ball to Complete Wetting: The Dynamic Tuning of Liquids on Nanostructured Surfaces. *Langmuir* **2004,** *20* (10), 3824-3827.
169. Poetes, R.; Holtzmann, K.; Franze, K.; Steiner, U., Metastable Underwater Superhydrophobicity. *Phys Rev Lett* **2010,** *105* (16), 166104.